STUDYING CLOUDS AND AEROSOLS WITH LIDAR DEPOLARIZATION RATIO AND BACKSCATTER RELATIONSHIPS

A Dissertation

by

HYOUN MYOUNG CHO

Submitted to the Office of Graduate Studies of
Texas A&M University
in partial fulfillment of the requirements for the degree of

DOCTOR OF PHILOSOPHY

December 2011

Major Subject: Atmospheric Sciences

Studying Clouds and Aerosols with Lidar Depolarization Ratio and Backscatter Relationships

A STUDYING CLOUDS AND AEROSOLS WITH LIDAR DEPOLARIZATION RATIO AND BACKSCATTER RELATIONSHIPS

A Dissertation

by

HYOUN MYOUNG CHO

Submitted to the Office of Graduate Studies of
Texas A&M University
in partial fulfillment of the requirements for the degree of

DOCTOR OF PHILOSOPHY

Approved by:

Co-Chairs of Committee,	Ping Yang
	Shaima L. Nasiri
Committee Members,	Gerald R. North
	George W. Kattawar
Head of Department,	Kenneth Bowman

December 2011

Major Subject: Atmospheric Sciences

ABSTRACT

Studying Clouds and Aerosols with Lidar Depolarization Ratio and Backscatter Relationships. (December 2011)

Hyoun Myoung Cho, B.S., Seoul National University, South Korea;
M.S, Seoul National University, South Korea

Co-Chairs of Advisory Committee: Dr. Ping Yang
Dr. Shaima L. Nasiri

This dissertation consists of three parts, each devoted to a particular issue of significant importance for CALIPSO lidar observation of depolarization ratio (δ) and backscatter (γ') to improve current understanding of the microphysical properties of clouds and aerosols. The relationships between depolarization ratio and backscatter allow us to retrieve particle thermodynamic phase and shape and/or orientation of aerosols and clouds.

The first part is devoted to the investigation of the relationships between lidar backscatter and the corresponding depolarization ratio for different cloud classifications and aerosol types. For each cloud and aerosol types, layer-averaged backscatter and backscattering depolarization ratio from the CALIPSO measurements are discussed. The present results demonstrate the unique capabilities of the CALIPSO lidar instrument for determining cloud phase and aerosols subtypes.

In the second part, we evaluate the MODIS IR cloud phase with the CALIPSO cloud products. The three possible misclassifications of MODIS IR cloud phase algorithm, which are studied by Nasiri and Kahn (2008) with radiative transfer modeling, are tested by comparing between MODIS IR phase and CALIOP observations. The current results support their hypotheses, which is that the MODIS phase algorithm may tend to classify thin cirrus clouds as water clouds or mixed phase clouds or unknown, and classify midlevel and/or mid-temperature clouds as mixed or unknown phase.

In the third part, we present a comparison of mineral dust aerosol retrievals from two instruments, MODIS and CALIPSO lidar. And, we implement and evaluate a new mineral dust detection algorithm based on the analysis of thin dust radiative signature. In comparison, three commonly used visible and IR mineral dust detection algorithms, including BTD procedure, D parameter method, and multi-channel image algorithm, are evaluated with CALIPSO aerosol classification. The comparison reveals that those dust detection algorithms are not effective for optically thin dust layers, but for thick dust storm. The new algorithm using discriminant analysis with CALIPSO observation is much better in detecting thin dust layer of optical thickness between 0.1 and 2.

ACKNOWLEDGEMENTS

I would like to express my sincere gratitude to my advisor, Dr. Ping Yang, for his wise guidance and continuous support during my Ph.D. study. I would like to thank another committee chair, Dr. Shaima Nasiri, for her guidance and endurance. She showed remarkable endurance throughout my Ph. D. work, inspiring and encouraging to achieve at the highest levels of science.

The research presented in this dissertation was partially supported by the United States National Science Foundation (ATM-0803779), U.S. National Oceanic and Atmospheric Administration (DG133E09CN0258), NASA (NNL006AA01A) and the endowment funds associated with the David Bullock Harris Chair in Geosciences, College of Geosciences, Texas A&M University.

I would also like to thank my committee members, Drs. Gerald North, and George Kattawar, for their interests in my research and constructive comments. Thanks also go to group members, colleagues and the department faculty and staff for making my time at Texas A&M University a great experience. I would also like to thank my friends, Jasf members, especially Sung-Uk Jung. I believe he is resting in heaven.

Lastly, I would like to thank my wife Keun-Hee Lee, the love of my life, for the loving support and patience she has given me all these years. I would also like to thank my family, my father, Il-Rae Cho and my mother, You-Yun Park, for all the unconditional help throughout the years. And please rest in peace, my grandmother, Bong-Jae Lee.

TABLE OF CONTENTS

Page

ABSTRACT iii

ACKNOWLEDGEMENTS v

TABLE OF CONTENTS vi

LIST OF FIGURES viii

LIST OF TABLES xii

1. INTRODUCTION 1

    1.1 Clouds and Aerosols and Their Role in Climate 1
    1.2 Passive Remote Sensing of Cloud Phases and Mineral Dust Aerosols 2
    1.3 Issues, Challenges and New Opportunities 5

2. DEPOLARIZATION RATIO AND BACKSCATTER RELATIONSHIPS... 10

    2.1 Polarization Lidar 10
    2.2 CALIPSO Lidar 13
    2.3 CALIPSO Lidar δ–γ' Relations for MODIS-based Cloud Classes 17
    2.4 CALIPSO Lidar δ–γ' Relations for Different Aerosol Types 47
    2.5 Summary 49

3. AN EVALUATION OF THE COLLECTION 5 MODIS IR CLOUDS PHASE RETRIEVAL 50

    3.1 Introduction 50
    3.2 MODIS IR Phase 51
    3.3 CALIPSO Cloud Layer Product 53
    3.4 Comparisons between MODIS and CALIPSO Cloud Phase Products 54
    3.5 Summary and Conclusions 69

4. DETECTION OF OPTICALLY THIN MINERAL DUST AEROSOL LAYERS USING MODIS 72

    4.1 Introduction 72
    4.2 Data 73

Page

4.3 Initial Evaluation of Existing Dust Detection Methods 76
4.4 MODIS Radiative Signatures of the Thin Dust Layers........................ 82
4.5 A New Multi-spectral MODIS Algorithm using Discriminant Analysis 95
4.6 Application of the New Dust Detection Algorithm 97
4.7 Summary and Conclusions.. 105

5. SUMMARY 107

REFERENCES.. 110

APPENDIX.. 126

VITA 129

LIST OF FIGURES

FIGURE Page

2.1 Principle of backscattering depolarization from a spherical water droplet, a hexagonal plate, and a solid column (From Liou, 2002). 12

2.2 The CALIPSO satellite image in 'A-train' (Courtesy of NASA CALIPSO web page: http://www-calipso.larc.nasa.gov/resources/images/a-train%28arch%29.jpg) 15

2.3 Schematic curves showing the relationships (Hu et al. 2007) between the layer-integrated depolarization ratio and layer-integrated attenuated backscatter coefficient for ice clouds (solid line) and water clouds (dashed line) 16

2.4 The ISCCP cloud classification scheme.. 19

2.5 The CALIPSO lidar δ–γ' relationships for nine ISCCP cloud types, as classified using MODIS data. Observations are over 12 months, from July 2006 to June 2007. The color of each pixel represents the frequency of occurrence for a $\Delta\delta$–$\Delta\gamma'$ box with 0.01 by 0.002 sr^{-1} interval 21

2.6 Histogram and normalized frequency of the difference between the MODIS and CALIPSO cloud top pressure retrievals during daytime in the August of 2006 25

2.7 Same as Fig. 2.5 except for single-layer clouds identified from the CALIPSO data.. 27

2.8 The δ–γ' relations for nine cloud types in the tropical region from 30°S to 30°N 28

2.9 The δ–γ' relation for nine cloud types in the midlatitudes (30°S-60°S and 30°N-60°N) 29

2.10 The δ–γ' relationships for clouds in the polar regions (60°S-90°S and 60°N-90°N) 31

FIGURE Page

2.11 The δ–γ' relationships with respect to cloud top temperature obtained by MODIS cloud retrievals for single-layer clouds identified from the CALIPSO data........ 33

2.12 The δ–γ' relationships for the clouds classified as water-phase by the MODIS IR cloud-phase determination algorithm........ 34

2.13 The δ–γ' relationship for the clouds classified as ice-phase by the MODIS IR cloud-phase determination algorithm........ 36

2.14 The δ–γ' relationship for clouds classified as mixed- or uncertain-phase by the MODIS IR cloud-phase determination algorithm........ 37

2.15 The δ–γ' relationship for clouds classified as water-phase by the MODIS cloud property retrieval processing path (RPP) phase determination algorithm........ 39

2.16 The δ–γ' relationship for clouds classified as ice-phase by the MODIS RPP phase determination algorithm........ 40

2.17 The δ–γ' relationship for clouds classified as undetermined-phase by the MODIS RPP phase determination algorithm........ 41

2.18 Same as Fig. 2.12 except for single-layer clouds identified from the CALIPSO data........ 43

2.19 Same as Fig. 2.13 except for single-layer clouds identified from the CALIPSO data........ 44

2.20 Same as Fig. 2.14 except for single-layer clouds identified from the CALIPSO data........ 45

2.21 The CALIPSO lidar δ–γ' relationships for six aerosol sub-types observed in 2008. The color of each pixel represents the frequency of occurrence for a $\Delta\delta$–$\Delta\gamma'$ box with 0.01 by 0.002 sr^{-1} interval........ 48

3.1 Difference in height between adjacent layers in the CALIPSO 5-km cloud layer product from January to June 2008. The left figure shows the distribution layer separations while the right figure shows the normalized cumulative distribution........ 55

FIGURE Page

3.2 The cloud top height and mid-layer temperature distribution of MODIS IR cloud phase for three layers (i.e. (a) and (b) are for single layers, (c) and (d) are for opaque single layers, and (e) and (f) are for transparent single layers) as detected by CALIPSO from January to June 2008 58

3.3 Zonal frequencies of cloud phase are shown for CALIPSO cloud phase in (a), MODIS IR cloud phase for all single layer clouds detected by CALIPSO in (b), all single-layer clouds classified as water by CALIPSO in (c), and (d) all single-layer clouds classified as ice by CALIPSO......... 64

3.4 Distributions of MODIS IR phase for opaque single-layer clouds detected by CALIPSO are shown with respect to CALIPSO-retrieved mid-layer cloud temperature for clouds classified by CALIPSO as water (a), ice (b), mixed-uncertain phases (c), and unknown (d) 65

3.5 Same as Fig. 3.4, but for transparent single-layer clouds 66

4.1 (a) MODIS RGB image on April 2, 2008 (1450 UTC) along with the CALIPSO track (the center line with colors), (b) MODIS aerosol optical thickness (AOT), and dust detection results (c, d, and e) for the $BTD_{11\text{-}12\mu m}$ threshold tests, (f) for the D parameter methods, and (g) for the MCI algorithm. Pixels classified as dust by each technique are shown in orange 79

4.2 Distribution of MODIS NDVI (a~c) and 3 by 3 pixel standard deviation of MODIS $R_{0.55\mu m}$ (d~f) for each of the CALIPSO clear, cloud, and dust categories (left panel: clear, middle panel: cloud, and right panel: dust pixels) during 2008... 84

4.3 (a) MODIS RGB image from January 1, 2008 (0055 UTC) along with CALIPSO flight track and (b) the RGB image of the red box area indicated in (a). The colorbar shows the CALIPSO scene classification along the CALIPSO track. Note that the CALIPSO retrieval classifies the region in the red circle in (b) as clear, although the MODIS image implies the presence of cloud.. 86

4.4 Distribution of 3 by 3 pixel standard deviation of MODIS $R_{0.55\mu m}$ for the modified CALIPSO categories (first row: clear ($R_{0.64\mu m}<0.05$), second row: clear ($R_{0.64\mu m}\geq0.05$), third row: cloud, and bottom row: dust) during 2008 with respect to different latitude bands (left column), and CALIPSO optical thickness (right column) 87

FIGURE Page

4.5 Same as Fig. 4.4 except for normalized difference vegetation index (NDVI) (see Eqn. 4.2) 89

4.6 Same as Fig. 4.4 except for the ratio of MODIS $R_{0.47\mu m}$ and $R_{0.64\mu m}$ 90

4.7 Same as Fig. 4.4 except for normalized difference dust index (NDDI)..... 92

4.8 Same as Fig. 4.4 except for $BTD_{8.5\text{-}11\mu m}$........ 93

4.9 Same as Fig. 4.4 except for $BTD_{11\text{-}12\mu m}$ 94

4.10 (a) MODIS RGB image on April 2, 2008 (1450 UTC) with the CALIPSO track, (b) aerosol optical thickness, and (c) dust detection results for the LDA, and (d) for the QDA methods. Black, white, and orange colors in (a), (c), and (d) represent clear, cloud, and dust pixels, respectively. Blue in (a) refers to the CALIPSO ‘other’ classification. Green in (c and d) represents undetermined pixels, typically due to sunglint. Blue in (c and d) marks land surfaces 98

4.11 Same as Fig. 4.10 except for on April 15, 2008 (0430 UTC) 99

4.12 CALIPSO cloud optical thickness histograms for LDA classifications [Clear (a and b), Cloud (c and d), and Dust (e and f)] for the CALIPSO cloud category. Left panels show lower confidence classifications, while right panels indicate higher confidence ones 103

4.13 Same as Fig. 4.12 except for the CALIPSO dust category 104

LIST OF TABLES

TABLE Page

2.1 Statistics of the differences between the MODIS and CALIPSO cloud-top pressure retrievals 24

3.1 CALIPSO top layers with layers separated by less than 200 m combined into a single layer. Columns are MODIS phase classifications while rows are CALIPSO phase classifications. There are three positions in the interior cells. The top position represents the number of pixels falling into both MODIS and CALIPSO categories, the middle position (in parentheses) is the percentage of pixels in the MODIS class out of all pixels in the CALIPSO class, while the bottom position is the percentage out of the total number of pixels 61

3.2 Same as Table 3.1 except for CALIPSO single layers 62

3.3 Same as Table 3.1 except for CALIPSO opaque single layers 67

3.4 Same as Table 3.1 except for CALIPSO transparent single layers 68

4.1 Comparisons between MODIS dust detection techniques and co-located CALIPSO scene classification during 2008 daytime over ocean. Rows are MODIS dust detection techniques, including three different BTD thresholds, while columns are CALIPSO cloud/dust classifications. The percentages in the interior cells represent the percentage of dust pixels by MODIS dust detection techniques out of the total number of the each CALIPSO classes. Note that CALIPSO dust categories are separated into thin and thick layer by a CALIPSO optical thickness (τ) threshold of 1 80

4.2 The statistics of the new MODIS LDA algorithm over ocean during 2009. Note that each LDA classification is broken into two degrees of confidence according to the conditional probability ($P<0.8$ implies lower confidence than $P\geq 0.8$). Values in bold indicate agreement between the MODIS LDA and CALIPSO categories 100

4.3 Same as Table 2, but for the QDA method 101

1. INTRODUCTION

1.1 Clouds and Aerosols and Their Role in Climate

Aerosols and clouds play an important role in the planetary radiation energy budget. Aerosols and clouds interact with both solar and infrared radiation. Clouds reduce the incoming solar energy by reflecting sunlight back to space, which result in cooling the earth surface. At the same time, clouds reduce the outgoing thermal radiation by absorbing the energy emitted by the earth's surface, leading to a warming of the atmosphere. The net effect of these cooling and warming effects depends on several factors, including the cloud fraction, lifetime, the altitude, temperature and transparency of the cloud layers, their thermodynamic phases and their multilayer structures (Wielicki et al. 1995). Aerosols also scatter sunlight back to space and absorb the radiation directly as clouds (Ångström 1962; McCormick and Ludwig 1967). In addition to the direct effect, aerosols can affect the earth's climate indirectly through the modification of cloud albedo (Twomey 1974), and the modification of the vertical thickness and horizontal extent of clouds, possibly leading to the so-called cloud-lifetime effect (Albrecht 1989; Pincus and Baker 1994). Because aerosol particles can act as cloud condensation nuclei (CCN), increase in aerosol concentration can increase the number of droplets, so that the average size of the droplets decreases. Therefore, the aerosols prevent the cloud from raining out and extend its lifetime, because smaller droplets do not fall to the ground.

However, the estimation of these cloud and aerosol effects on climate is not

---

This dissertation follows the style of *Journal of Atmospheric Sciences*.

straightforward. To estimate these effects, the concept of radiative forcing is widely used. The radiative forcing of cloud and aerosol is effective parameter in studying the interaction between the radiation and cloud/aerosol and in diagnosing model simulations. The uncertainty in cloud and aerosol forcing comes from the compatibility between observation and theoretical computation. For instance, the cloud radiative forcing in theory is supposed to represent the radiative effects of cloud alone, but in reality it is influenced by factors other than clouds such as clear sky background conditions including aerosols and water vapor. And the accurate determination of aerosol radiative effect is also difficult because of complexities in optical and chemical properties of the aerosols, and in the transport and cloud modification process. Thus, it is clear that accurate measurements of cloud and aerosol are important to quantify radiative forcings.

1.2 Passive Remote Sensing of Cloud Phases and Mineral Dust Aerosols

Satellite measurements can be used to infer cloud and aerosol properties, including feature top height/pressure/temperature, optical thickness, and effective particle size globally. However, significant errors in estimating the cloud and aerosol radiative forcing can be introduced by uncertainties in the satellite cloud and aerosol products. Thus, it is important to evaluate the quality of cloud and aerosol products inferred from satellite observations. Passive remote sensing of clouds and aerosols currently focuses on multi-spectral approaches. These approaches are based on the assumption that scattering or absorption by atmospheric particles can occur dominantly in some wavelengths. To retrieve a given cloud or aerosol property, algorithms employ the bands that effectively utilize the information content. For example, combination of two bands centered at visible (VIS) and shortwave-infrared (SWIR) wavelengths can be used to infer cloud optical thickness and effective particle size (Nakajima and King 1990). To retrieve cloud top pressure (CTP) for mid to high clouds, bands located within the 15μm CO_2 absorption region can be used (the CO_2 slicing technique), while low-level cloud top temperature (CTT) can be retrieved by using the IR window band (Menzel et al. 2006, 2008; Platnick et al. 2003). Since these cloud and aerosol products are inferred from different spectral bands, and sometime different instruments, it is necessary to examine the consistency between the retrieved products.

The cloud thermodynamic phase is critical to infer the accurate optical and microphysical properties of clouds, and to determine radiative forcing because the radiative properties of clouds vary with their phases. In passive remote sensing, the spectral absorption difference between visible (VIS) and shortwave infrared (SWIR) wavelengths is widely used to determine the cloud thermodynamic phase (Pilewskie and Twomey 1987; Riédi et al. 2000; Knap et al. 2002; Platnick et al. 2003; Pavolonis et al. 2005; Chylek et al. 2006). The brightness temperature differences between three IR window channels centered at 8.5, 11, and 12 μm are also often used for discriminating cloud thermodynamic phase (Baum et al. 2000).

In the climate study of atmospheric aerosols, mineral dust aerosols, composed of soil particles lifted into the atmosphere by wind, are important because they contribute significantly to the global aerosol loading (Duce et al. 1991). In terms of mass, mineral dust aerosol is the largest one of all aerosol types, comparable only to sea salt (Zender et al. 2004). Thus, the climatic effects of mineral dust are potentially large. Mineral dust also affects air quality and cloud formation. Recent studies (Dunion and Velden 2004; Evan et al. 2006a) showed the dust storm could affect the formation and evolution of hurricane.

Due to the importance of mineral dust aerosols in climate and environment, the use of remote sensing is required for providing more information about mineral dust aerosols on the both regional and global scale. Various algorithms have been developed to separate dust aerosols from clear and cloud pixels in a wide range of wavelengths from ultra-violet (UV) to infrared (IR) with various sensors. For example, the index of UV-absorbing aerosols (Aerosol Index; AI), provided by Ozone Monitoring Instrument (OMI) onboard Aura satellite, can be used to detect dust and smoke (Herman et al. 1997; Torres et al. 1998, 2007). Many researchers (Tanré and Legrand 1991; Kaufman et al. 2000; Miller 2003; and Qu et al. 2006) have used visible (VIS) / near IR (NIR) band ratios to detect dust. The brightness temperatures from thermal IR wavelengths can be also used (Shenk and Curran 1974; Ackerman 1989, 1997; Legrand et al. 1989, 2001; Wald et al. 1998; Darmenov and Sokolik 2005; and Hao and Qu 2007). And more complex algorithms using combinations of VIS/NIR and TIR wavelengths are proposed by several researchers (Roskovensky and Liou 2005, Hansell et al. 2007; and Zhao et al. 2010). Martins et al. (2002) pointed out that the spatial variability could be used to discriminate homogeneous dust layers from clouds. They found that clouds tend to have much complex spatial structure than aerosols due to the complicated dynamic and thermodynamic processes in cloud evolution. On the other hands, dust layers apart from its source regions tend to have homogeneous structure except for dense dust storm cases.

1.3 Issues, Challenges and New Opportunities

As mentioned in the previous subsection, satellite-based remote sensing of clouds and aerosols requires good understanding of several different aspects as well as the knowledge of radiative transfer process and retrieval methods. Cloud radiative properties and cloud life cycle are influenced by the cloud thermodynamic phase (Sun and Shine 1994; Harrington et al. 1999; Yoshida and Asano 2005; Ehrlich et al. 2008). Because the cloud phases and aerosol types are difficult to predict in weather prediction and climate models, uncertainty in these parameters may lead to large errors in estimates of precipitation and the strength of the circulation (Chylek et al. 2006). For climate studies, the monitoring of cloud microphysical and optical properties as well as aerosol-cloud interactions is essential.

Because cloud phase directly impacts the hydrometeor types (rain, snow, hail, etc.), the accurate determination of cloud thermodynamic phase is critical in precipitation processes in atmospheric model. The cloud thermodynamic phase is also important for retrieving the optical and microphysical properties of clouds. In addition to cloud phases, the particle shapes in ice clouds are also important to determine cloud radiative forcing because the radiative properties of cloud particles vary widely according to their shapes (Liou 2002; Yang et al. 2005). For cloud radiative property calculation, the cloud particles have been usually categorized into two kinds of shape (i.e. spherical and non-spherical shapes; Fu 1996). Several field experimental researches

(Stephens et al. 1990; Stackhouse and Stephens 1991) show that the asymmetry factor of non-spherical particle is significantly smaller than that of spherical particle. Because of large differences in the radiative properties between spherical and non-spherical ice particles, inaccurate representation of cloud particle shapes can lead to systematic biases in climate model simulation (Senior and Mitchell 1993; Ho et al. 1998).

In passive satellite remote sensing of cloud-phase, the most widely used one is the Moderate Resolution Imaging Spectroradiometer (MODIS) bispectral IR phase product (Platnick et al. 2003). However, Nasiri and Kahn (2008) recently discussed several limitations of the MODIS IR algorithm by the radiative transfer modeling study. They point out the potential misclassification for 1) MODIS to classify optically thin cirrus clouds as water clouds, 2) MODIS to classify optically thin cirrus clouds as mixed or unknown phase, and 3) opaque ice clouds composed of small particles to be classified as water clouds and that it was likely that 4) midlevel (approximately 4–7 km) or mid-temperature water or ice clouds would be classified as mixed phase or unknown. Here the term “mid-temperature” refers to temperatures at which water, ice, or mixed phase particles could coexist—roughly between 250 and 265 K.

In the mineral dust study, the net radiative impact on the climate cycle is still uncertain (Seinfeld et al. 2004; House et al. 2006). In fact, it is still not known whether mineral dust will have a net warming or cooling effect (Houghton et al. 2001). The overall radiative effect of dust depends on not only the single scattering albedo of the dust particle but to the underlying surface. For instance, dust over dark surfaces, such as oceans, can decrease the absorption of solar radiation, leading to a cooling effect (Tegen et al. 1996), however dust over high reflective regions, such as ice, snow or desert surfaces, can have warming effect. Claquin et al. (2003) proposed that the high concentration of dust has cooling effect of the tropics. Other researcher (Overpeck et al. 1996) found that dust accelerates deglaciation. The role of dust particle as condensation nuclei in cloud formation is also uncertain, however it is potentially significant (Rosenfeld et al. 2001; Levin et al. 1996). Therefore, an ability to quantify the amounts of atmospheric dust is essential to assess the magnitude of their regional impacts and radiative forcing.

Studies in aerosol types by passive remote sensing were limited mainly because of the difficulty in classifying chemical components from the columnar measurements of radiances/reflectances from space (Li et al. 2009). In particular, significant problems in detecting mineral dust have been demonstrated in case of the clouds presence (Brennan et al. 2005; Darmenov and Sokolik 2005; Evan et al. 2006b). The remote sensing in detecting mineral dust is affected by several factors, including the radiative, microphysical, and optical properties of the particle, the radiative properties of the land/ocean surface, the presence or absence of cloud, and the sensor characteristics and radiative transfer model used to detect dust (Baddock et al. 2009). Problems to determine dust sources may occur particularly in the presence of cloud and the existence of low contrast between dust and land/ocean surface (Gassó and Stein 2007; Bullard et al. 2008).

As mentioned in the previous subsection, numerous dust detection methods have been developed. These dust detection algorithms were successful with varying degrees depending on the observation conditions (day/night, land/ocean, etc.). In terms of aerosol optical thickness (AOT), the over-ocean retrieval algorithms are more accurate than that over land due to a little effect of the surface (Kaufman et al. 2000). However, in spite of these extensive researches, most of them are focused on optically thick dust storms and often fail to detect optically thin dust layers, because the limited vertical information from passive remote sensing is available, especially over the oceans.

Fortunately, with the launch of Cloud-Aerosol Lidar and Infrared Pathfinder Satellite Observations (CALIPSO) having an active instrument, we are able to obtain better information on the particle shape and vertical profile of clouds and aerosols. The CALIPSO mission was developed for observing the global distribution and properties of aerosols and clouds (Winker et al. 2009). The CALIPSO satellite is flying in formation with the A-train constellation of satellites (Stephens et al. 2002), which are in a 705-km sun-synchronous polar orbit with crossing an equator at local time of about 1330. The Cloud-Aerosol Lidar with Orthogonal Polarization (CALIOP; referred to as “CALIPSO lidar” hereafter), a near-nadir viewing two wavelength polarization-sensitive lidar, is the primary instrument on CALIPSO satellite. Depolarization ratio and backscatter observations from the CALIPSO lidar provide valuable new information that will help to further understanding of the microphysical characteristics of aerosols and cloud particles. For example, polarized lidar returns allows evaluation of the existing cloud and aerosol products including cloud phase and dust detection algorithms as independent datasets.

The main theme of this research is to improve current understanding of the microphysical properties of aerosols and clouds by using newly available global observations of lidar depolarization ratio and backscatter relationships. These relationships allow us to retrieve particle thermodynamic phase and shape and/or orientation of aerosols and clouds. The rest of this dissertation is organized into three major sections, each devoted to a particular issue that has been briefly introduced in the previous subsection.

In section 2, we present the relationships between lidar backscatter and the corresponding depolarization ratio for different cloud classifications and aerosol types. For each cloud and aerosol types, layer-averaged backscatter and backscattering depolarization ratio from the CALIPSO measurements are discussed. In section 3, we evaluate the MODIS IR cloud phase with the CALIPSO cloud products. The three possible misclassifications of MODIS cloud phase mentioned in radiative transfer modeling study by Nasiri and Kahn (2008) are tested. In section 4, we investigate the radiative signature of mineral dust. Three commonly used visible and IR mineral dust detection algorithms are evaluated with the CALIPSO classification of aerosol particle from depolarization ratio and backscatter relationship. And, the MODIS radiative signatures of optically-thin dust layer over ocean are investigated. Based on the investigation of thin dust signature, a new dust detection algorithm using discriminant analysis is introduced and evaluated. The final section summarizes the results from the previous sections.

2. DEPOLARIZATION RATIO AND BACKSCATTER RELATIONSHIPS[*]

The lidar, which stands for Light Detection And Ranging, is important tool in remote sensing of the atmosphere. Through the backscattering lidar technique, lidar can provide the information about the composition and structure of clouds, aerosols, and minor gases. Since the development of backscattering lidar technique, more advanced techniques of lidar have been developed, including differential absorption technique, Doppler technique, and depolarization technique. The differential absorption technique, which utilizes multiple wavelengths, is used for detecting the composition of minor gases (Higdon et al. 1994). The Doppler technique is used for determining the motion of particles and air molecules (McGill et al. 1997). The microphysical properties of atmospheric particles can be obtained by the depolarization technique (Liou and Lahore 1974) from the measurements of polarization lidar. This study focuses on this polarization lidar observation.

2.1 Polarization Lidar

A polarization lidar is one of the most powerful remote sensing tools for understanding aerosols and clouds. Since the first publication about polarization lidar cloud measurements was published by Schotland et al. (1971), several research

---

[*] Reprinted with permission from “Depolarization ratio and attenuated backscatter for nine cloud types: analyses based on collocated CALIPSO lidar and MODIS measurements” by H.-M. Cho, P. Yang, G. W. Kattawar, S. L. Nasiri, Y. Hu, P. Minnis, C. Trepte, and D. Winker, 2008. *Optics Express*, 16(6), 3931−3948, Copyright by the Optical Society

programs, including the First International Satellite Cloud Climatology Project Regional Experiment (FIRE), the Experimental Cloud Lidar Pilot Study (ECLIPS), Atmospheric Radiation Measurement (ARM), the Arctic Facility for Atmospheric Remote Sensing (AFARS) and the Lidar In-space Technology Experiment (LITE), were conducted to demonstrate the use of polarization lidar for atmospheric research.

The laser backscatter depolarization technique (Sassen 1991, 2000) was one of the earliest applications of lidar for cloud and climate study. Polarization lidar measurements provide the information about particle shape and orientation for cloud and aerosol. The basic principle of depolarization can be explained by ray-tracing theory, as shown in Fig. 2.1. Spherical scatters, such as water droplets, backscatter the incident rays through a number of possibilities: the edge rays; a central ray that undergoes external reflection; and two refractions, none of which change the incident polarization state. However, nonspherical particle, such as ice crystals, normally comes out after several internal reflections that transform the incident electric vectors, leading to depolarization. The ratio of parallel and perpendicular components of backscattered light from the linearly polarized source is referred to as the linear backscattering depolarization ratio.

The depolarization principle has been supported by field and laboratory measurements (Schotland et al. 1971; Liou and Lahore 1974; Sassen 1976) for various types of ice crystals and water droplets. For example, Sassen (1991, 1994) presented that the depolarization ratio for water clouds is close to zero and that for ice crystals varies from 0.5 to 0.7, depending on their shape and size. This depolarization technique can be

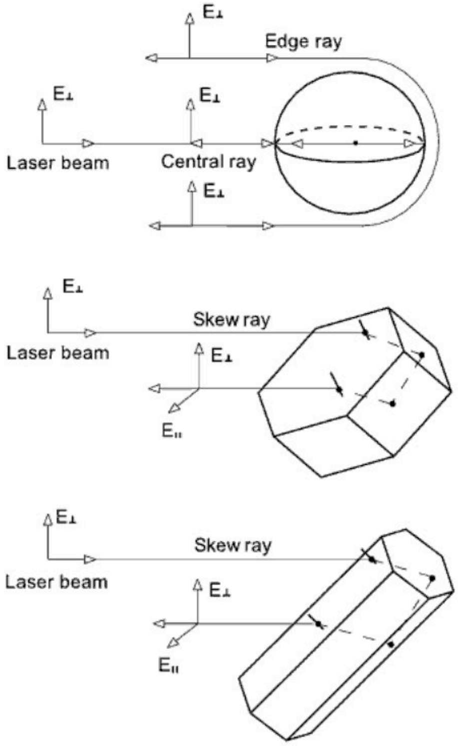

Fig. 2.1 Principle of backscattering depolarization from a spherical water droplet, a hexagonal plate, and a solid column (From Liou, 2002).

used to study the orientation properties of ice particles. In the case of a vertically oriented lidar involving horizontally oriented plates, the depolarization ratio would be zero as a result of the symmetry of the two parallel crystal surfaces with respect to the laser beam.

This technique also can be used to identify the type of atmospheric aerosols because of its particle shape sensitivity (Sassen 2000). Spherical aerosols (e.g., haze and smoke particles) generate little or no change in the incident polarization state, while nonspherical particles (e.g., dust) can produce significant depolarization depending on the particle shape (Mishchenko and Sassen 1998). For example, the mineral dust particle from Asian dust storm shows a highly irregular shape (Okada et al. 2001) and typically have linear depolarization ratios of about 0.2–0.3 (Murayama et al. 2001), which is similar to some ice crystal clouds.

The depolarization technique is valid only when the signal is dominated by single scattering or the lidar field of view (FOV) is narrow, such as ground-based or aircraft-based lidar. When the FOV is wide enough, such as in the case of the CALIPSO lidar which has a 0.13 mrad FOV receiver (90 meter footprint size), even spherical particles generate depolarized signal through multiple scattering events because the incident laser beam is transferred from the initial reference plane to the plane of scattering within the FOV, and therefore, partial depolarization is produced (Hu et al. 2001). Note that this multiple scattering effect is small for ice clouds (Reichardt and Reichardt 2003; You et al. 2006).

2.2 CALIPSO Lidar

This research uses polarization lidar onboard the CALIPSO satellite, which was launched in April, 2006. The main objective of the CALIPSO mission is to provide a global, multi-year data set of cloud and aerosol spatial and optical properties from which to assess uncertainties of aerosol direct and indirect effects on climate forcing and cloud-climate feedback (Winker et al. 2009). To address this objective, CALIPSO satellite carries a two-wavelength and polarization-sensitive elastic backscatter lidar (CALIPSO lidar), which provides high-resolution vertical profiles of aerosols and clouds. The

CALIPSO lidar is a key instrument in the “A-train”, a constellation of five polar-orbiting satellites flying in close formation (Stephens et al. 2002) as shown in Fig. 2.2. The CALIPSO lidar has three receiver channels. One measures the 1064 nm backscatter intensity. Two other channels receive orthogonally polarized components of the 532 nm backscattered signal, respectively.

The CALIPSO cloud and aerosol products used in this study are the CALIPSO level-2 layer data. The CALIPSO data product contains information on up to 10 cloud layers and 8 aerosol layers within each retrieval footprint. Specifically, we use the layer-integrated depolarization ratio (δ) and the total layer-integrated attenuated backscatter (γ') at 532 nm, which are defined as follows:

$$\delta = \frac{\int_{top}^{base} \beta'_{\perp}(z)dz'}{\int_{top}^{base} \beta'_{//}(z)dz'}, \tag{2.1}$$

$$\gamma' = \int_{top}^{base} [\beta'_{\perp}(z) + \beta'_{//}(z)]dz', \tag{2.2}$$

where $\beta'_{\perp}$ and $\beta'_{//}$ are the perpendicular and parallel components of the attenuated backscatter, respectively.

The relationship between depolarization ratio and attenuated backscatter from the lidar measurements can be used to infer microphysical properties of aerosols and cloud layers (Hu et al. 2009). With the depolarization ratio, the measurement of attenuated backscatter gives additional information in the interpretation of the cloud layers. Platt (1978) and Platt et al. (1987) observed that the high backscatter could be used to

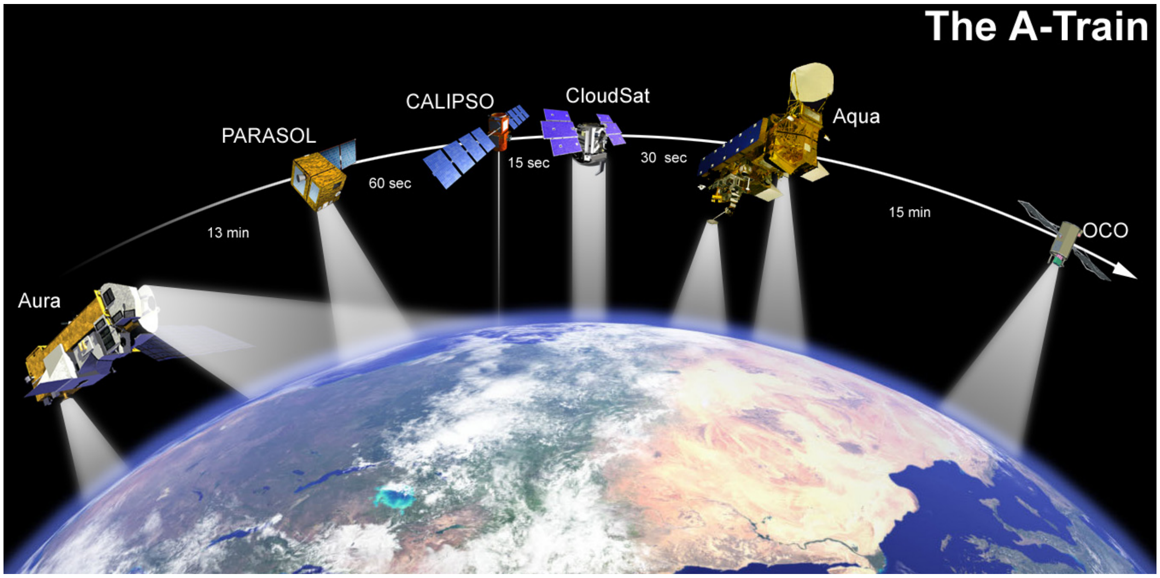

Fig. 2.2 The CALIPSO satellite image in 'A-train' (Courtesy of NASA CALIPSO web page: http://www-calipso.larc.nasa.gov/resources/images/a-train%28arch%29.jpg).

separate the horizontally oriented ice particle from the water cloud layer having a low depolarization ratio.

Hu et al. (2007) derived theoretically the relationships between CALIPSO lidar δ and γ' for both ice and water clouds, which are schematically depicted in Fig. 2.3. Water clouds consisting of spherical liquid droplets have positive correlation between δ and γ', whereas the correlations for ice clouds are negative. It should be pointed out that although the single water droplet does not depolarize the backscattered light, multiple scattering events within a water cloud do tend to depolarize lidar signals. Therefore, the depolarization ratio associated with water clouds increases with increasing backscatter and is positively correlated to the optical depth. The curves for water and ice cross each other near δ=0.171 and γ'=0.0623. The lower right portion of the ice cloud curve

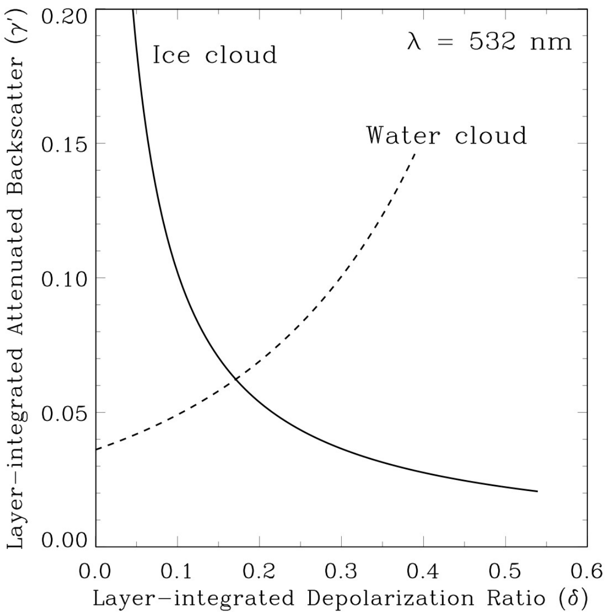

Fig. 2.3 Schematic curves showing the relationships (Hu et al. 2007) between the layer-integrated depolarization ratio and layer-integrated attenuated backscatter coefficient for ice clouds (solid line) and water clouds (dashed line).

(below the intersection with the water curve), corresponding to depolarization ratios between 0.3 and 0.5, is associated with ice clouds consisting of randomly oriented ice particles. The upper left portion of the ice curve, corresponding to high backscatter and small depolarization ratio values, is associated with clouds consisting of horizontally oriented ice crystals such as plates, or horizontally oriented ice columns, such as Parry-oriented columns. From launch to November 2007, the CALIPSO lidar was pointed within 0.3° within nadir. At this orientation, the specular reflection caused by two horizontally-parallel faces of horizontally-oriented ice plates or Parry-oriented columns leads to large backscatter. The specular reflection in this case, however, does not depolarize the backscattered lidar beam because the parallel and perpendicular components of the electric vector associated with the lidar beam are indistinguishable with respect to a horizontal plane. The presence of horizontally-oriented ice crystals has been confirmed using ground-based lidar observations. Additionally, Chepfer et al. (1999), using satellite-based observations by the Polarization and Directionality of Earth Reflectances (POLDER) instrument, found horizontally oriented ice crystals in approximately 40% of ice clouds.

2.3 CALIPSO Lidar δ–γ' Relations for MODIS-based Cloud Classes

2.3.1 Introduction

In this subsection, I review the work published in Cho et al. (2008). This paper reports on the relationship between lidar backscatter and the corresponding depolarization ratio for nine cloud types based on applying the International Satellite Cloud Climatology Project (ISCCP) cloud classification scheme to MODIS observations. Specifically, MODIS MYD06 cloud optical thickness and cloud top pressure are used to classify cloud types. For each cloud type, layer-averaged backscatter and backscattering depolarization ratio from the CALIPSO measurements are investigated. This work also considers the cloud δ-γ' relation with respect to latitude and the cloud phases determined by the MODIS cloud-phase algorithm.

The MODIS retrieved cloud properties used in the present study are Collection-5 MYD06 level-2 cloud products, specifically, optical thickness (τ), cloud top pressure (P_{top}), cloud top temperature (CTT), and two cloud phase products. The retrieval of τ (King et al. 2004) is accomplished using reflectances at 2.1 μm and either 0.65, 0.8, or 1.2 μm, depending on surface type; the retrieved product resolution is 1 km by 1 km. The P_{top} retrievals (Menzel et al. 2008) utilize the CO_2-slicing method for high and midlevel clouds and 11 μm brightness temperature matched to a numerical weather prediction model analysis vertical temperature profile for low clouds; the product resolution is 5 km by 5 km. The first MODIS cloud-phase product in this study is the operational bispectral infrared (IR) cloud phase algorithm. It uses the brightness temperatures at two IR channels and classifies clouds as water-, ice-, or mixed- or uncertain-phase at 5 km resolution. The second cloud phase product uses a multitude of channels and is used in the first step in the retrieval of cloud τ and effective radius. This product is at 1 km resolution and is denoted here as the retrieval processing path (RPP) phase (Platnick et al., 2003). Because the τ and RPP phase retrievals rely on reflected solar radiation, all of our comparisons use only daytime MODIS and CALIPSO observations.

In terms of cloud top pressure and optical thickness, clouds are classified on the basis of the ISCCP scheme (Rossow and Schiffer 1999) as shown in Fig. 2.4. Specifically, a cloud is first categorized as high (50 hPa < P_{top} < 440 hPa), middle (440 hPa < P_{top} < 680 hPa), or low (680 hPa < P_{top} < 1000 hPa). Each cloud-top pressure category is further categorized into one of three sub-types based on cloud optical thickness (τ). For example, high clouds consist of cirrus clouds ($0 < \tau < 3.6$), cirrostratus clouds ($3.6 < \tau < 23$), and deep convective clouds ($23 < \tau < 379$). Similarly, middle clouds are categorized as altocumulus, altostratus, and nimbostratus with respect to the three optical thickness ranges, whereas low clouds are categorized as cumulus, stratocumulus, and stratus. It should be stressed that these cloud classifications are based only on retrieved cloud top height and optical thickness, and therefore vary from other meteorological uses of the class categories.

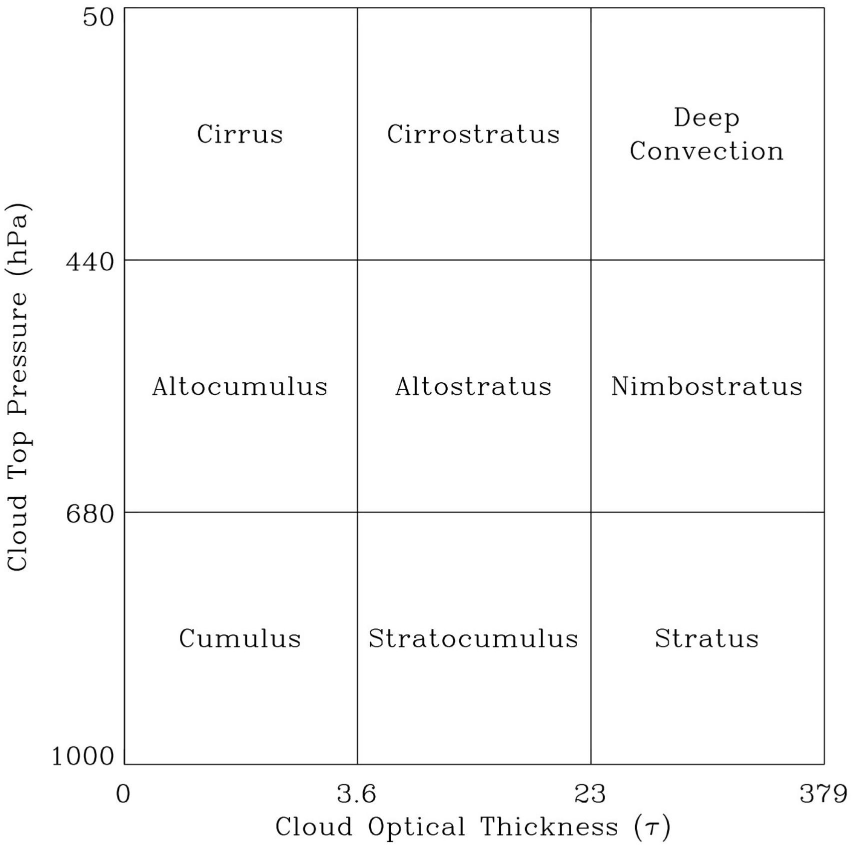

Fig. 2.4 The ISCCP cloud classification scheme.

2.3.2 δ–γ' relation for different cloud types

In this subsection, the data come from 12 months (July 2006 - June 2007) of collocated MODIS Level-2 MYD06 cloud products and CALIPSO Level-2 1-km cloud layer products. The collocation is based on matching the CALIPSO pixels to the nearest MODIS pixels for both 1 km and 5 km MODIS resolutions. For those MODIS variables with a resolution of 5 km by 5 km, approximately 5 CALIPSO pixels correspond to the same MODIS properties. In each figure, the δ–γ' relation is plotted for each cloud class with color representing the number of occurrences for a $\Delta\delta$–$\Delta\gamma'$ box with 0.01 (for $\Delta\delta$) by 0.002 sr^{-1} (for $\Delta\gamma'$) interval.

The δ–γ' relation for the uppermost layers over the entire one year dataset is shown in Fig. 2.5. In total, 4353 daytime CALIPSO granules are used in this study. At daytime, there are 14 to 15 CALIPSO granules per day. A daytime CALIPSO granule consists of approximately 21,000 pixels. The clusters of high observation occurrence match well to the theoretical water and ice cloud curves shown in Fig. 2.3. Note that the δ–γ' patterns for high clouds (cirrus, cirrostratus, and deep convection), altostratus, and nimbostratus are similar to those shown by Hu et al. (2007) for the case where the CALIPSO lidar was pointed at 0.3° of nadir. All CALIPSO lidar data used in this study are pointed at 0.3° of nadir.

For the δ–γ' relationship for high clouds, the feature associated with randomly oriented ice crystals (i.e. low backscatter portion of each panel) dominates, particularly in the cirrus class. However, the feature associated with horizontally oriented crystals (i.e. upper left portion) is prominent for the mid to high optical thickness cases of

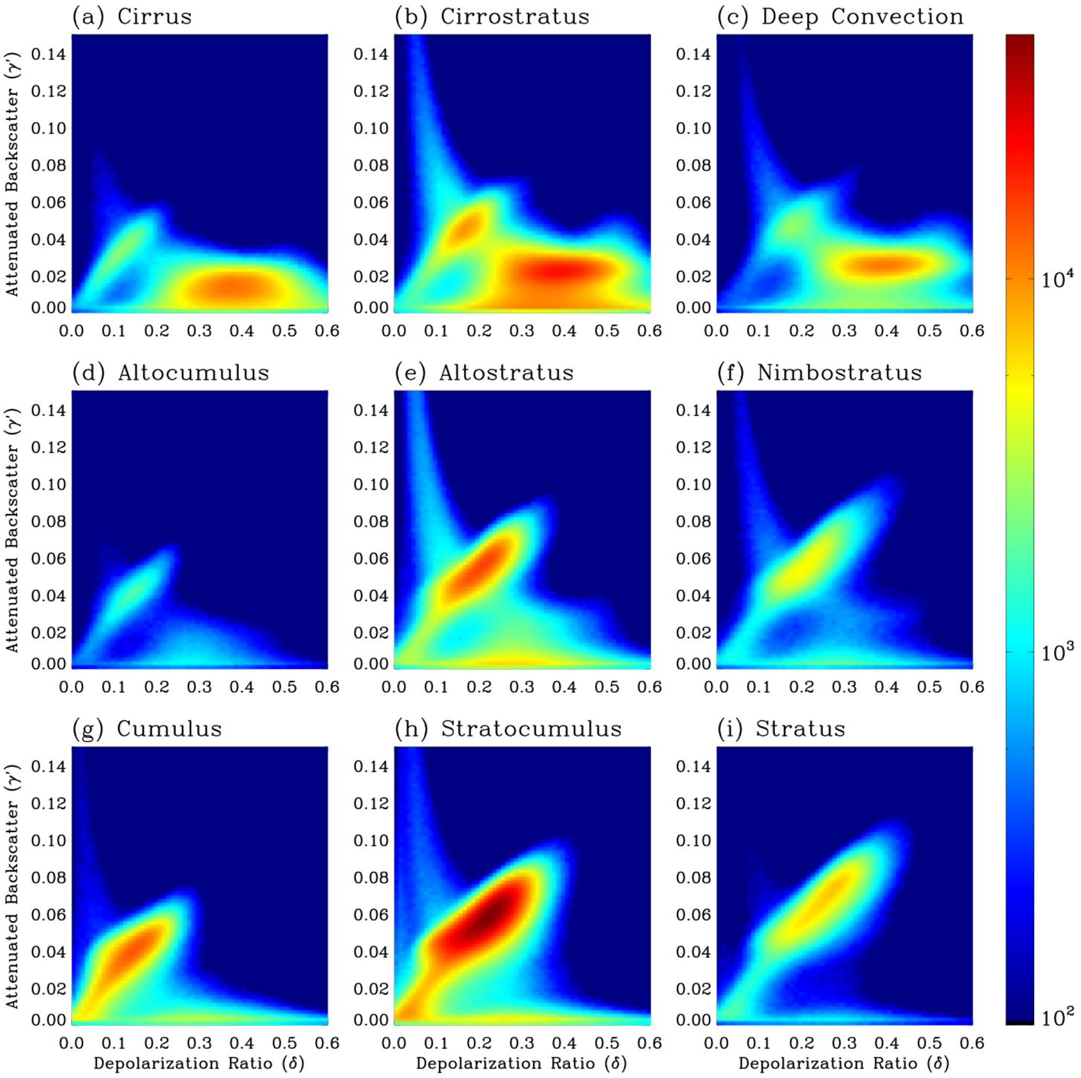

Fig. 2.5 The CALIPSO lidar δ–γ' relationships for nine ISCCP cloud types, as classified using MODIS data. Observations are over 12 months, from July 2006 to June 2007. The color of each pixel represents the frequency of occurrence for a $\Delta\delta$–$\Delta\gamma'$ box with 0.01 by 0.002 sr^{-1} interval.

cirrostratus, deep convection, altostratus, nimbostratus and stratocumulus. The layer-integrated attenuated backscatter values for thick clouds are larger than those for thin clouds because γ' is proportional to cloud thickness. However, the differences between the results for cirrostratus clouds and deep convection are smaller than the counterparts for cirrus and cirrostratus clouds. This feature is primarily due to the attenuation of backscatter within clouds. However, the depolarization ratio in the case of ice clouds consisting of randomly oriented ice crystals is not sensitive to optical depth. The variation of the depolarization ratio is primarily due to different ice crystal habits.

Figure 2.5 also shows clusters with the positive slope feature associated with water clouds in Fig. 2.3. This feature is dominant in the low cloud classes, implying, as expected, that these low clouds tend to be water-phase. However, signatures associated with both ice and water clouds are found in the midlevel (altostratus, in particular) and high cloud classes. These results are not surprising for the midlevel cloud classes, as *in situ* observations show that midlevel clouds can be composed of super-cooled liquid water droplets, ice crystals, or a mixture of both ice and water. The water cloud signatures in the high cloud classes may be due to supercooled-water as the temperatures at 440 hPa in standard tropical and midlatitude summer atmospheres are between 258 and 256 K (McClatchey et al. 1972). For the highest cloud classes, though, we also have to consider the possibility of cloud height misclassification by MODIS, or horizontal inhomogeneities at smaller scales than the MODIS 5x5 km product resolution. If high ice clouds and low level water clouds both exist, not necessarily overlapping geometrically, within a 5 km x 5 km MODIS footprint, they may be assigned a high cloud height by MODIS, while CALIPSO may see individual water clouds and ice clouds.

Many pixels corresponding to small backscatter values in Fig. 2.5 are likely caused by thin cirrus clouds or the uppermost thin clouds in the case of multi-layered clouds. MODIS cloud-height retrievals have difficulty in cases of optically thin clouds and multi-layered clouds. According to Weisz et al. (2007), there are relatively large differences between MODIS and CALIPSO cloud-top height retrievals, particularly for thin cirrus clouds. In the MODIS cloud top retrievals, very thin cirrus clouds (low γ' values) that are not detected by MODIS may be incorrectly classified as a cloud type associated with a lower layer. To avoid the potential ambiguity caused by mismatching cloud top retrievals and overlapping clouds in the cloud phase features shown in the CALIPSO δ–γ' relation, we screened both the MODIS and CALIPSO data to eliminate cases in which the CALIPSO lidar detected multi-layered clouds.

Cloud top heights of the uppermost CALIPSO layers were converted to pressures using the National Centers for Environmental Prediction (NCEP) re-analysis profiles interpolated to CALIPSO grids. Table 2.1 lists the mean pressure difference (MPD) and the standard deviation (SD) of the differences between the cloud top pressures obtained from MODIS and CALIPSO during the daytime in August 2006. The quantities MPD and SD are defined as:

$$\text{MPD} = \frac{1}{N}\sum_{i=0}^{N}\left(P_{i,MODIS} - P_{i,CALIPSO}\right), \tag{2.3}$$

and

$$\mathrm{SD} = \sqrt{\frac{1}{N-1}\sum_{i=0}^{N}\left(\left(P_{i,MODIS} - P_{i,CALIPSO}\right) - \mathrm{MPD}\right)^2}\,, \tag{2.4}$$

respectively. In Eqs. (2.3) and (2.4), *N* indicates the total number of the pixels. It is evident from Table 2.1 that the screened data sets show a smaller MPD and SD values in comparison with the unscreened case.

Table 2.1 Statistics of the differences between the MODIS and CALIPSO cloud-top pressure retrievals.

	Number of Pixels	MPD (hPa)	SD (hPa)
Uppermost layers	5429675	67.2	170.2
Single-layers	3772072	29.5	155.4

Figure 2.6 shows the histograms of the difference between the MODIS and CALIPSO cloud height retrievals in terms of cloud-top pressure difference. The left panel shows the histogram in terms of number of pixels versus the cloud-top pressure difference. Because the unscreened case has more pixels than the screened case (see Table 2.1), the histogram curve of the unscreened case is higher than of the screened case. The right panel shows the normalized frequency of the distribution of the difference between the MODIS and CALIPSO cloud height retrievals. Here the normalized frequency is defined as the ratio of the number of pixels in each histogram

bin shown in the left panel of Fig. 2.6 to the number of total pixels involved in the statistics. The right panel of Fig. 2.6 shows that the peak of the curve is located at $P_{MODIS} - P_{CALIPSO} \approx 10\text{hPa}$ in the screened case whereas the peak of the normalized frequency in the unscreened case is shifted to $P_{MODIS} - P_{CALIPSO} \approx 30\text{hPa}$. While, the normalized frequencies in the screened and unscreened cases look quite similar, it is clear that the MODIS results agree better with the CALIPSO retrievals in the case of single-layered clouds than in the unscreened case where multi-layered clouds exist.

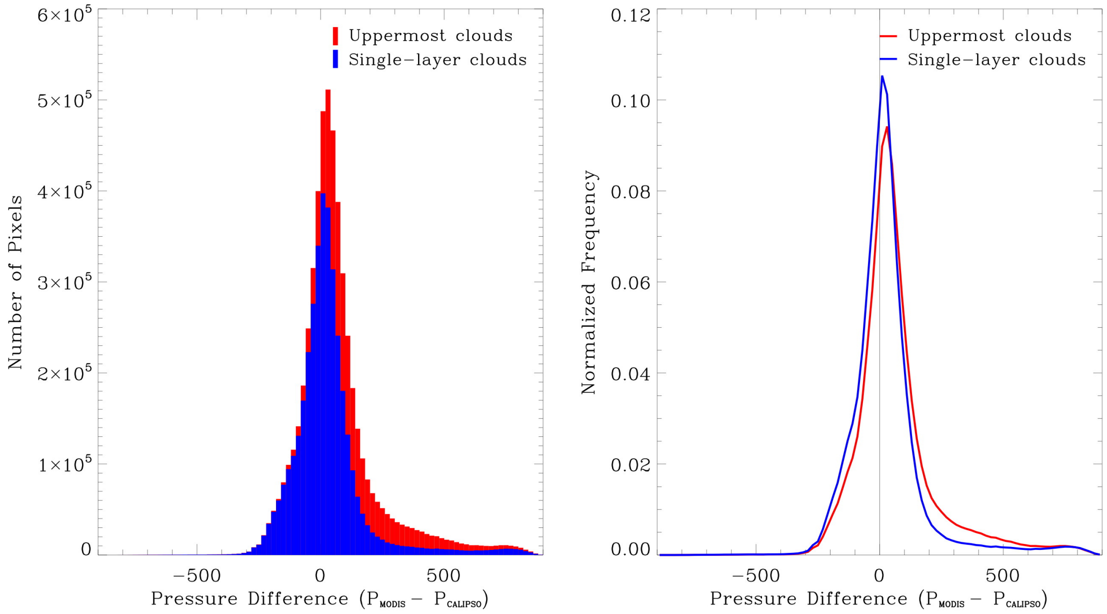

Fig. 2.6 Histogram and normalized frequency of the difference between the MODIS and CALIPSO cloud top pressure retrievals during daytime in the August of 2006.

As the screened counterpart of Fig. 2.5, Fig. 2.7 shows the δ–γ' relations for global single-layered clouds. Overall, the features shown in the δ–γ' relations in the screened (Fig. 2.7) and unscreened (Fig. 2.5) cases are similar. However, the major difference between the results shown in Figs. 2.5 and 2.7 is that small values of attenuated backscatter are eliminated for both water and ice features in the screened case, particularly for moderate and thick clouds. As already explained, small backscatter may be due to the presence of multi-layered clouds containing thin uppermost layers that MODIS does not detect. It is evident from Fig. 2.7 that weak features associated with thin ice layers (i.e., pixels with low γ' values) are still observed in cumulus and stratocumulus classes.

To investigate the dependence of the cloud δ–γ' relationship on geographic location, we investigate the δ–γ' relationship for three latitude regimes: tropics (30°S to 30°N), midlatitudes (30°N to 60°N and 30°S to 60°S), and high latitudes (60°N to 90°N and 60°S to 90°S). The complete dataset, multiple cloud layers have not been screened out, is used for the geographic analysis. The results for the tropical region are shown in Fig. 2.8. In the tropical region only water phase features are observed for low and middle clouds; however, both water and ice features with patterns quite similar to those shown in the high cloud classes in Fig. 2.5 are observed in the case of tropical high clouds. Horizontally oriented crystals are present only in the cirrostratus cloud class. The majority of the tropical high cloud observations show signatures of randomly oriented ice crystals with depolarization ratios between 0.3-0.5. *In situ* observations of tropical ice clouds show that the shapes of ice crystals within tropical ice clouds, especially those associated with strong deep convection, can be complicated and irregular. Irregular ice crystal shapes would lead to high depolarization ratios and low backscatter values, which could explain the absence of an oriented crystal signature in Fig. 2.8 except for the cirrostratus class.

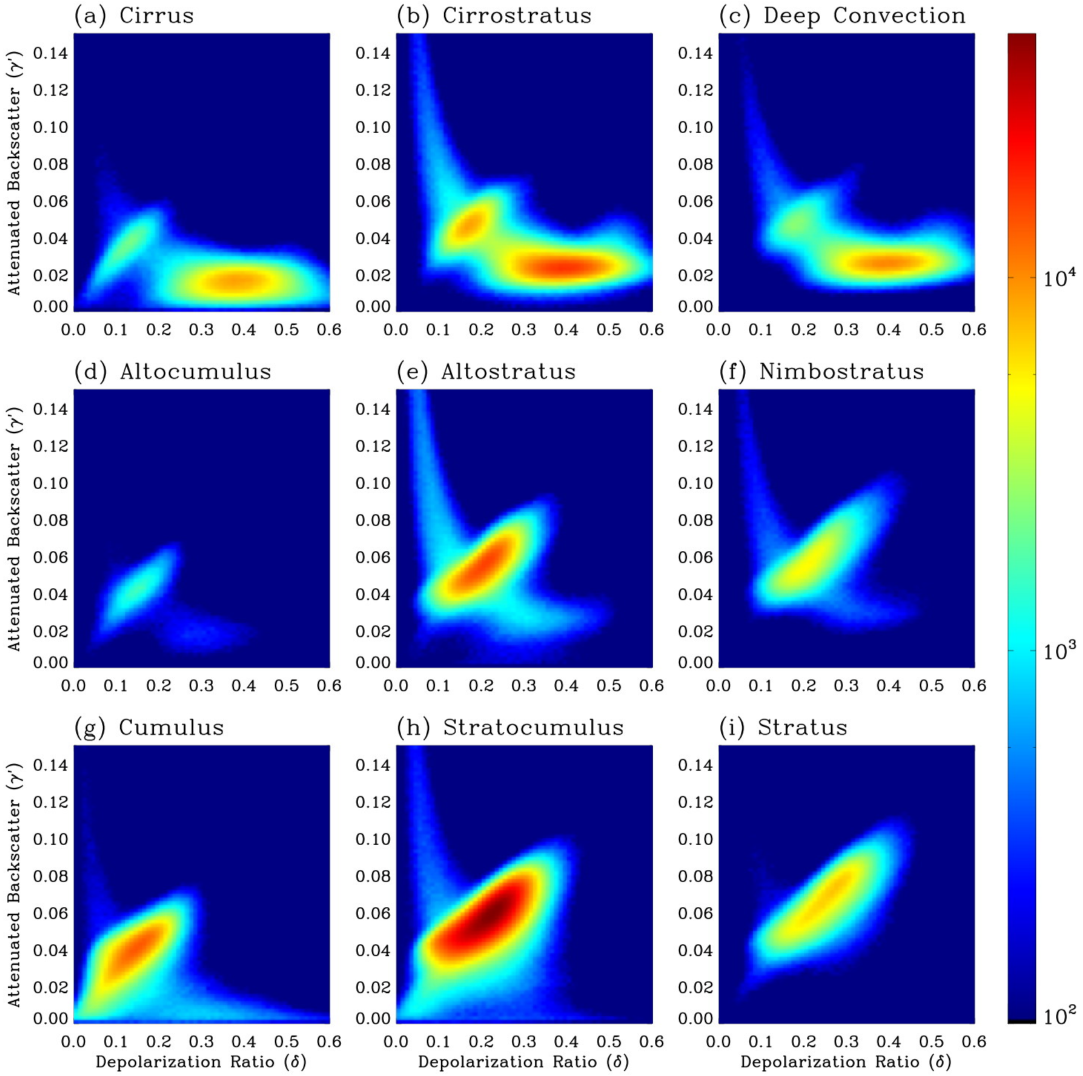

Fig. 2.7 Same as Fig. 2.5 except for single-layer clouds identified from the CALIPSO data.

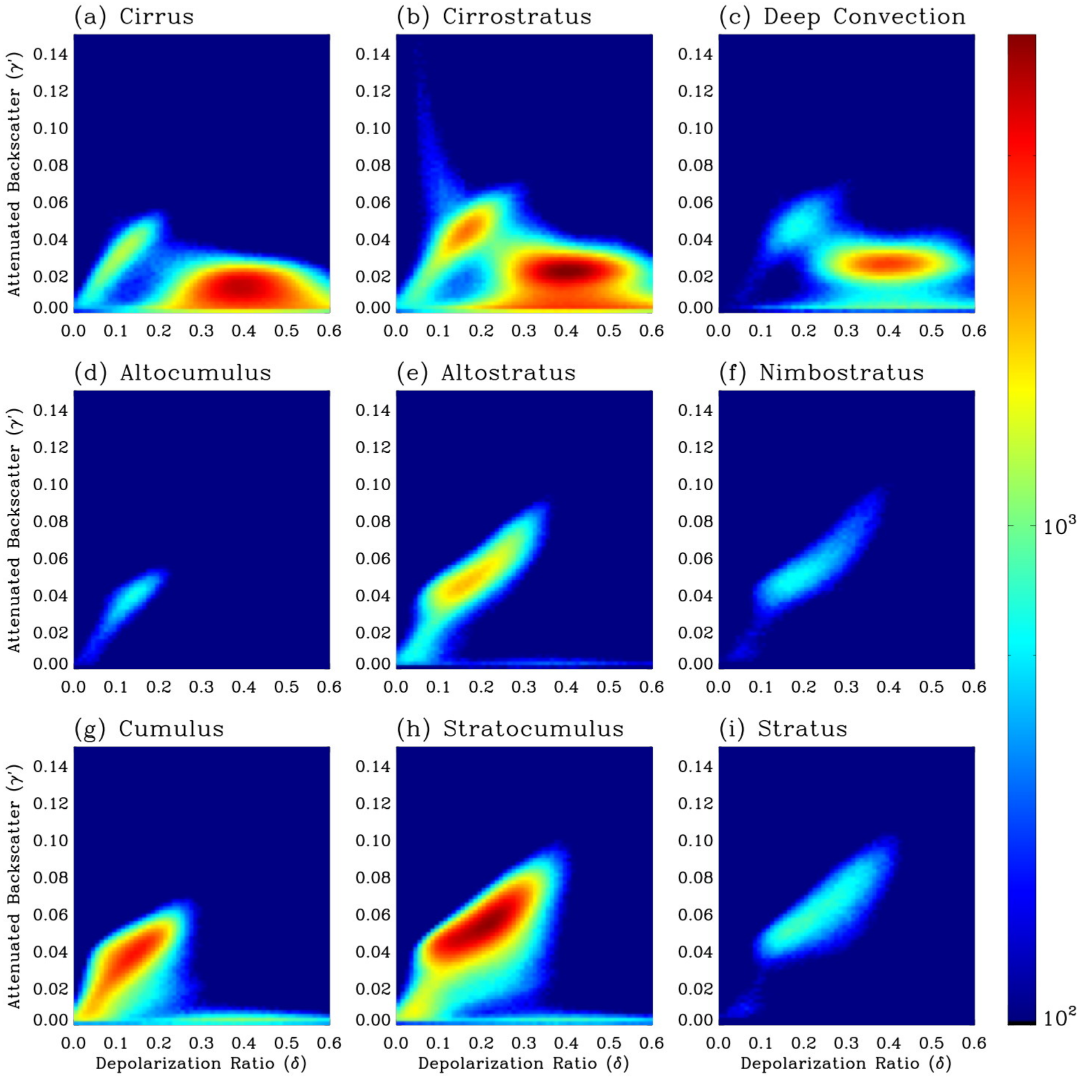

Fig. 2.8 The δ–γ' relations for nine cloud types in the tropical region from 30°S to 30°N.

The δ–γ' relations for the midlatitude regime are shown in Fig. 2.9. For the midlatitude cases, ice signatures are seen in all the cloud classes except for stratus; water signatures are seen in all of the classes. Signatures corresponding to horizontally oriented ice crystals are found more often in the midlatitude cases than in the tropics, and are strongest in the moderate optical thickness classes. Differing from the tropical

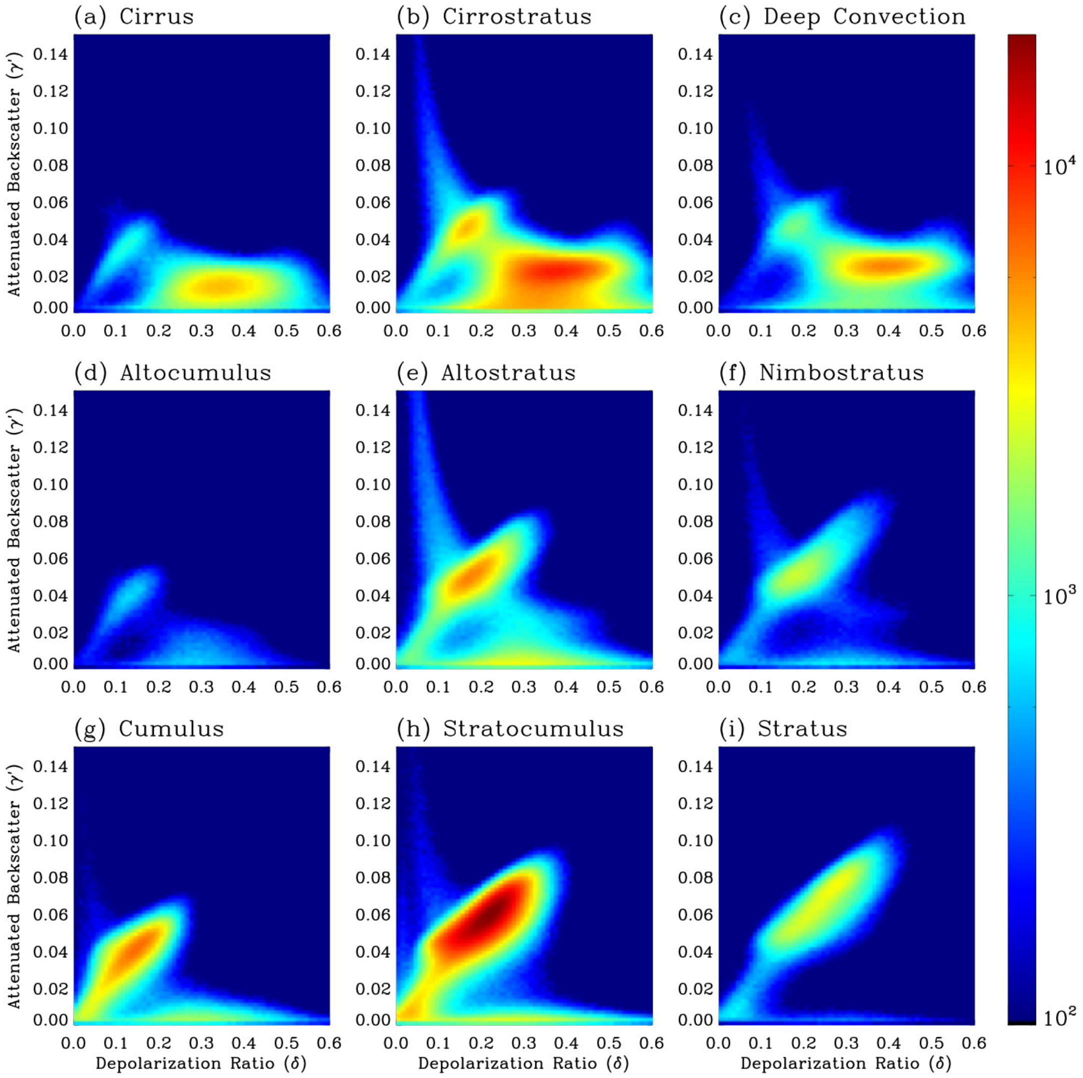

Fig. 2.9 The δ–γ' relation for nine cloud types in the midlatitudes (30°S-60°S and 30°N-60°N).

cloud systems shown in Fig. 2.8, both water and ice phases are observed in midlatitude mid-level clouds. The lack of ice feature in the mid-level tropics may be explained by different temperature ranges with respect to latitude bands. A pressure range of midlevel (440 to 680 hPa) in the midlatitude will cover lower temperature ranges than in the tropics, so the mid-level clouds in the midlatitude regions might contain more ice phase crystals. Additionally, the ice-phase feature is also weakly shown in the δ–γ' relationship for the midlatitude nimbostratus and stratocumulus cloud classes. Furthermore, it is evident from Fig. 2.9 that horizontally oriented ice crystals are present in midlatitude cirrostratus, deep convection, altostratus, nimbostratus, and stratocumulus classes. Pristine ice crystals have been observed in the midlatitudes by aircraft or balloon-borne instruments. If pristine ice plates or columns are horizontally oriented, the corresponding depolarization ratios are low. The existence of ice and water cloud signatures in the midlevel cloud classes may point to mixed-phase clouds, which occur frequently in the midlatitudes, and/or separate cases of water phase and ice phase clouds.

The δ–γ' relations for the polar regions are shown in Fig. 2.10. Overall, the patterns shown in Figs. 2.9 and 2.10 are quite similar. However, the high cloud classes, especially the deep convection class, occur less frequently in the polar regions than in the tropics and midlatitudes. Both water and ice signatures are found in all of the polar classes except for the stratus and cumulus classes. The cirrostratus class has the largest fraction of ice signature, most of which is randomly oriented. Similar to the midlatitude case, all of the moderate optical thickness classes demonstrate the oriented crystal feature. It should be pointed out that the polar region MODIS cloud classes may have more errors than the tropical and midlatitude classes due to the difficulties in MODIS cloud detection and cloud property retrieval over cold, bright surfaces with low solar elevation angles.

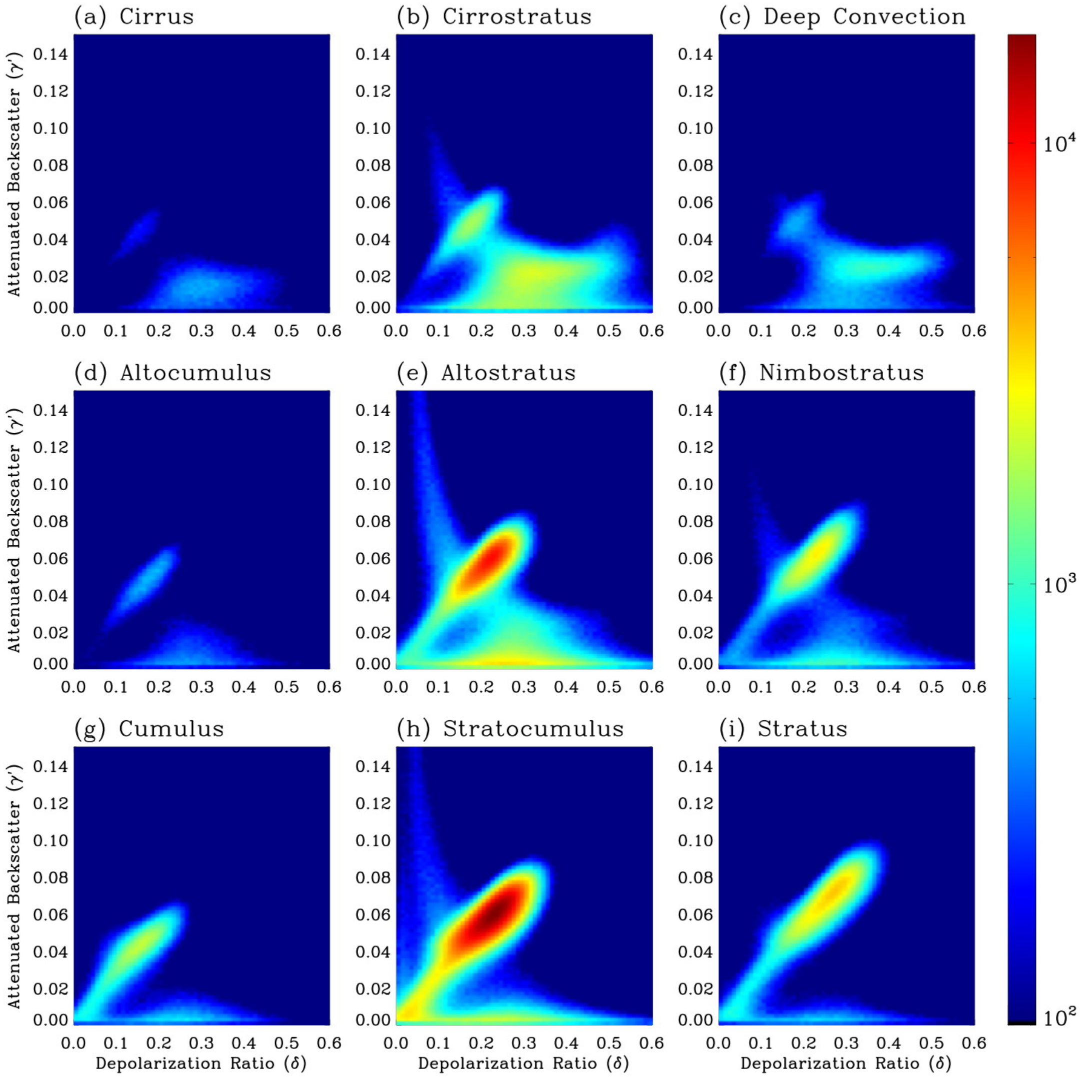

Fig. 2.10 The δ–γ' relationships for clouds in the polar regions (60°S-90°S and 60°N-90°N).

We also consider the relationship between cloud thermodynamic phase and cloud top temperature in Fig. 2.11. The δ–γ' relations from CALIPSO are shown for nine MODIS cloud top temperature retrieval ranges. As expected, the clouds with cloud-top temperatures above 0°C correspond mainly to the water cloud feature in the δ–γ' relation, whereas the clouds with cloud top temperatures below -45°C correspond primarily to the feature associated with randomly oriented ice crystals. However, water features are observed for cloud-top temperatures as cold as -45°C and ice features are noticed for cloud-top temperatures as warm as -5°C. For cloud top temperatures between -5°C and -25°C, the observed ice features correspond to horizontally oriented ice crystals, while both oriented and non-oriented crystal features are seen between -25° and -40°C. Within these temperature ranges, ice crystals and supercooled water drops can occur in single-phase or mixed-phase clouds. An interesting feature is the apparent increase in depolarization ratio with decreasing temperature for randomly oriented ice crystals. The differences between MODIS and CALIPSO retrieved cloud height, especially in the case of thin clouds, may impact these results, as the MODIS cloud top temperatures are inferred from the cloud top pressure retrievals for midlevel and upper level clouds.

The CALIPSO lidar retrievals are independent sources of information about cloud phase that can be compared against the two MODIS-derived cloud phase products described in section 2.3.1. The MODIS bispectral IR cloud phase algorithm results are shown in Figs. 2.12-14, while those from the RPP phase algorithm are shown in Figs. 2.15-17. The global δ–γ' relations for all clouds identified as water phase by the operational MODIS bispectral IR algorithm are shown in Fig. 2.12. In this case, high frequencies of occurrence are observed for the three low cloud classes, as well as two of the middle cloud classes, altostratus and nimbostratus. Comparisons with Fig. 2.5 show that the clouds causing the strong water cloud signatures in the upper level clouds in the

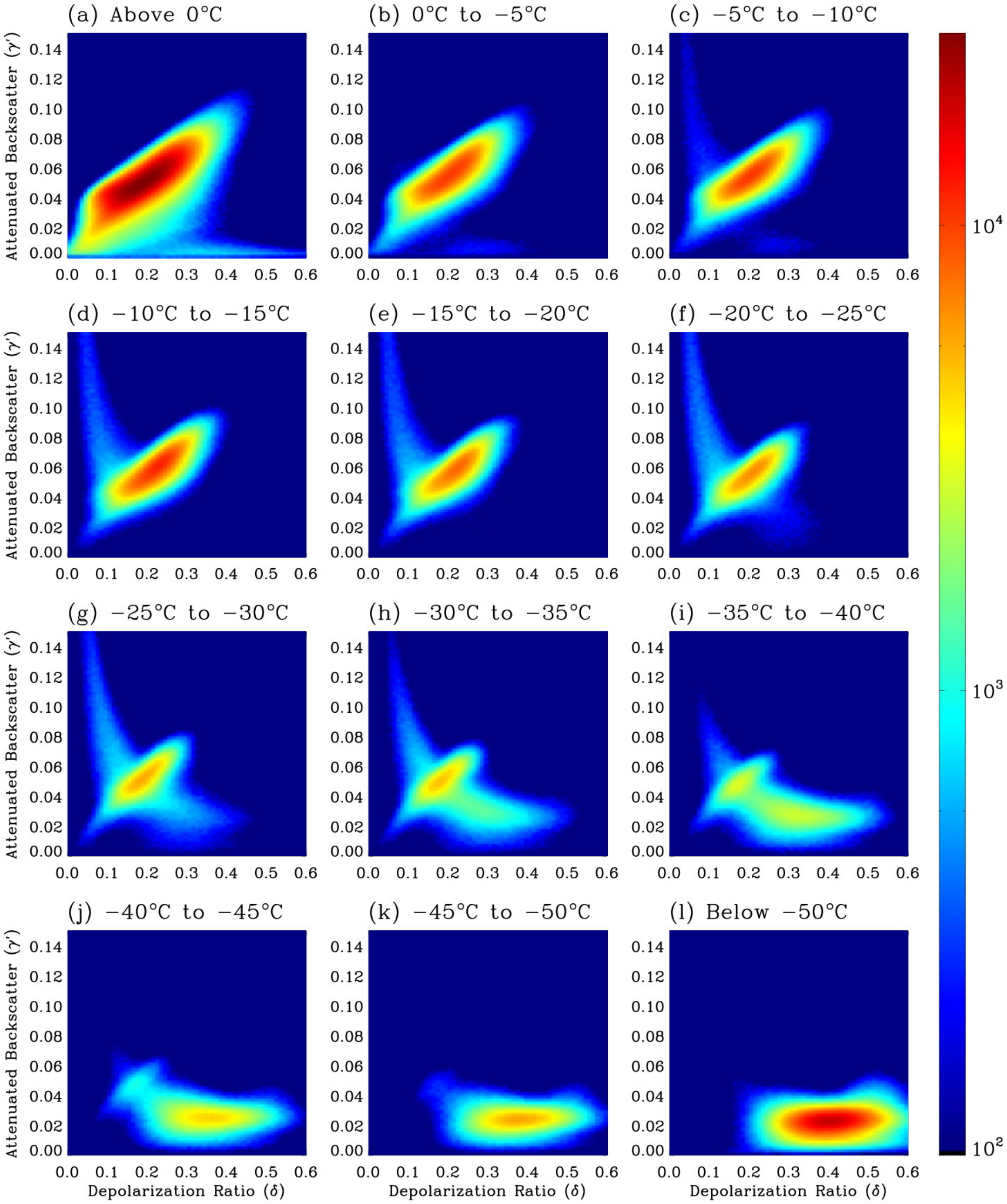

Fig. 2.11 The δ–γ' relationships with respect to cloud top temperature obtained by MODIS cloud retrievals for single-layer clouds identified from the CALIPSO data.

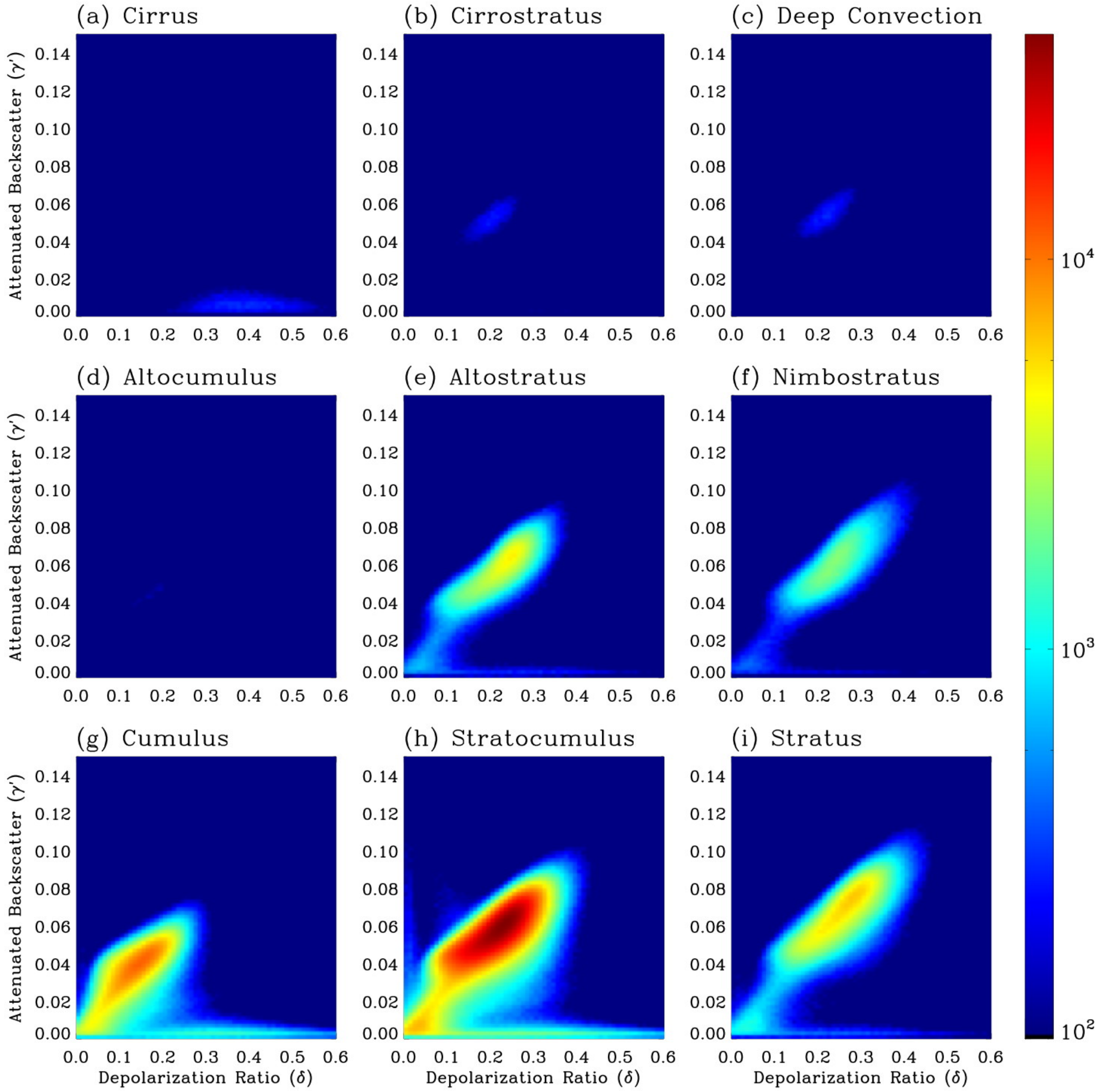

Fig. 2.12 The δ–γ' relationships for the clouds classified as water-phase by the MODIS IR cloud-phase determination algorithm.

entire dataset are not being classified as water by the MODIS IR phase algorithm. There is, however, a weak component of the cirrus class exhibiting a randomly oriented crystal lidar signature that is classified as water by MODIS. Fig. 2.12 shows that the vast majority of clouds classified as water by the MODIS phase algorithm exhibit δ–γ' signatures associated with water clouds.

Figure 2.13 shows the global δ–γ' relations for clouds identified as ice phase by the MODIS IR-phase algorithm. The most obvious feature is that the low cloud classes are not populated. Strong lidar signatures associated with randomly oriented crystals are seen in the high cloud classes, and, to a lesser extent, in the altostratus class. However, the typical water-phase δ–γ' feature is observed in the altocumulus, altostratus, cirrus and cirrostratus classes. These water features may mean that MODIS misclassified some water clouds as ice. There are other possibilities, including mixed-phase clouds, or heterogeneous cloud features (i.e., the co-existence of ice clouds and water clouds) within the MODIS phase 5 km x 5 km footprint.

Figure 2.14 shows the global δ–γ' relations for those clouds identified as mixed and unknown phase by the MODIS IR algorithm. The greatest number of MODIS pixels with this classification fall into the cirrostratus, altostratus, stratocumulus, nimbostratus, and deep convection classes, and both water and ice features are seen in the δ–γ' relations. This is not surprising as the MODIS IR algorithm assigns mixed or unknown phase to clouds with spectral and thermal signatures that do not definitively point to either ice or water phase. Comparisons of Fig. 2.14 to Fig. 2.13 show that clouds exhibiting features associated with horizontally-oriented ice crystals are likely to be classified as mixed or unknown phase by MODIS. This tendency warrants further study.

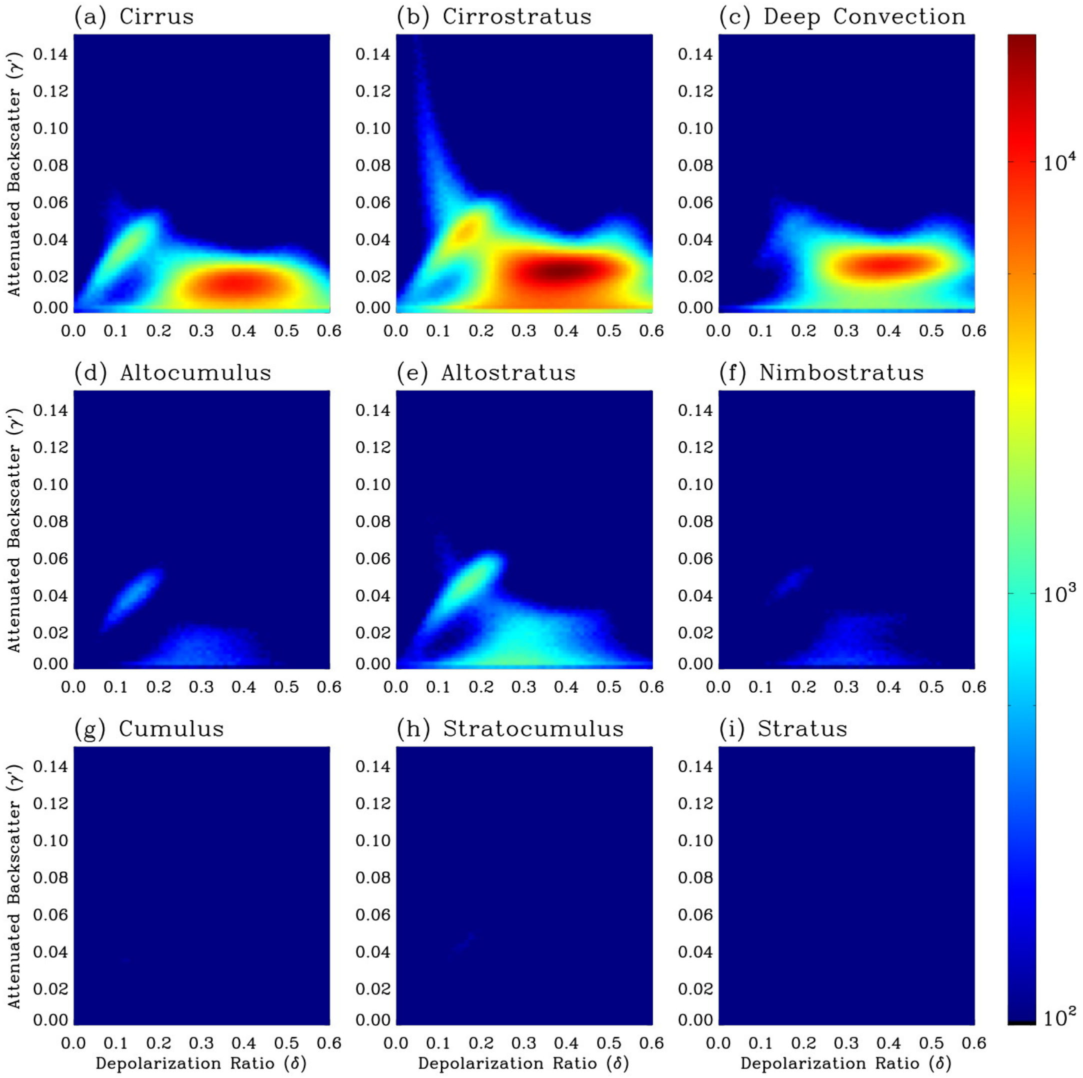

Fig. 2.13 The δ–γ' relationship for the clouds classified as ice-phase by the MODIS IR cloud-phase determination algorithm.

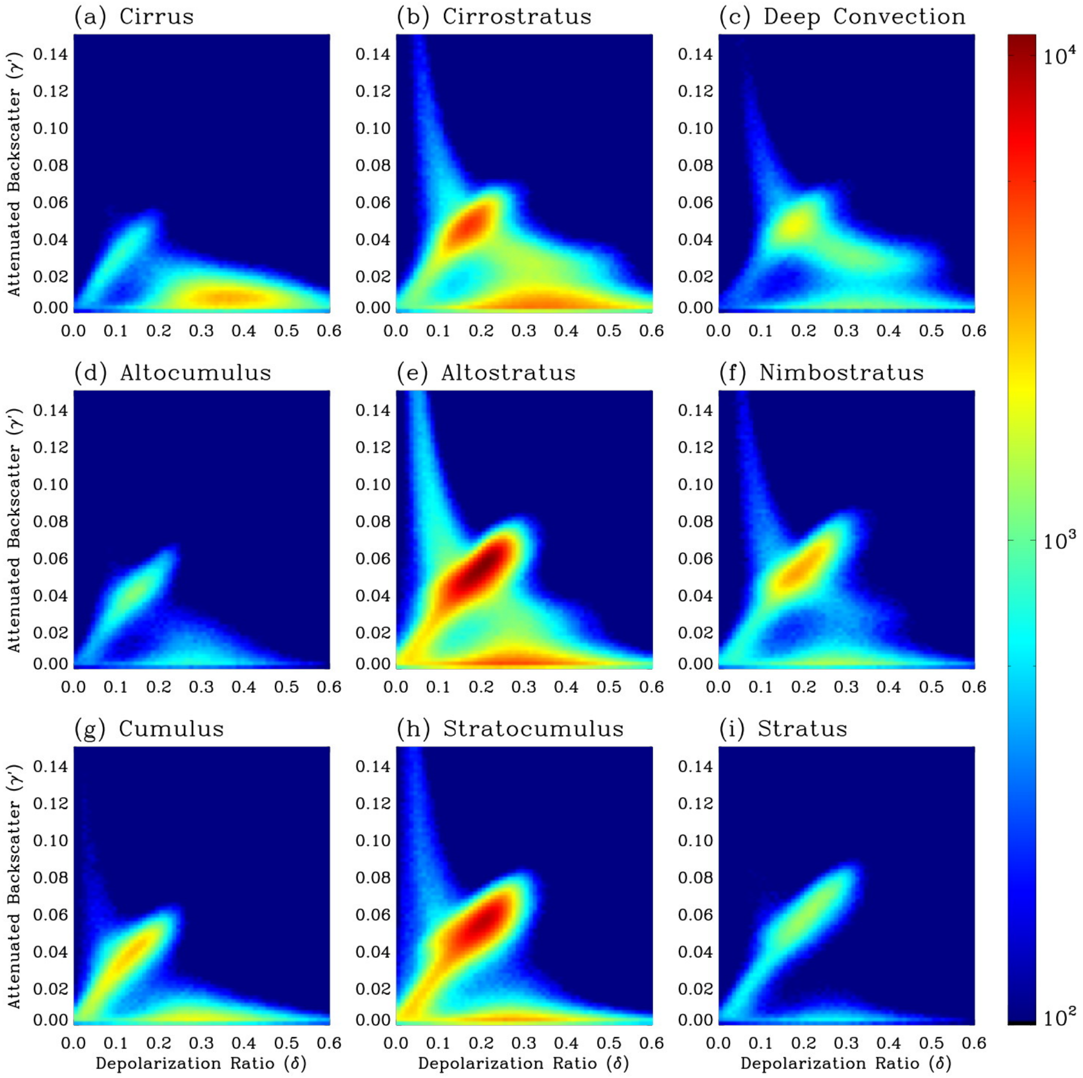

Fig. 2.14 The δ–γ' relationship for clouds classified as mixed- or uncertain-phase by the MODIS IR cloud-phase determination algorithm.

The δ–γ' relations for water, ice, and undetermined phase classifications, based on the MODIS cloud property retrieval processing path (RPP) phase algorithm are shown in Figs. 2.15-17. The RPP phase algorithm utilizes a number of visible, near-infrared, and infrared MODIS channels, but can only be applied to daytime MODIS observations. Fig. 2.15 shows the δ–γ' relations for those clouds classified as water by the RPP. The majority of the clouds classified as water by the RPP demonstrate features indicative of water in the lidar relations, although randomly oriented crystal features are seen in the cirrus and cirrostratus classes, and weak features associated with horizontally oriented particles are seen in the moderate optical thickness classes. This feature is not seen in the MODIS IR phase plot, implying that the IR phase algorithm classifies these scenes as having mixed or unknown phase.

The clouds classified as ice by the MODIS RPP are shown in Fig. 2.16. The δ–γ' relations for the upper level clouds look similar to those for the MODIS IR phase plot in Fig. 2.13. The midlevel cloud features indicative of water clouds are stronger in the MODIS RPP ice case, though, and some low level clouds with water features are classified as ice by the MODIS RPP. More detailed case studies are necessary to understand these features. An interesting note is that the RPP algorithm classifies a much larger fraction of the horizontally-oriented crystal features as ice than does the IR phase algorithm, which tends to classify them as mixed or unknown.

Only a small fraction of the RPP cases are classified as undetermined phase. The δ–γ' relations in Fig. 2.17 show that the midlevel and low level undetermined clouds tend to demonstrate strong water features, while the cirrus class shows moderate ice features. Several classes, cirrostratus, deep convection, and altocumulus, are basically unpopulated.

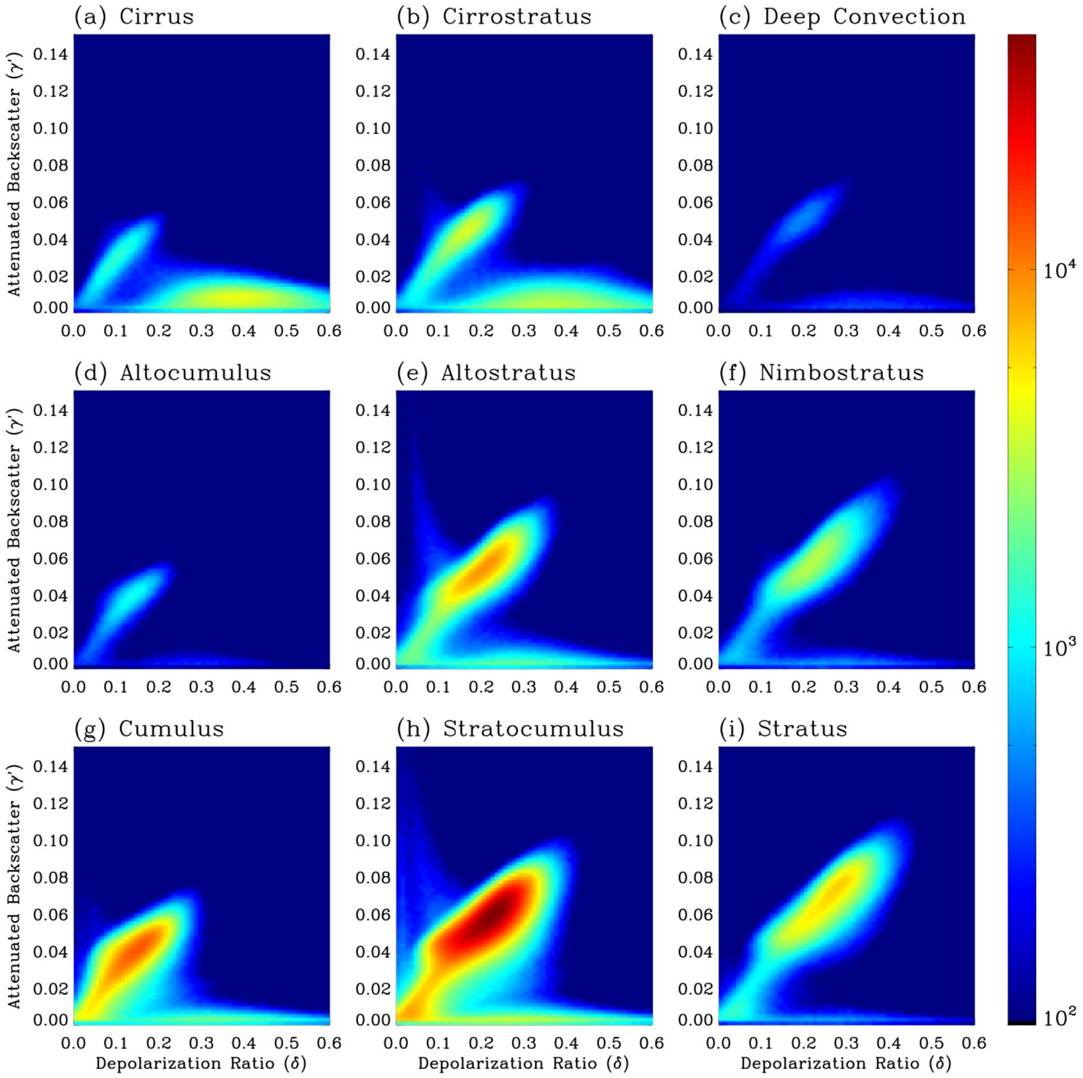

Fig. 2.15 The δ–γ' relationship for clouds classified as water-phase by the MODIS cloud property retrieval processing path (RPP) phase determination algorithm.

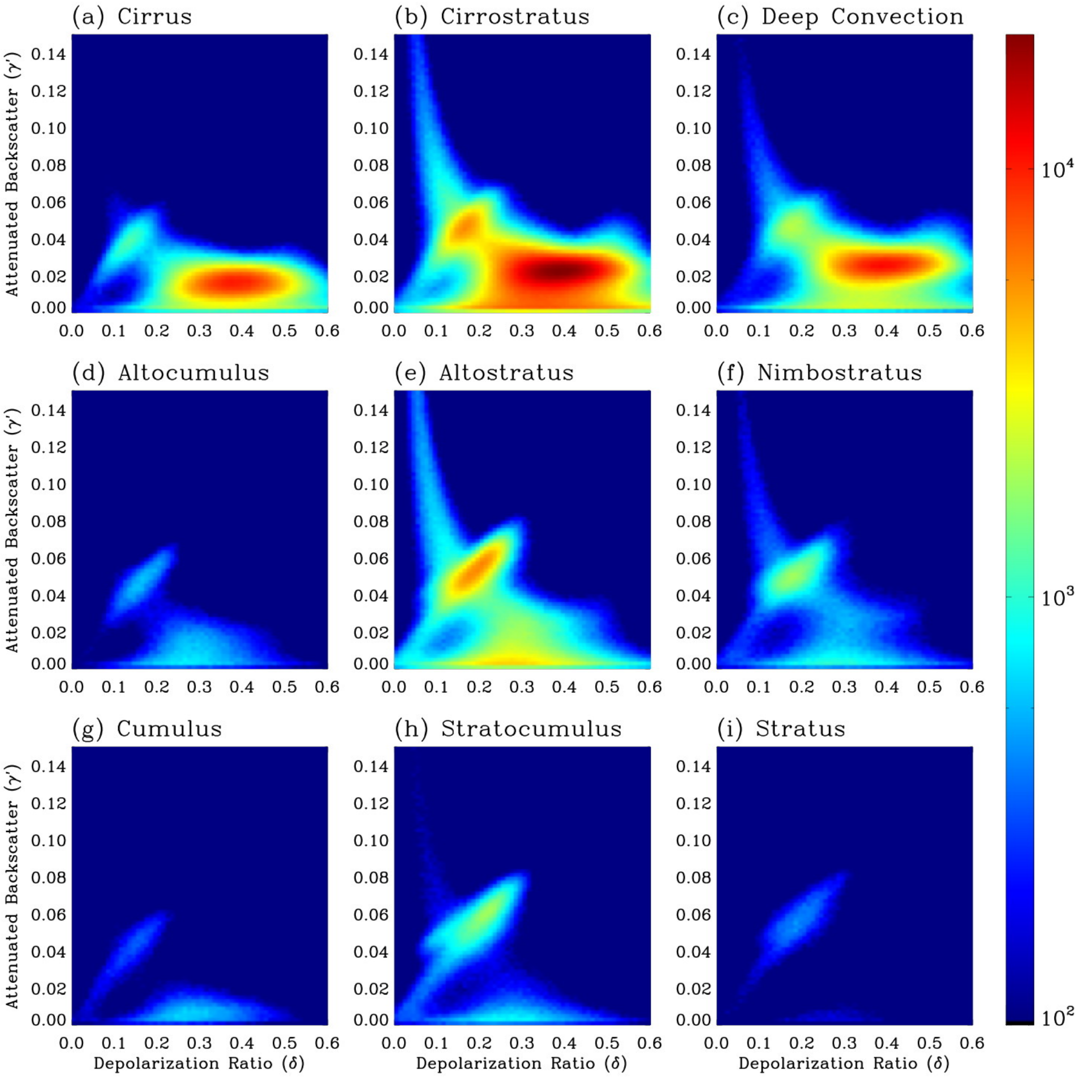

Fig. 2.16 The δ–γ' relationship for clouds classified as ice-phase by the MODIS RPP phase determination algorithm.

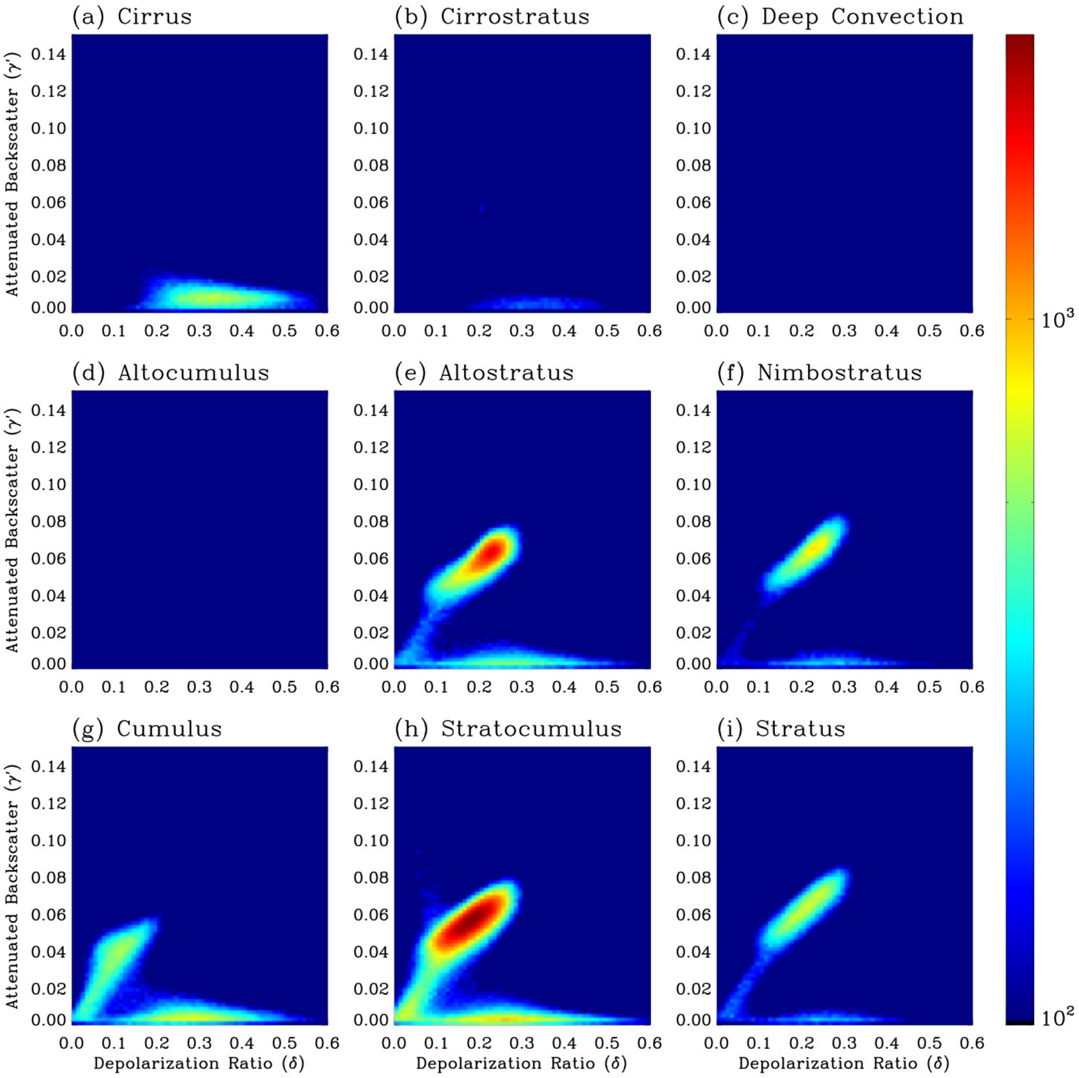

Fig. 2.17 The δ–γ' relationship for clouds classified as undetermined-phase by the MODIS RPP phase determination algorithm.

Figures 2.18, 2.19 and 2.20 show the δ–γ' relations for single-layered water, ice, and mixed-/uncertain-phase clouds, respectively, which are identified on the basis of the MODIS bispectral IR phase algorithm. The unscreened counterparts of Figs. 2.18, 2.19 and 2.20 are Figs. 2.12, 2.13 and 2.14, respectively. Again, the overall features in the δ–γ' relations shown in the screened and unscreened cases are similar; however, low γ' values associated with the uppermost thin clouds are eliminated in the screened results. Furthermore, it seems likely, based on comparison of Figs. 2.20 and 2.14, that many clouds identified as mixed- or uncertain-phase by the MODIS IR algorithm have more than one layer.

2.3.3 Conclusion

We investigated the relationships between layer-averaged depolarization ratio (δ) and layer-averaged attenuated backscatter (γ') measured by the CALIPSO lidar for nine ISCCP cloud classes applied to MODIS data. These results were published in Cho et al. (2008). To summarize, the CALIPSO lidar contains information on up to 10 cloud layers within each 1 km retrieval footprint; however only the uppermost cloud layer is considered in this study. The cloud class assignment was made on the basis of the MODIS retrievals of cloud-top pressure and cloud optical depth for a period of 12 months from July 2006 to June 2007. Because the study depends on MODIS optical depth retrievals, only daytime observations are included. On a global scale, the CALIPSO lidar δ–γ' relation associated with water clouds is observed for all nine cloud types. The δ–γ' feature associated with horizontally oriented ice crystals is prominent for

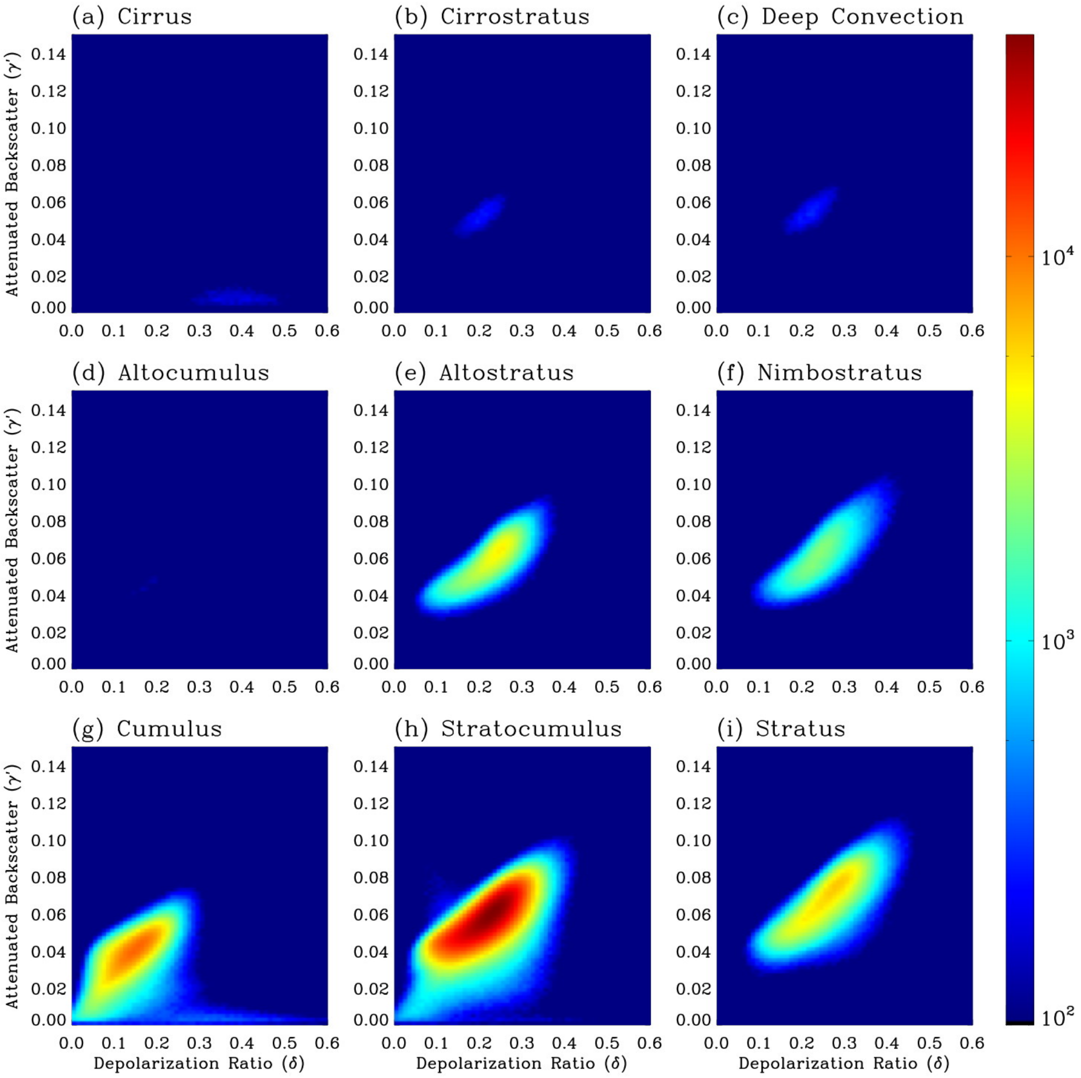

Fig. 2.18 Same as Fig. 2.12 except for single-layer clouds identified from the CALIPSO data.

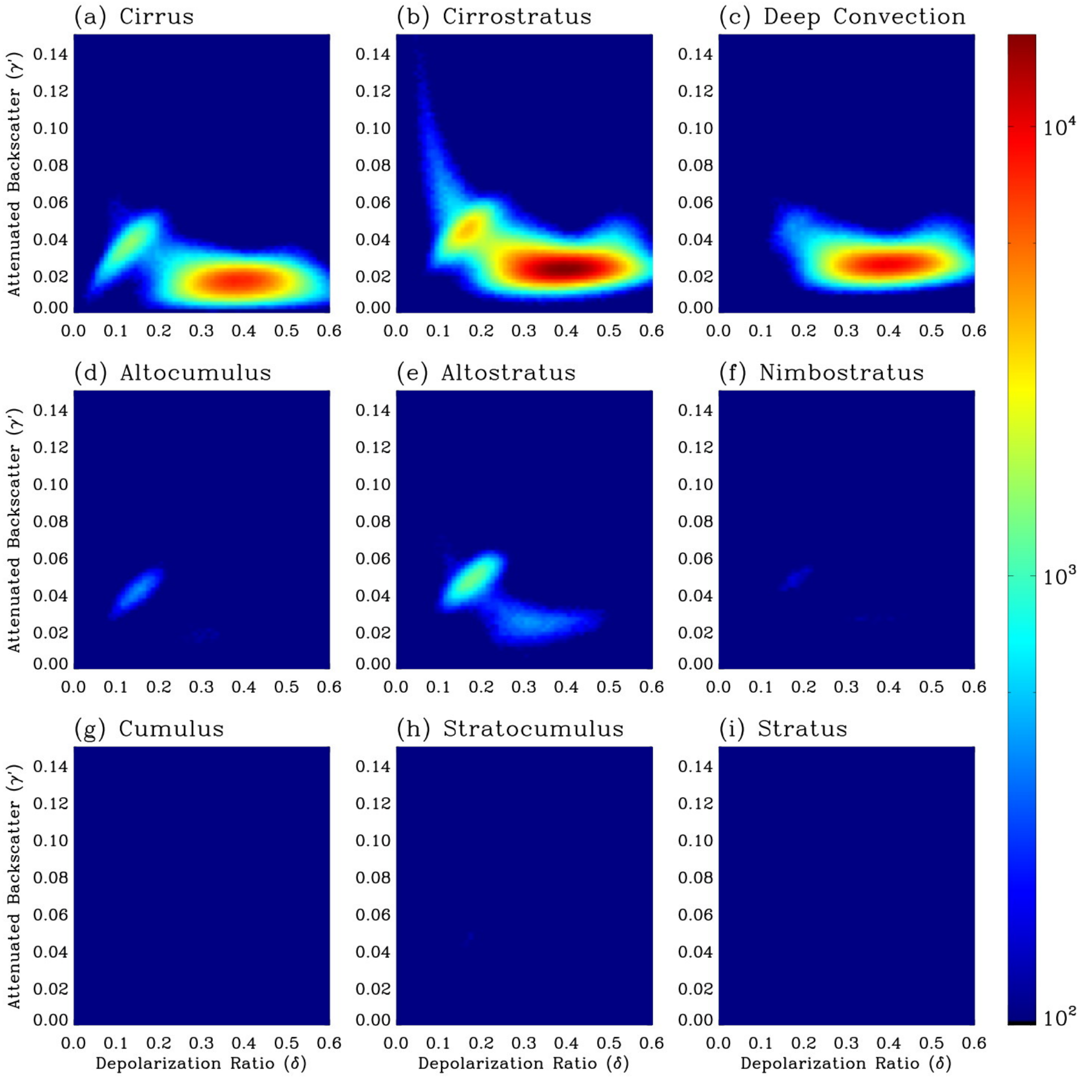

Fig. 2.19 Same as Fig. 2.13 except for single-layer clouds identified from the CALIPSO data.

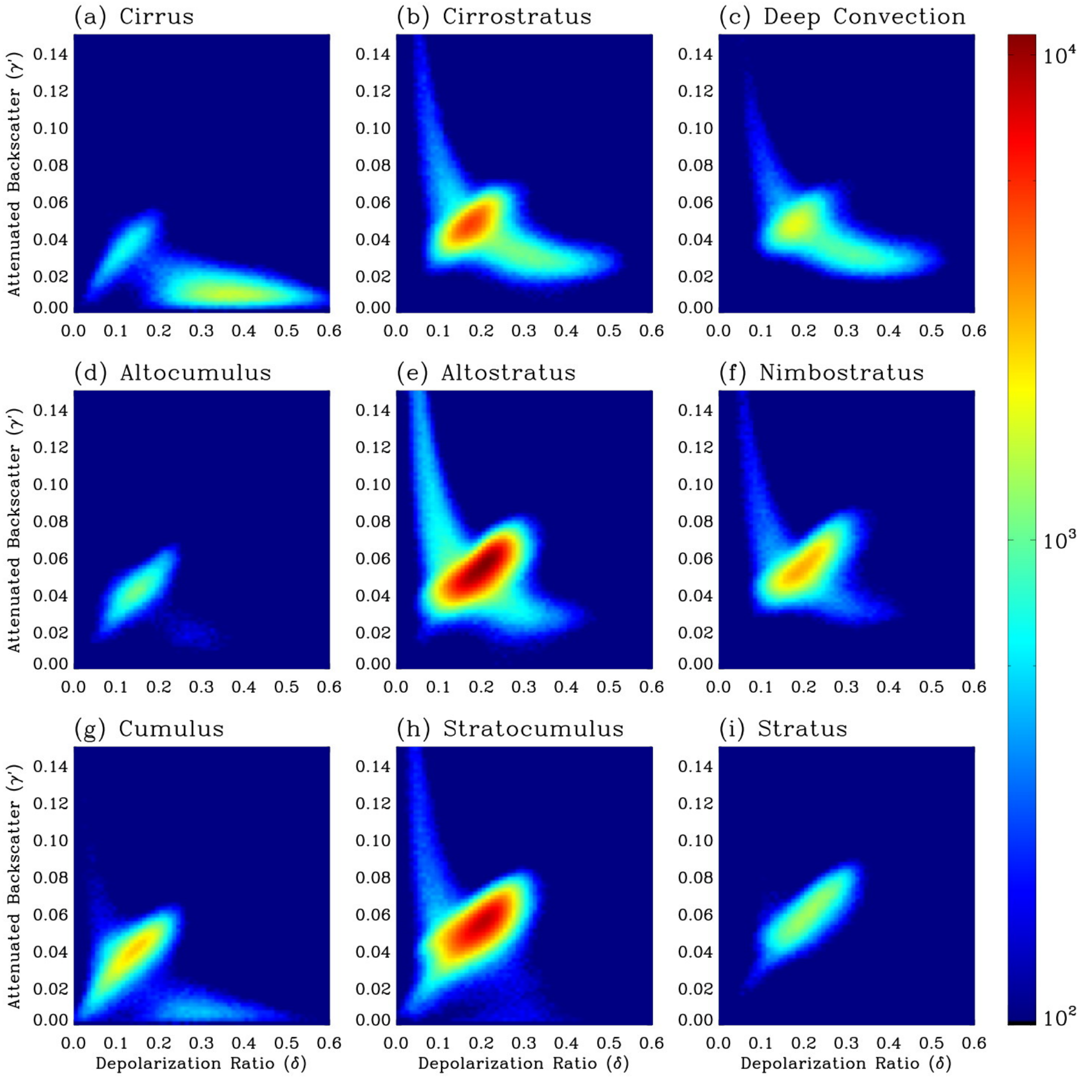

Fig. 2.20 Same as Fig. 2.14 except for single-layer clouds identified from the CALIPSO data.

cirrostratus, deep convection, altostratus, and nimbostratus classes. Furthermore, we screened both the MODIS and CALIPSO data to eliminate the cases in which two or more cloud layers were observed. It is shown that very low γ' values in the unscreened case were largely eliminated in the case of single-layered clouds. These low γ' values correspond to the uppermost thin layers in two- or multi-layered cloud systems.

The dependence on latitude was also considered. For the tropical region (30ºS-30ºN), only the water-phase feature is observed in the CALIPSO lidar δ–γ' relation for low and mid-level clouds; however, both water-phase and ice-phase signatures are observed for high clouds. In the midlatitude and polar regions, both water-phase and ice-phase are observed for high and middle clouds. Additionally, the feature associated with horizontally oriented ice crystals is prominent for cirrostratus and altostratus clouds. In addition to the analysis of the CALIPSO lidar δ–γ' relation for cloud systems at three latitude belts, we also analyzed the lidar δ–γ' relations for various cloud top temperatures. Randomly oriented ice crystal features correspond to colder cloud top temperatures than horizontally oriented crystals. Additionally, the depolarization ratio associated with randomly oriented ice crystals increases for colder cloud top temperatures.

We investigated the CALIPSO lidar δ–γ' relationship with respect to the cloud phase determined from both the operational MODIS bi-spectral infrared phase algorithm and the MODIS cloud optical properties retrieval processing path phase algorithm. It is shown that the MODIS bi-spectral IR algorithm is consistent with that indicated by the CALIPSO lidar δ–γ' relationship for water clouds. However, the typical feature associated with water phase in the δ–γ' relationship is observed for the clouds that are identified as ice by the MODIS IR algorithm. Both water and ice signatures are observed for those clouds classified as mixed or unknown phase by the MODIS IR algorithm. On the other hand, the RPP algorithm misclassifies a lot of ice clouds as water clouds (Figs. 2.15-16). Although the MODIS IR algorithm is generally more conservative in its phase classification for most cloud systems, the RPP algorithm is more effective in detecting ice clouds consisting of horizontally oriented ice crystals, as evident from a comparison of Figs. 2.13 and 2.16. The present results clearly demonstrate the unique capabilities of the CALIPSO lidar instrument for determining cloud phase.

2.4 CALIPSO Lidar δ–γ' Relations for Different Aerosol Types

Here, we demonstrate the CALIPSO lidar δ–γ' relationships for different aerosol subtypes. The CALIPSO aerosol sub-typing algorithm uses the integrated attenuated backscatter at 532 nm and the particulate depolarization ratio with an aid of surface types and layer elevation to identify aerosol type from among one of the six types (i.e. Clean Marine, Clean continental, Polluted continental, Dust, Polluted dust, Smoke (biomass burning)). For example, aerosol layers having particulate depolarization ratio greater than 0.2 are classified as dust except for polar region. More detailed descriptions of the algorithm are given in Omar et al. (2009).

Fig. 2.21 shows the CALIPSO lidar δ–γ' relationships for six aerosol sub-types observed in 2008. The attenuated backscatters and depolarization ratios of aerosols are much smaller than that of clouds. Actually, Cloud-Aerosol discrimination (CAD)

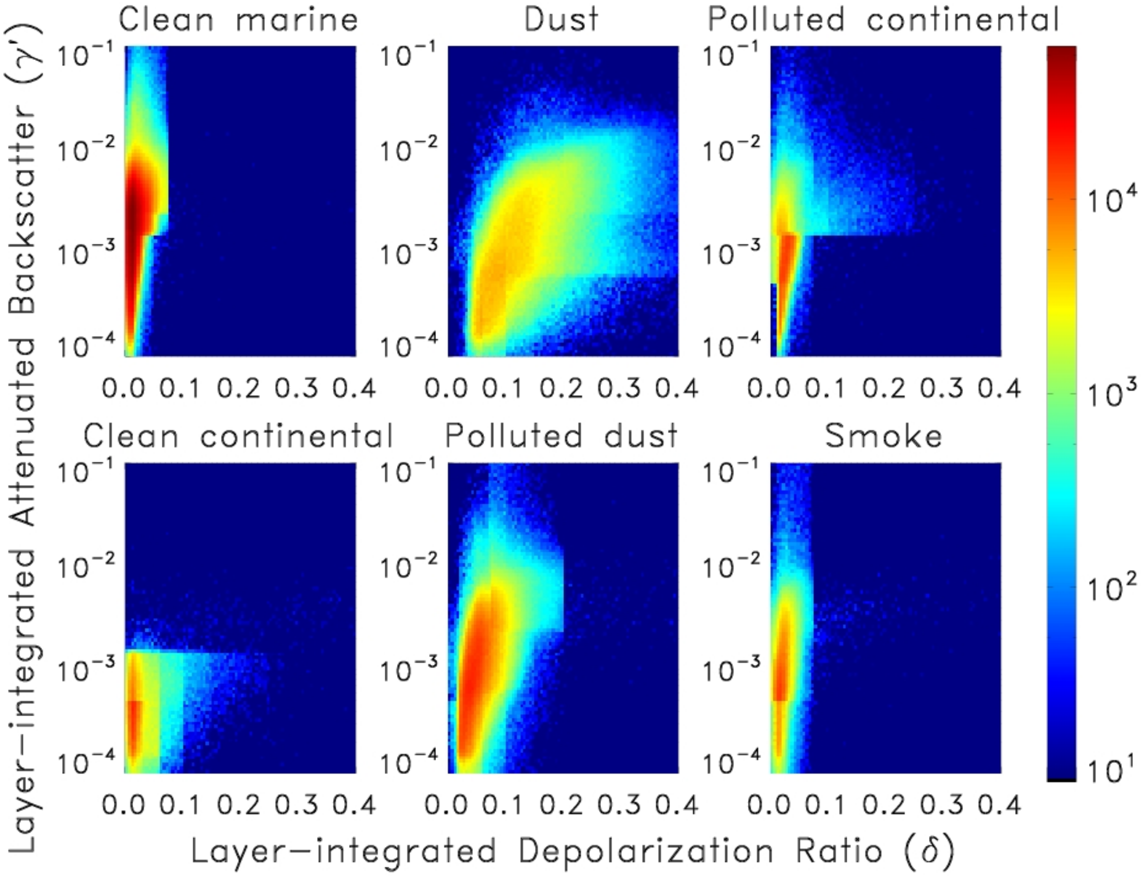

Fig. 2.21 The CALIPSO lidar δ–γ' relationships for six aerosol sub-types observed in 2008. The color of each pixel represents the frequency of occurrence for a $\Delta\delta$–$\Delta\gamma'$ box with 0.01 by 0.002 sr^{-1} interval.

algorithm (Liu et al. 2009) uses these two parameters to distinguish cloud and aerosol based on the statistical differences. The attenuated backscatter of dust is within almost same ranges as others except for clean continental types. However, due to its nonspherical characteristics, only dust type has larger depolarization ratio rather than other aerosol types. Thus, dust aerosol type can be well separated from other aerosol types, except for the thick dust, which has similar depolarization ratio of cirrus cloud.

Therefore, CALIPSO aerosol products are used to evaluate the MODIS dust detection algorithms in section 4.

2.5 Summary

In this section, we introduce spaceborne polarization lidar, CALIPSO lidar, and demonstrate its unique capabilities by presenting the relationships between lidar backscatter and the corresponding depolarization ratio for different cloud classifications and aerosol subtypes.

3. AN EVALUATION OF THE COLLECTION 5 MODIS IR CLOUD PHASE RETRIEVAL[*]

In this section, I review the work published in Cho et al. (2009). This paper evaluates the MODIS IR cloud phase retrieval using the collocated CALIPSO cloud products. As mentioned in section 1, the possible misclassifications of MODIS cloud phase (Nasiri and Kahn, 2008) are tested.

3.1 Introduction

This study, which can be viewed as a follow-up to Nasiri and Kahn (2008), henceforth referred to as NK08, mainly focuses on the evaluation of cloud thermodynamic phase retrieval based on infrared-channels using independent lidar observations. The expansion of the A-train satellite constellation to include the CALIPSO satellite provides an opportunity to address the deficiencies of the earlier study. With the observations made by CALIPSO lidar, it is feasible to test three of the four NK08 hypotheses (numbers 1, 2, and 4). The previous section has already shown the usefulness of combining MODIS and CALIOP products for cloud studies. They classified clouds using MODIS-retrieved cloud top height and optical thickness and looked at the CALIOP layer-integrated backscatter and depolarization ratio relationships. The previous section has showed that liquid water, randomly-oriented, and

---

[*] Reprinted with permission from “Application of CALIOP measurements to the evaluation of cloud phase derived from MODIS infrared channels” by H.-M. Cho, S. L. Nasiri, and P. Yang, 2009. *J. Appl. Meteorol. Clim.*, 48(10), 2169-2180, Copyright by American Meteorological Society (AMS).

horizontally-oriented ice crystal signatures were frequently observed in the MODIS data for mid-level and upper-level clouds.

The rest of this section is organized as follows. In section 3.2, we discuss the MODIS instruments and IR phase algorithm. In section 3.3, the CALIPSO cloud layer products used in our analysis are presented, and in section 3.4 we present the present evaluation of MODIS IR cloud phase. The summary and conclusions are given in section 3.5.

3.2 MODIS IR Phase

MODIS (Barnes et al. 1998) is a 36-channel cross-track scanning radiometer with a spectral coverage between 0.4 and 14.5 μm and spatial resolutions between 250 m and 1000 m, depending on channel. While there are two MODIS instruments currently in orbit, this study focuses on the instrument on the Aqua satellite, launched in May of 2002. The MODIS instrument scans out to ± 55 degrees off nadir, but here we consider only MODIS data collocated with CALIPSO data. The MODIS infrared cloud phase product is one of a set of infrared-based cloud products available at 5x5 km resolution including cloud-top pressure (Menzel et al. 2008), cloud-top temperature, and cloud effective emissivity (Platnick et al. 2003) in the MYD06 cloud product files. Cloud retrievals are only performed on those pixels determined to be cloudy by the MODIS cloud mask (MYD35, Frey et al. 2008).

The MODIS Collection 5 infrared phase classification algorithm uses the brightness temperature difference (BTD) between channels centered at 8.5 μm and 11.0

μm (MODIS channels 29 and 31, respectively), as well as the brightness temperature (BT) at 11.0 μm to infer cloud thermodynamic phase (Platnick et al. 2003; Nasiri and Kahn 2008). The bi-spectral algorithm is based on the premise that the [8.5 - 11 μm] BTD tends to be positive for ice clouds and negative for water clouds. Like many cloud phase algorithms, there are a priori assumptions of relationships between cloud temperature and cloud phase. In the case of the MODIS algorithm, pixels with very cold 11-μm brightness temperatures (11 μm BT ≤ 238 K, in the current version) are assumed to be ice. This works because the 11-μm BT of a cloudy scene is usually warmer than the cloud top temperature due to contributions to the radiance from the surface and the atmosphere. Optically thin cirrus clouds, even very cold clouds, may have warm 11-μm BTs, and therefore must be classified by the [8.5 - 11 μm] BTD, rather than by the 11-μm BT.

The MODIS bi-spectral IR phase algorithm has four possible cloud phase classifications: ice, water, mixed, and unknown. NK08 tends to lump the mixed and unknown classifications together because of a lack of evidence that the mixed classification implied truly mixed-phase clouds, but in the present study we consider the classifications separately. NK08 describes the MODIS algorithm as conservative because over 20% of pixels in the data from the January 2005 case are classified as unknown (14.4%) or mixed (8.5%) phase.

3.3 CALIPSO Cloud Layer Product

In this study, the CALIPSO 5-km cloud layer product (version 2.01) is used. In this product, information about up to 10 cloud layers is available at a 5-km spatial resolution. We use the cloud layer boundaries, mid-layer cloud temperature, and cloud phase classification products in this study. An important note about the 5-km cloud layer product cloud layer boundaries is that it is possible for one cloud to be split up into multiple vertically contiguous or overlapping layers, based on vertical variations in the attenuated backscatter and the complex spatial averaging employed in the feature detection algorithm (Vaughan et al. 2009). The mid-layer cloud temperature is determined by calculating the atmospheric temperature at the geometric midpoint of the layer using temperature from the GEOS-5 data product provided to the CALIPSO project by the NASA Global Modeling and Assimilation Office (GMAO) Data Assimilation System.

The CALIOP cloud phase classification is archived in the “Feature Classification Flag” scientific data set. The CALIPSO cloud layer product phase retrieval algorithm is based on a combination of the relationships between the depolarization ratio and attenuated backscatter, the mid-layer cloud temperature, and attenuated backscatter thresholds. A more detailed description of the algorithm is given in the CALIPSO Scene Classification ATBD (Liu et al. 2005). The cloud phase retrieval is, at the time of this writing, still considered to be a beta-version product, and is subject to revisions in later versions. Additionally, there is a known bug in the cloud phase classification in which certain clouds with mid-layer cloud temperatures greater than 0°C are classified as ice.

We have corrected this bug in our analysis by setting the CALIPSO phase of clouds with mid-layer temperatures greater than 0°C to be water[1]. The phase classification currently has three categories: water, ice, and unknown. While the scientific data set contains a placeholder for mixed-phase classifications, it was not been implemented in the 2.01 version.

3.4 Comparisons between MODIS and CALIPSO Cloud Phase Products

This study uses six months of both daytime and nighttime MODIS and CALIPSO data between 85° north and south from January through June 2008 when the lidar view angle is 3° off nadir. Note that this is a different time period from the analyses in section 2 and that because the lidar view angle is now 3° off-nadir, high attenuated backscatter from horizontally oriented ice crystals is no longer common. We have made three modifications to the output from the 5-km cloud layer product. The first, discussed in section 3.3, is the correction of the warm ice cloud bug in the phase product. The second modification is the combination of cloud layers that are overlapping or have small vertical separations into single layers. Vertically contiguous or overlapping cloud layers are an expected result of the CALIPSO iterative feature detection algorithm (Vaughan et al. 2009) stemming from its use of progressive scanning at different spatial resolution to detect faint features. In the operational CALIPSO 5-km cloud layer product, approximately 50% of multi-layer profiles have vertical separations of less than 200 m, and 47% have separations less than 100 m, as shown in Figure 3.1. Note that the

---

[1] The bug has been corrected in the current version 3 product, but the results shown here were published using version 2.01 data.

majority of layers have virtually no separation. While this is not unsurprising based on the feature detection algorithm, it does mean that clouds that a user of the product considers to be single-layer might have two or more layers in the 5-km CALIPSO cloud product. For this study, layers with vertical separations of less than 200 m are combined and are considered to be a single layer. In the case that the two layers have different cloud phases (i.e. water and ice), we describe the layer as mixed-uncertain phase with respect to the CALIPSO cloud phase. This mixed-uncertain phase classification, our third modification, should not be confused with the unused mixed-phase scientific data set in the CALIPSO 5-km cloud layer product.

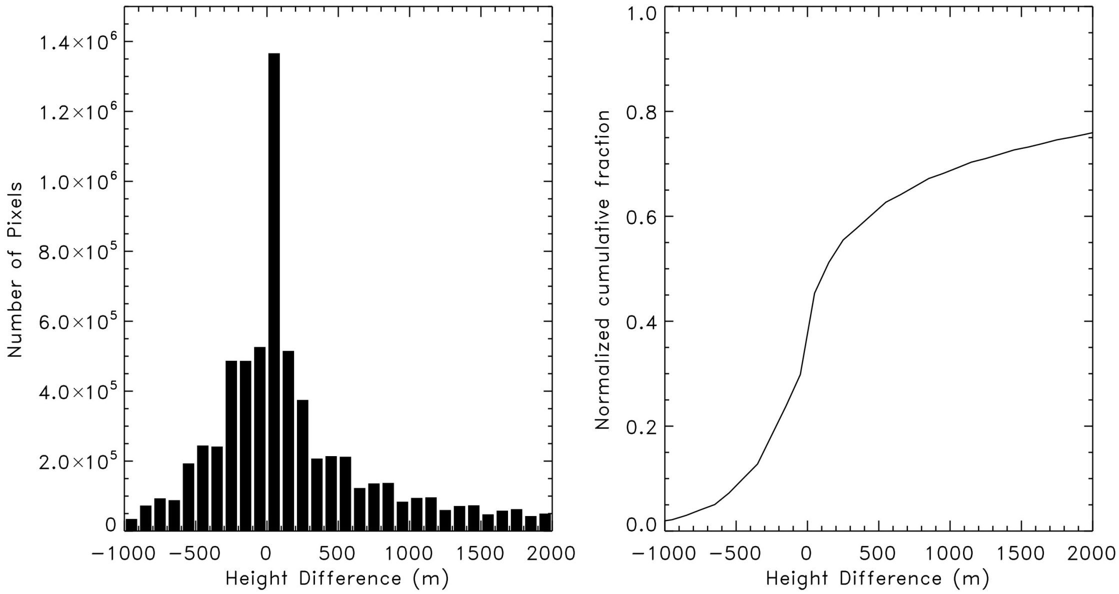

Fig. 3.1 Difference in height between adjacent layers in the CALIPSO 5-km cloud layer product from January to June 2008. The left figure shows the distribution layer separations while the right figure shows the normalized cumulative distribution.

The collocation is based on matching CALIPSO pixels to the nearest MODIS pixels for 5 km MODIS resolution by minimizing the root-mean-square latitude and longitude difference of the centers of the scenes. In this study, CALIPSO 5 km data are used as the “reference” for comparisons with the MODIS products. No cloud-height and MODIS zenith angle-based parallax correction is done in this study, thus introducing the potential for collocation errors (e.g. Holz et al. 2008). These errors will be small for low clouds or high latitude clouds, but could be up to 5 km for high clouds in the tropics.

The MODIS IR phase retrievals are compared with the CALIPSO products in several ways. Results are broken into four categories based on characteristics of the CALIPSO data: the top cloud layer of the entire CALIPSO data set, single-layered clouds, opaque single-layered clouds, and transparent single-layered clouds. CALIPSO cloud detection is considered “truth” in this study; therefore excluding cases for which MODIS detects a cloud but CALIPSO does not. Holz et al. (2008) found that those cases were only 15% of collocated scenes. Because passive IR observations are more sensitive to upper clouds, only the top CALIPSO cloud layer is considered in the comparisons. Those CALIPSO retrievals with only one layer after our 200-m separation correction has been applied are considered to be single-layered. The single-layered category is further split into opaque cloud layers (those for which there is no ground return), and transparent cloud layers (those with a ground return). These categories are considered in our comparisons of MODIS cloud phase retrievals to CALIPSO cloud products in terms of number of pixels classified, cloud top height, cloud top temperature, cloud latitude, and CALIPSO cloud phase.

Figure 3.2 shows the distribution of MODIS IR phase retrievals for single-layer clouds detected by CALIPSO with respect to CALIPSO retrieved cloud top height (a, c, and e) and mid-layer cloud temperature (b, d, and f). As discussed above, retrieved CALIPSO cloud layers that are separated by less than 200 m vertically have been combined into a single layer. To simplify the comparisons, we consider only single-layer clouds, which are approximately 54% of the total CALIPSO cloudy scenes. Figure 3.2a shows that the majority of single-layer clouds detected by CALIPSO have cloud top heights lower than 4 km. Unsurprisingly, the majority of these low clouds are classified as water by MODIS, with a sizable number of scenes not detected as cloudy by MODIS. The majority of higher clouds are classified as ice by MODIS.

A further separation of the single-layer clouds into opaque and transparent clouds shows that 95% of clouds not detected by MODIS are transparent clouds; most of these have tops below 4 km, but are fairly evenly distributed with respect to height above 4 km. This raises the possibility of aerosol contamination in the low level CALIPSO clouds. More transparent high clouds appear to be missed by MODIS than classified as any other single phase. The opaque low clouds tend to be classified as water, with some as unknown. There is a peak in the MODIS classification of mixed-phase clouds around 5 km, and the majority of opaque clouds above 8 km are classified as ice. While the strength of the water cloud peak masks it somewhat, the comparisons with respect to cloud height do support the NK08 interpretation that midlevel clouds are likely to be classified as mixed or unknown by MODIS, but it also shows a sizable number of low clouds classified as unknown.

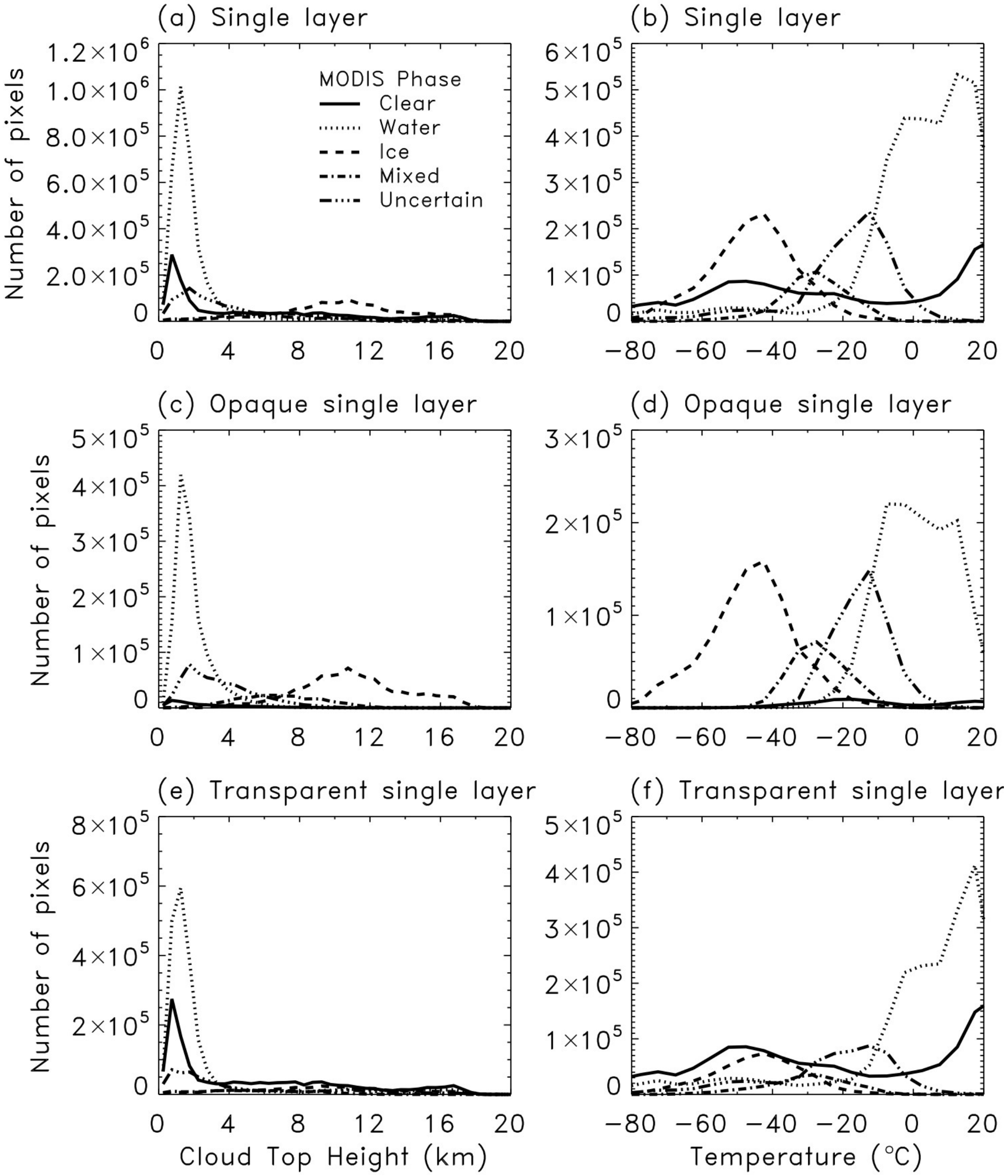

Fig. 3.2 The cloud top height and mid-layer temperature distribution of MODIS IR cloud phase for three layers (i.e. (a) and (b) are for single layers, (c) and (d) are for opaque single layers, and (e) and (f) are for transparent single layers) as detected by CALIPSO from January to June 2008.

The distributions with respect to mid-layer cloud temperature (Fig. 3.2b, d, and f) are even more interesting and support the NK08 hypotheses regarding thin cirrus misclassifications and classification of mid-temperature clouds as mixed or unknown phase. The frequency distributions of the MODIS phase classifications are much broader with respect to temperature than they are with respect to cloud height. Further consideration of the single-layer cloud case in Figure 3.2b indicates that MODIS tends to classify clouds with temperatures below -40°C as ice and those with temperatures above 0°C as water. The MODIS mixed classification is the dominant classification for clouds with temperatures between approximately -28°C and -15°C and classifications for clouds with temperatures around -30°C are split nearly equally between ice, mixed, and unknown MODIS classifications. A sizable fraction of CALIPSO clouds are classified as clear by MODIS for all temperatures, but there are cases in which clouds with temperatures below -40° are classified as either water, mixed or unknown by MODIS. Less than 3% of opaque CALIPSO clouds are classified as clear by MODIS, but more cold transparent clouds are classified as clear than any of the four cloud phases. Additionally, similar numbers of transparent clouds with temperatures below -40°C are classified as water and mixed phase.

In addition to comparing MODIS cloud phase to CALIPSO cloud height, mid-layer temperature, and opacity, we consider the CALIPSO cloud phase retrievals. These comparisons should be viewed with some caution due to the beta status of the CALIPSO phase retrievals. While the CALIPSO retrievals are not assumed to be “truth”, the differences in retrieval techniques illuminate the complexity in inferring cloud thermodynamic phase.

The cloud phase comparisons are shown in a tabular form in Tables 3.1–3.4. In these tables, the columns show MODIS phase classifications, while the rows show CALIPSO phase classifications. Recall that the CALIPSO mixed-uncertain category comprises those CALIPSO layers that were combined because they vertically contiguous, or nearly so, but had different CALIPSO phase classifications. There are three numbers in all interior cells: the top is the number of pixels falling into both MODIS and CALIPSO categories, the middle (in parentheses) is the percentage of pixels with the MODIS classification out of all the pixels in the CALIPSO category, while the bottom is the percentage out of the total number of pixels.

Table 3.1 shows the cloud phase occurrences and co-occurrences for the top layer of all the CALIPSO clouds and the corresponding MODIS retrievals. In Table 3.2, only the single-layer CALIPSO clouds are included. Between January and June 2008, 15% of the clouds in the CALIPSO 5-km product are not detected by MODIS; this fraction increases to 19% when only single-layer clouds are considered. When the top layers of all of the cloud cases are considered, CALIPSO classifies 57% of them as ice. The fraction of ice classifications falls to 37% for single-layer clouds. The percentage of CALIPSO water cloud classifications is 38% in the all-cloud cases, and increases to 58% for single-layer clouds. A small percentage is classified as mixed-uncertain or unknown clouds. Because single-layer cloud scenes are easier to work with, many researchers restrict their studies to single-layer cases. These results show that such a limitation may introduce a water cloud bias.

Table 3.1 CALIPSO top layers with layers separated by less than 200 m combined into a single layer. Columns are MODIS phase classifications while rows are CALIPSO phase classifications. There are three positions in the interior cells. The top position represents the number of pixels falling into both MODIS and CALIPSO categories, the middle position (in parentheses) is the percentage of pixels in the MODIS class out of all pixels in the CALIPSO class, while the bottom position is the percentage out of the total number of pixels.

		MODIS IR phase					
		Clear	Water	Ice	Mixed	Uncertain	Sum
CALIPSO Phase	Water	731,361 (13.0%) 4.9%	3,594,820 (64.0%) 24.3%	123,561 (2.2%) 0.8%	172,649 (3.1%) 1.2%	993,704 (17.7%) 6.7%	5,616,095 37.9%
	Ice	1,353,829 (16.1%) 9.1%	1,460,366 (17.4%) 9.9%	2,917,225 (34.7%) 19.7%	1,137,918 (13.6%) 7.7%	1,527,741 (18.2%) 10.3%	8,397,079 56.7%
	Mixed-uncertain	31,860 (7.8%) 0.2%	101,276 (24.7%) 0.7%	93,737 (22.8%) 0.6%	64,815 (15.8%) 0.4%	118,665 (28.9%) 0.8%	410,353 2.8%
	Unknown	64,221 (16.1%) 0.4%	171,474 (43.1%) 1.2%	67,816 (17.0%) 0.5%	36,719 (9.2%) 0.2%	57,662 (14.5%) 0.4%	397,892 2.7%
	Sum	2,181,271 (14.7%)	5,327,936 (36.0%)	3,202,339 (21.6%)	1,412,101 (9.5%)	2,697,772 (18.2%)	14,821,419

Table 3.2 Same as Table 3.1 except for CALIPSO single layers.

		MODIS IR phase					
		Clear	Water	Ice	Mixed	Uncertain	Sum
CALIPSO Phase	Water	656,082 (14.3%) 8.2%	2,980,392 (65.0%) 37.4%	73,177 (1.6%) 0.9%	115,237 (2.5%) 1.4%	758,467 (16.5%) 9.5%	4,583,355 57.6%
	Ice	760,923 (25.9%) 9.6%	335,196 (11.4%) 4.2%	1,198,250 (40.8%) 15.1%	323,028 (11.0%) 4.1%	317,825 (10.8%) 4.0%	2,935,222 36.9%
	Mixed-uncertain	17,744 (9.5%) 0.2%	57,959 (31.0%) 0.7%	27,874 (14.9%) 0.4%	24,799 (13.3%) 0.3%	58,636 (31.4%) 0.7%	187,012 2.3%
	Unknown	49,916 (19.6%) 0.6%	123,947 (48.7%) 1.6%	26,222 (10.3%) 0.3%	18,624 (7.3%) 0.2%	35,638 (14.0%) 0.4%	254,347 3.2%
	Sum	1,484,665 (18.7%)	3,497,494 (43.9%)	1,325,523 (16.7%)	481,688 (6.1%)	1,170,566 (14.7%)	7,959,936

Of the single-layered clouds detected by CALIPSO, MODIS classifies 44% as water, 17% as ice, and about 21% as either mixed-phase or uncertain (Table 3.2). The fraction of MODIS ice cloud classifications is much smaller than the fraction of CALIPSO ice cloud classifications. While the majority (65%) of single-layer clouds classified as water by CALIPSO are also classified as water by MODIS, only 41% of the single-layer CALIPSO ice clouds are classified as ice by MODIS, and 26% are not detected by MODIS. Only 2% of single-layer CALIPSO clouds are mixed-uncertain, but 45% of them are classified as mixed or uncertain by MODIS.

Figure 3.3 shows the zonal frequencies of the CALIPSO phase retrievals (a) and the MODIS phase retrievals (b) for single-layer clouds detected by CALIPSO. The percentages of single-layer CALIPSO clouds retrieved as water and ice dwarf those retrieved as mixed-uncertain and unknown (6%, total). The zonal distribution of MODIS phase retrievals for single-layer CALIPSO clouds look similar to those for all MODIS clouds, such as those in Fig. 3.2 in NK08. Water clouds dominate the MODIS phase retrievals, except in the high latitudes. In the tropics and mid-latitudes, ice is the next most frequent cloud phase, and the frequency of the mixed and unknown MODIS classification increases poleward of approximate 40°. The frequency of single-layer CALIPSO clouds not detected by MODIS is similar to the frequency of MODIS ice retrievals.

In Figures 3.3c and 3.3d, the zonal distributions of MODIS phase retrievals are separated into those clouds classified as water by CALIPSO (58%), and those classified as ice by CALIPSO (37%). Differences between the phase retrievals for CALIPSO water clouds and MODIS increase poleward of 40°, with mixed being increasingly more likely as the MODIS classification. The number of CALIPSO water clouds that are not detected by MODIS peaks in the tropics. The MODIS phase retrievals for the CALIPSO ice clouds are more complicated, with similar number of clouds being classified as ice by MODIS as the sum of the mixed, unknown, and water classifications for all latitudes. Additionally, the number of CALIPSO ice clouds not detected by MODIS has peaks in both the tropics and in the high latitudes.

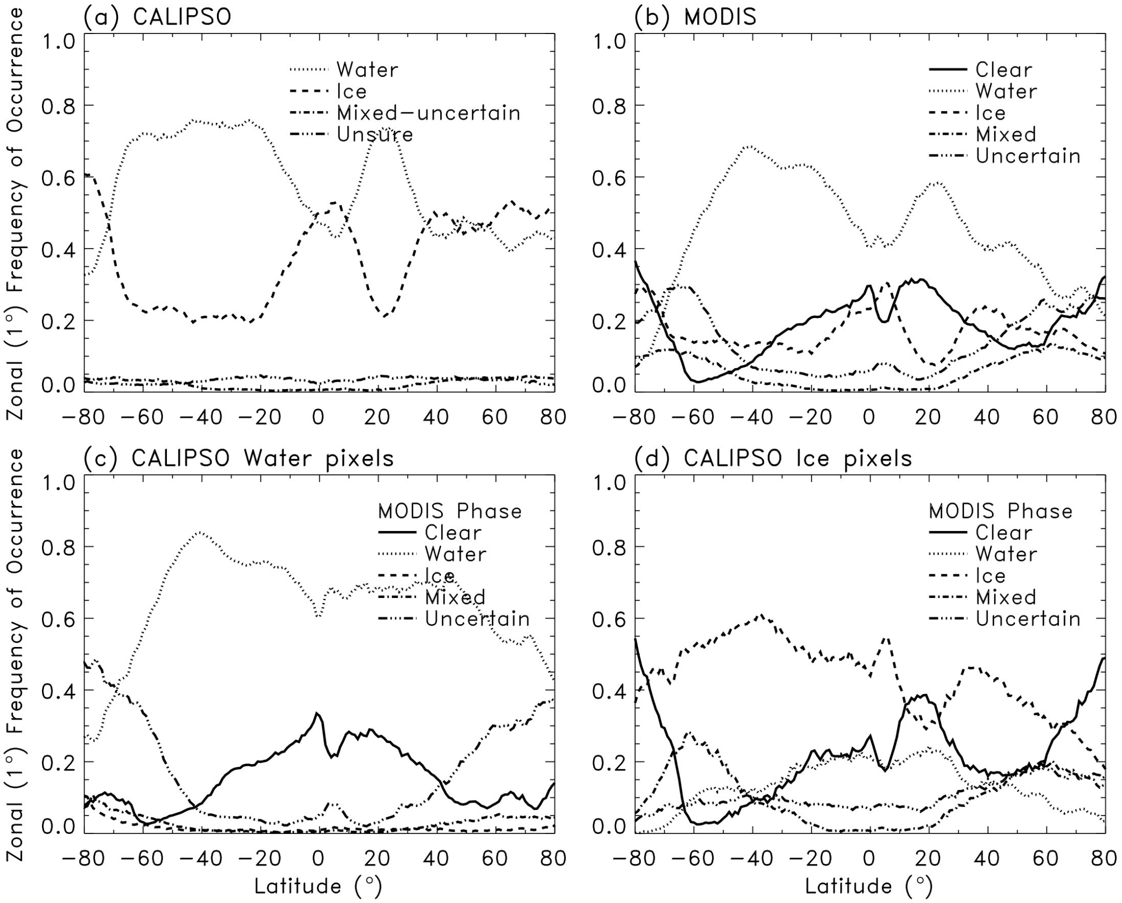

Fig. 3.3 Zonal frequencies of cloud phase are shown for CALIPSO cloud phase in (a), MODIS IR cloud phase for all single layer clouds detected by CALIPSO in (b), all single-layer clouds classified as water by CALIPSO in (c), and (d) all single-layer clouds classified as ice by CALIPSO.

The distribution of MODIS phase retrievals for each retrieved CALIPSO phase is now explored. These comparisons are made with respect to mid-layer cloud temperature for single-layer opaque (Fig. 3.4) and single-layer transparent clouds (Fig. 3.5). Figure 3.4a shows that opaque CALIPSO water clouds have mid-layer cloud temperatures between -40°C and 20°C (our cloud temperature scale is between -80°C and 20°C) and these clouds tend to be classified as either water (the warmer clouds) or uncertain (the cooler clouds) by MODIS. In Figure 3.4b, the colder CALIPSO ice clouds tend to be classified as ice by MODIS, while the warmer ice clouds tend to be classified as mixed.

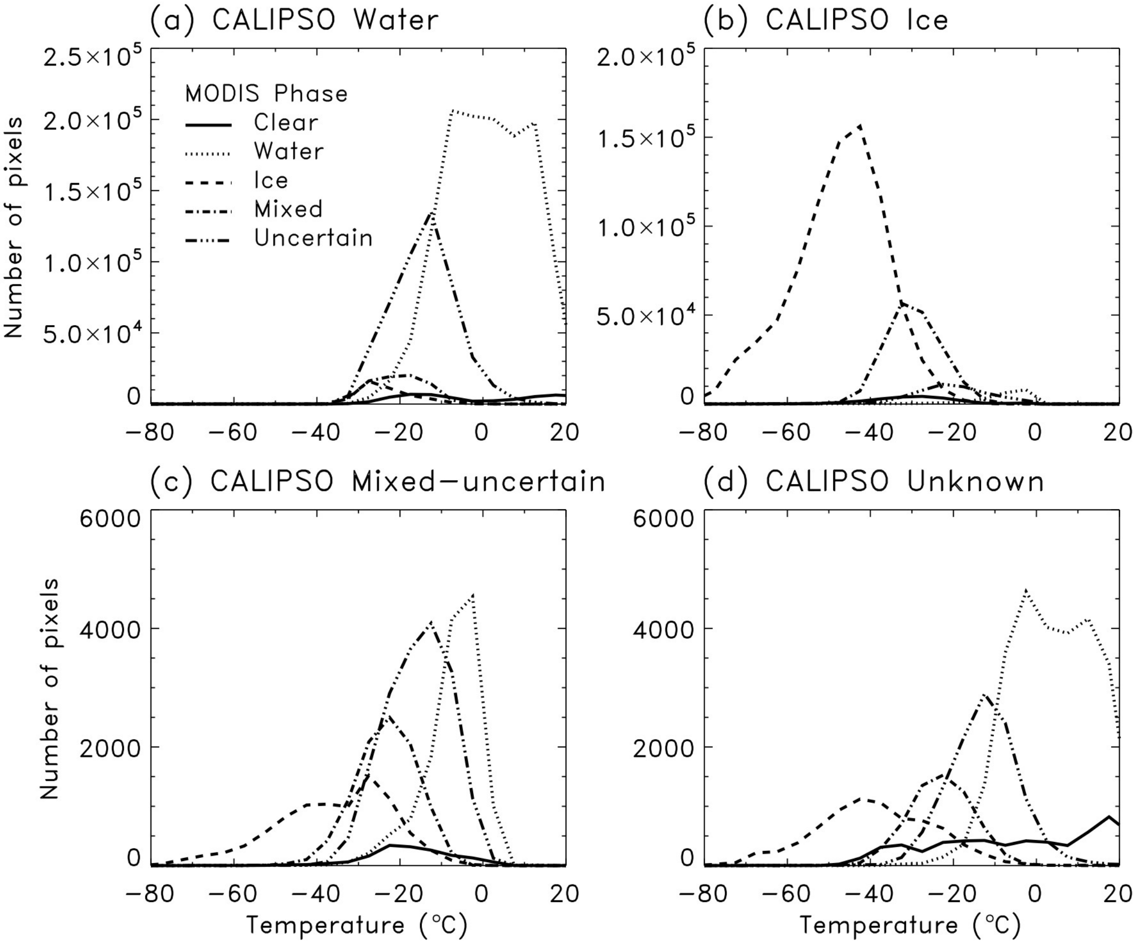

Fig. 3.4 Distributions of MODIS IR phase for opaque single-layer clouds detected by CALIPSO are shown with respect to CALIPSO-retrieved mid-layer cloud temperature for clouds classified by CALIPSO as water (a), ice (b), mixed-uncertain phases (c), and unknown (d).

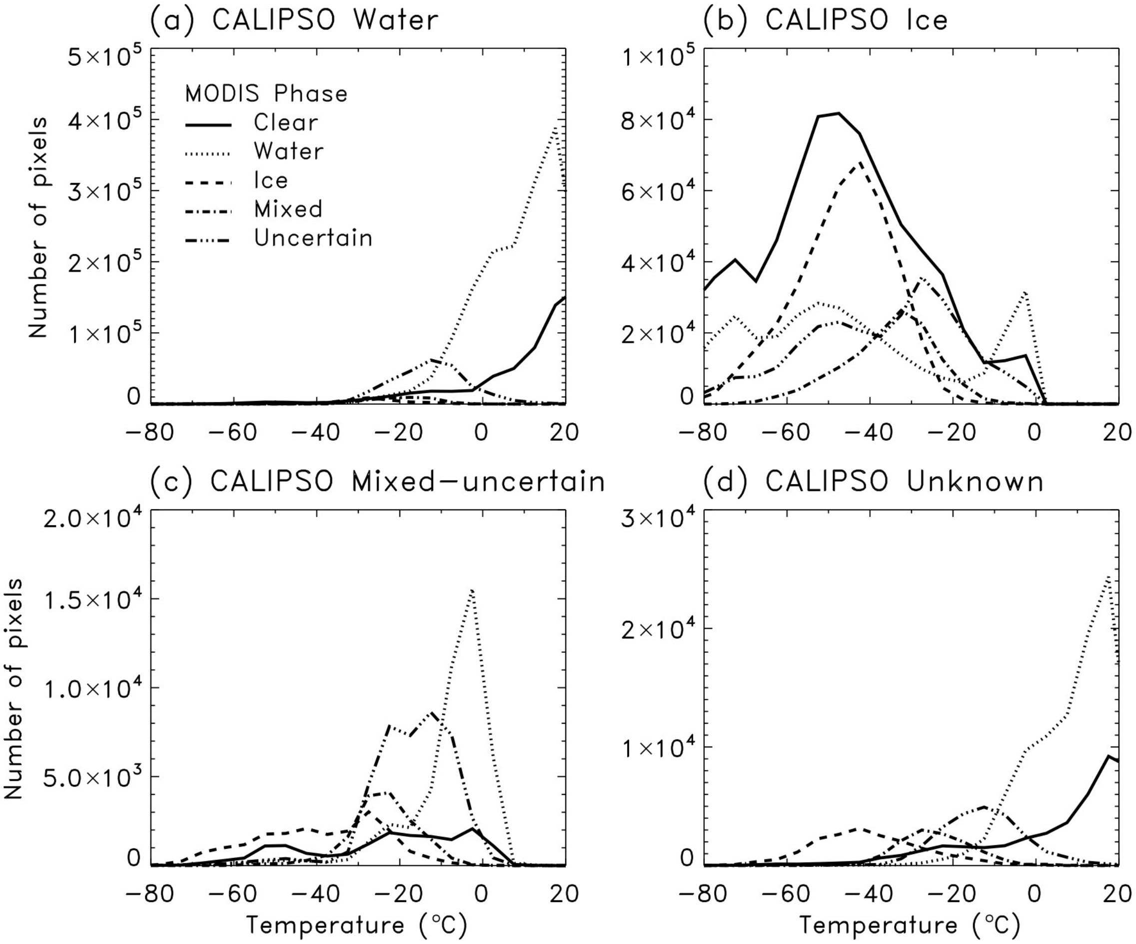

Fig. 3.5 Same as Fig. 3.4, but for transparent single-layer clouds.

The phase co-occurrences for opaque CALIPSO clouds in Table 3.3 show that results for opaque unknown and mixed-uncertain CALIPSO clouds should be interpreted with caution because they make up less than 4% of the category. However, both the opaque mixed-uncertain and unknown CALIPSO clouds span the range of MODIS classifications and while the distributions with respect to mid-layer temperature are broad, the peaks progress from ice, to mixed, to uncertain, to water with increasing temperature.

The transparent cloud distributions in Figure 3.5 and co-occurrences in Table 3.4 differ from the opaque clouds in Figure 3.4 and Table 3.3. There is a larger fraction of clouds not detected by MODIS for each of the CALIPSO classifications and there is a somewhat larger percentage of CALIPSO mixed-uncertain and unknown cases (7%).

Table 3.3 Same as Table 3.1 except for CALIPSO opaque single layers.

		MODIS IR phase					
		Clear	Water	Ice	Mixed	Uncertain	Sum
CALIPSO Phase	Water	50,648	1,293,448	43,135	76,821	492,166	1,956,218
		(2.6%)	(66.1%)	(2.2%)	(3.9%)	(25.2%)	
		1.6%	0.8%	1.4%	2.4%	15.5%	61.8%
	Ice	21,028	21,322	817,596	195,092	48,276	1,103,314
		(1.9%)	(1.9%)	(74.1%)	(17.7%)	(4.4%)	
		0.7%	0.7%	25.8%	6.2%	1.5%	34.8%
	Mixed-uncertain	1,579	13,159	8,837	9,493	17,399	50,467
		(3.1%)	(26.1%)	(17.5%)	(18.8%)	(34.5%)	
		0.0%	0.4%	0.3%	0.3%	0.5%	1.6%
	Unknown	5,797	26,577	7,507	6,020	11,320	57,221
		(10.1%)	(46.4%)	(13.1%)	(10.5%)	(19.8%)	
		0.2%	0.8%	0.2%	0.2%	0.4%	1.8%
	Sum	79,052	1,354,506	877,075	287,426	569,161	3,167,220
		(2.5%)	(42.8%)	(27.7%)	(9.1%)	(18.0%)	

Table 3.4 Same as Table 3.1 except for CALIPSO transparent single layers.

		MODIS IR phase					
		Clear	Water	Ice	Mixed	Uncertain	Sum
CALIPSO Phase	Water	605,434	1,686,944	30,042	38,416	266,301	2,627,137
		(23.0%)	(64.2%)	(1.1%)	(1.5%)	(10.1%)	
		12.6%	35.2%	0.6%	0.8%	5.6%	54.8%
	Ice	739,895	313,874	380,654	127,936	269,549	1,831,908
		(40.4%)	(17.1%)	(20.8%)	(7.0%)	(14.7%)	
		15.4%	6.5%	7.9%	2.7%	5.6%	38.2%
	Mixed-uncertain	16,165	44,800	19,037	15,306	41,237	136,545
		(11.8%)	(32.8%)	(13.9%)	(11.2%)	(30.2%)	
		0.3%	0.9%	0.4%	0.3%	0.9%	2.8%
	Unknown	44,119	97,370	18,715	12,604	24,318	197,126
		(22.4%)	(49.4%)	(9.5%)	(6.4%)	(12.3%)	
		0.9%	2.0%	0.4%	0.3%	0.5%	4.1%
	Sum	1,405,613	2,142,988	448,448	194,262	601,405	4,792,716
		(29.3%)	(44.7%)	(9.4%)	(4.1%)	(12.5%)	

The transparent CALIPSO ice clouds span the gamut of MODIS phase classifications, with a noticeable number of clouds with temperatures less than -40° being classified as water by MODIS, supporting the NK08 hypothesis of under-classification of thin cirrus clouds as ice by MODIS. While both the transparent and opaque CALIPSO mixed-uncertain classifications show large percentages of MODIS mixed and uncertain cases, we hesitate to claim that this supports the interpretation of the MODIS mixed class as signifying mixed-phase clouds for two reasons. The first is relationships between mid-layer cloud temperature and retrieved MODIS phase may be stronger than those between CALIPSO cloud phase and MODIS cloud phase. The second reason is that it is uncertain how well either the MODIS mixed-phase category or our CALIPSO mixed-uncertain class (combining two layers of different CALIPSO phases with little or no vertical separation) sample the full regime of true mixed-phase clouds.

3.5 Summary and Conclusions

In this study, CALIPSO cloud products are compared to the MODIS IR phase retrievals for the 6 months from January 2008 - June 2008. The MODIS IR phase categories are water, ice, mixed, and unknown, although the ability of the algorithm to classify true mixed-phase cloud as mixed is not well known. CALIPSO cloud top height, mid-layer cloud temperature, cloud opacity or transparency, as well as CALIPSO cloud phase retrievals, are used in the comparison. More than 14 million cloudy comparisons are made, but we focus on the 8 million cases described as containing only single-layer clouds. One caveat, that affects not just our results but those of all researchers who simplify multi-instrument cloud comparisons by focusing on CALIPSO single-layer clouds, is that the CALIPSO cloud phase retrievals show that a focus on single-layer clouds may introduce a bias towards water clouds.

The data show that clouds classified by CALIPSO as being single-layered with a top below 4 km are typically classified as water by the MODIS algorithm, with some classified as clear (not detected as clouds) or unknown. Opaque clouds (those without

CALIPSO ground returns) with tops above 8 km tend to be classify by MODIS as ice, with some unknown, while transparent high cloud classification span the range of MODIS classes. Opaque clouds with tops between 4 and 8 km are about as likely to be classified as mixed or uncertain, with slightly lower likelihood of being classified as water or ice. The MODIS phase distributions with respect to CALIPSO mid-layer cloud temperature tend to be broad and overlapping, with well-defined peaks for opaque clouds. The ice cloud frequency peaks around -43°C, mixed at -27°C, unknown at -15°, and water above 0°C. The frequency distributions are even broader for transparent clouds, showing that MODIS has detection issues with optically thin clouds, as seen by Ackerman et al. (2008), as well as difficulty in assigning a phase to them.

These results support several hypotheses presented by Nasiri and Kahn (2008, NK08) in their primarily radiative transfer modeling study. Specifically, the MODIS IR phase algorithm may tend to 1) classify thin cirrus clouds as water clouds, 2) classify thin cirrus clouds as mixed or unknown, and 3) classify midlevel and/or mid-temperature clouds as mixed or unknown phase. The comparisons to the CALIPSO mid-layer cloud temperature product demonstrates the usefulness of the concept of "mid-temperature" to describe temperatures at which water, ice, or mixed-phase clouds could occur. An interesting observation is that while the MODIS IR phase algorithm makes a priori assumptions about relationships between cloud temperature and cloud phase, the assumptions are executed with respect to brightness temperature, rather than cloud temperature. For the CALIPSO opaque cloud cases, where brightness temperature is a decent proxy for cloud temperature, this assumption holds well, as is seen in the MODIS phase vs. mid-layer cloud temperature distributions discussed above. The NK08 results demonstrated that there may not be enough spectral phase information in the 8.5 and 11 µm MODIS bands to determine the phase of many mid-temperature clouds and that, therefore, the MODIS unknown phase classification is most appropriate for these clouds. Our current results show that MODIS is classifying the majority of opaque mid-temperature clouds as unknown or mixed phase. However, the MODIS-assumed thermodynamic phase – cloud temperature relationships breaks down for the transparent cloud cases.

4. DETECTION OF OPTICALLY THIN MINERAL DUST AEROSOL LAYERS USING MODIS

4.1 Introduction

Mineral dust aerosols, one of the major atmospheric aerosol groups, are important in climate studies (Sokolik and Toon, 1996; Jaffe et al., 1999; Husar et al., 2001; and Prospero et al., 2002) through several ways. Mineral dust affects the Earth radiation budgets directly through absorbing and reflecting solar radiation and indirectly through regulating the formation and maintenance of clouds. Recent studies (Dunion and Velden, 2004; and Evan et al., 2006a) showed the possible impact of the dust storm in the formation and evolution of hurricane. Despite the climatic importance of dust, its effect on the climate via direct or indirect radiative forcing still has large uncertainties in climate change studies (IPCC, 2007; and Zhu et al., 2007). Additionally, the amount of mineral dust aerosol entering the atmosphere is also uncertain with emission estimates from modeling studies ranging from 1000 ~ 2150 Tg per year (Zender et al., 2004). These uncertainties primarily come from insufficient measurements on global scale and uncertainties of retrievals.

As mentioned in section 1, several algorithms have been proposed to discriminate dust aerosols from clouds and clear scenes in a wide range of wavelengths from ultra-violet (UV) to infrared (IR) with various passive sensors. Most of these algorithms have focused on optically thick dust plumes, which are transported from desert areas. Due to the lack of vertical sensitivity from passive remote sensing, it can be difficult to separate thin mineral dust from cloud and clear scenes. Again, the CALIPSO satellite can provide more precise vertical information about and greater sensitivity to small amount of dust, which makes it an excellent instrument to evaluate existing detection algorithms and help develop new ones.

The objectives of this section are to present an evaluation of the existing three dust detection methods, to describe a new algorithm for dust detection over ocean for the MODIS, and then to discuss validation and case study results for our new technique by using CALIPSO lidar observation. Therefore, the remainder of this paper is as follows: Section 4.2 presents the MODIS and CALIPSO data used in this study. In section 4.3, we show the result from the evaluation of the existing dust detection methods. The MODIS radiative signatures of the thin dust layers are discussed in section 4.4. Section 4.5 describes a new multi-spectral algorithm based on discriminant analysis. The case study and evaluation of our new algorithm are shown in section 4.6. Finally, the summary and conclusions are given in section 4.7.

4.2 Data

In this study, several mineral dust detection approaches using VIS/IR bands with passive sensors are evaluated using active remote sensing observations. Dust detection approaches applied to MODIS observations from the Aqua satellite in the “A-train” constellation are compared with CALIPSO lidar scene classification. The CALIPSO lidar products are used as an independent source of mineral dust information for product evaluation and as reference for training a new dust detection algorithm. This study uses one year of 2008 daytime collocated MODIS and CALIPSO data over ocean.

4.2.1 MODIS

The MODIS is a passive optical multispectral sensor that measures visible and infrared radiation in 36 spectral bands ranging from 0.4 μm to 14.4 μm (Kaufman et al., 2000). MODIS is presently mounted on two satellite platforms: Terra and Aqua. Both Terra and Aqua satellites are operated at a sun-synchronous orbit with the altitude of 705 km, observing the earth at three different nadir spatial resolutions: 250 m, 500 m, and l000 m. Major datasets used in this study include the Level 1B (L1B) MODIS measurements at 1-km resolution from Aqua satellite. Note that the reflectances in solar bands are corrected with solar zenith angle, and the brightness temperatures are converted from radiance. In discussion for comparison with detection results, the aerosol optical thickness (AOT) at a wavelength of 0.55 μm from the Level 2 aerosol product (MYD04) is also used.

4.2.2 CALIPSO cloud and aerosol layer product

The CALIPSO cloud and aerosol products used in this study are the CALIPSO 5-km Level-2 (Ver. 3.01) layer data. The CALIPSO Level-2 layer products contain information on up to 8 aerosol layers and 10 cloud layers within each 5-km retrieval footprint. To describe the CALIPSO cloud/dust categories, we use the number of layers provided in CALIPSO cloud and aerosol retrievals as well as aerosol type classification.

The number of feature layers (i.e. cloud or aerosol layers) is calculated by the Selective Iterated Boundary Location (SIBYL) algorithm (Vaughan et al., 2009) using profiles of attenuated backscatter coefficients. After detecting the feature boundaries, the Scene Classification Algorithm (SCA) discriminates between cloud and aerosol (Liu et al., 2009) and then determines the cloud phases (Hu et al., 2009) and the sub-types of aerosol layers (Omar et al., 2009). The CALIPSO aerosol sub-typing algorithm uses the integrated attenuated backscatter at 532 nm and the particulate depolarization ratio with an aid of surface types and layer elevation to identify aerosol type from among one of the six types (i.e. Clean Marine, Clean continental, Polluted continental, Dust, Polluted dust, Smoke (biomass burning)). For example, aerosol layers having particulate depolarization ratio greater than 0.2 are classified as dust except for polar regions. More detailed descriptions of the algorithm are given in Omar et al. (2009).

In this study, we classify the CALIPSO retrievals into four categories: clear, cloud, dust, and other. We consider the pixel to be clear if no layers are found in either the aerosol or cloud product. If only cloud layers are present, then we classify the pixel as cloud. If only dust type aerosol layers are found in the whole column, we consider it to be a dust pixel. If the pixel does not fit into either of the above three categories (clear, cloud, dust), we classify the pixel as “other”. The other category includes scenes containing both cloud and dust, cloud and non-dust aerosols, or just non-dust aerosols.

4.3 Initial Evaluation of Existing Dust Detection Methods

We evaluate three existing dust detection techniques by applying them to MODIS daytime radiances/reflectances over the ocean and comparing the results with CALIPSO's operational aerosol and cloud product. Specifically, we compare: (1) simple brightness temperature difference (BTD) threshold techniques, (2) Roskovensky and Liou's (2005) D-parameter algorithm and (3) Zhao et al.'s (2010) multi-channel imager (MCI) algorithm. We start with the simplest of three techniques: utilizing infrared brightness temperature differences (BTDs) to detect dust. Shenk and Curran (1974) demonstrated the utility of the 10.5–12.5 μm BTD from the Temperature Humidity Infrared Radiometers (THIR) on board the Nimbus 4 satellite for dust storm detection over land. BTDs are used to infer the temperature differences between the surface and cooler mineral aerosol layer (Darmenov and Sokolik, 2005). Ackerman (1997) used simulations of the BTD between the 8.5 and 11 μm ($BTD_{8.5\text{-}11\mu m}$) and the BTD between 11 and 12 μm ($BTD_{11\text{-}12\mu m}$) to investigate the possibility of detecting soil-derived aerosols. His research showed, through observation and modeling studies, that $BTD_{11\text{-}12\mu m}$ of dust is smaller than that of clouds. In this study, we test the use of three different thresholds (0, 0.5, and 1 K) in $BTD_{11\text{-}12\mu m}$ in detecting dusty pixels as classified by CALIPSO.

For the D-parameter method, Roskovensky and Liou (2005) expanded upon the simple $BTD_{11\text{-}12\mu m}$ test by adding a reflectance ratio. According to measurement and modeling studies (Patterson et al., 1977; and Sokolik and Toon, 1999), mineral dust aerosol displays a decreasing imaginary part of the complex index of refraction with wavelength in visible spectral range, while clouds scatter more uniformly over this spectral range. For example, Miller (2003) uses the reflectance ratio between visible and near-infrared channels in MODIS data to enhance dust regions over dark backgrounds such as ocean water (apart from areas of sun glint, shallow, or sediment/organic-laden waters). In this study, we evaluate the D-parameter, which is defined by Roskovensky and Liou (2005) as follows,

$$D = \exp\left\{-\left[rr \times a + (\mathrm{BTD}_{11\text{-}12\mu\mathrm{m}} - b)\right]\right\}, \tag{4.1}$$

where rr represents the 0.54 μm/0.86 μm reflectance ratio, a is its scaling factor (0.8) and b is an offset to the $\mathrm{BTD}_{11\text{-}12\mu\mathrm{m}}$ (2.0), respectively. Pixels with D values greater than 1 are classified as dust.

The third algorithm we test is multi-channel imager (MCI) algorithm developed by Zhao et al. (2010). This algorithm is designed to operationally monitor the outbreak and dispersion of dust storms and smoke plumes over both land and ocean for multi-channel radiometric imagers such as EOS/MODIS, JPSS/VIIRS, and GOES-R/ABI. In this study, however, we focus on the dust detection over ocean. As the MCI algorithm's name implies, several spectral tests involving SW reflectances and IR brightness temperatures are used. The algorithm introduces an additional level of sophistication through application of a spatial variability test using the standard deviation of 0.86-µm reflectances. The purpose of the spatial variability test is to exploit the tendency of dust to be more uniformly distributed than cloud (Martins et al., 2002). In addition, since dust over ocean is less reflective than clouds, a reflectance test ($R_{0.47\mu\mathrm{m}} \leq 0.3$) is added to BTD tests ($\mathrm{BTD}_{3.9\text{-}11\mu\mathrm{m}}$, $\mathrm{BTD}_{11\text{-}12\mu\mathrm{m}}$) and reflectance ratio tests ($R_{0.47\mu\mathrm{m}}/R_{0.64\mu\mathrm{m}}$, modified version of ratio of $R_{0.86\mu m}$ and $R_{0.64\mu m}$). In their initial evaluation, the algorithm can capture heavy dust and smoke plumes over land and ocean, however it has difficulty in detecting thinner or dispersed dust and smoke plumes due to the relatively weak aerosol signal.

We compare the dust detection methods to a MODIS scene off the northwest coast of Africa from April 2, 2008 at 1450 UTC in Fig. 4.1. Panel (a) shows a MODIS true color view of the scene along with the CALIPSO track labeled with the CALIPSO scene classification. Panel (b) shows the MODIS retrieval of aerosol optical thickness (AOT) over ocean. The black strip down the length of the image is where sunglint prevented retrieval. Dust plumes can be found near the coastline of Africa in right and lower side of Fig. 4.1a and b. Thin dust layers are detected by CALIPSO along the track (lower part of center line in Fig. 4.1a), even though it is difficult to identify in MODIS RGB image due to the dust being optically thin (Fig. 4.1b). The results of three different BTD11-12μm thresholds are shown in panels (c–e). The differences between these show the detection sensitivity to small threshold changes. As the threshold increases, detected dusty area increases. However, cloudy areas are also classified as dust with a high threshold. The D-parameter technique looks effective in identifying dust regions with both thin and thick dust layers. The MCI algorithm detects the relatively thick dust near the coastline of Africa. These results demonstrate the difficulty of optically thin dust detection in scenes with clouds.

While Figure 4.1 compares dust detection for one MODIS granule, the algoirthms have also been applied to a year (2008) of co-located ocean-only MODIS and

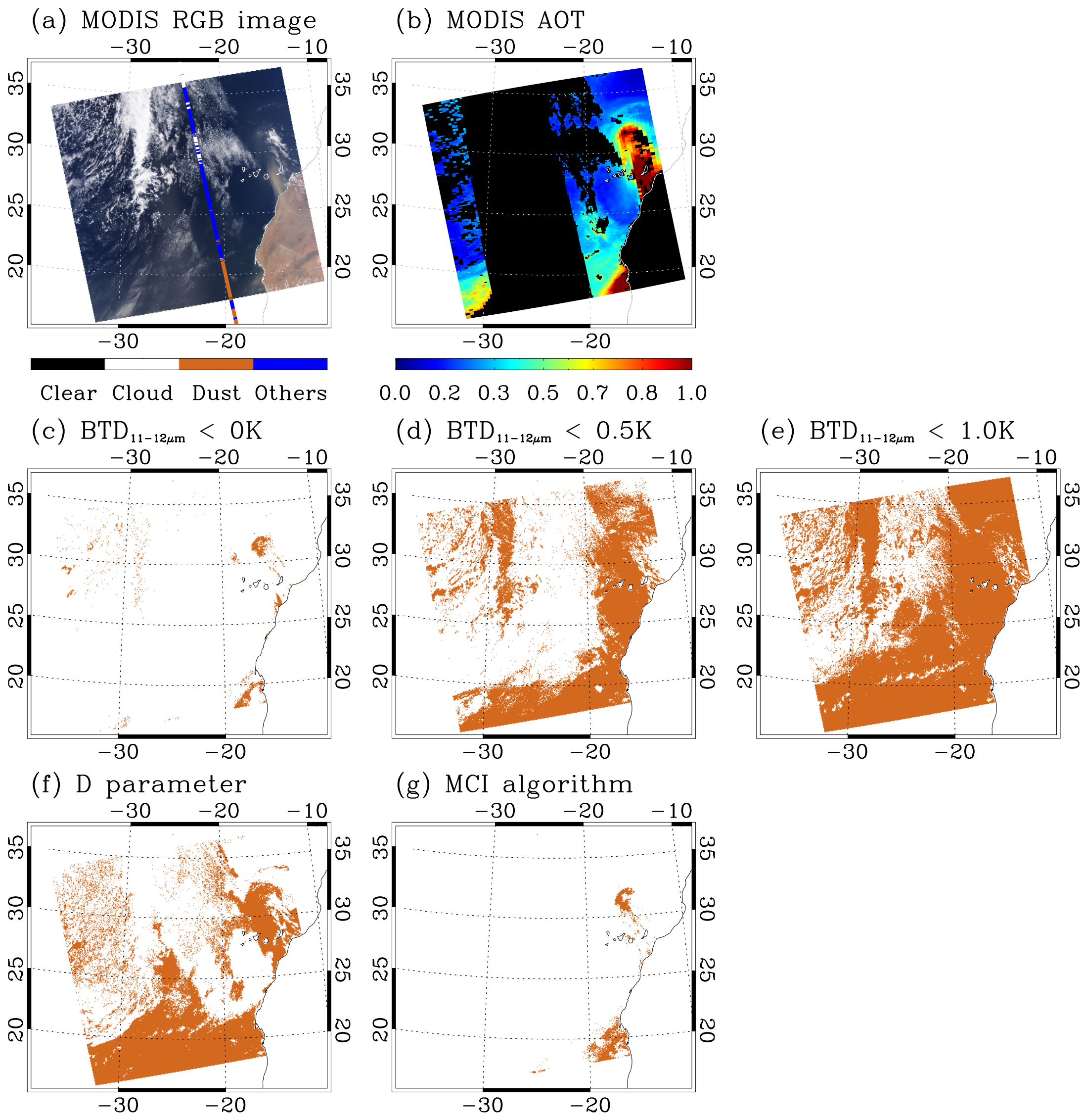

Fig. 4.1 (a) MODIS RGB image on April 2, 2008 (1450 UTC) along with the CALIPSO track (the center line with colors), (b) MODIS aerosol optical thickness (AOT), and dust detection results (c, d, and e) for the $BTD_{11\text{-}12\mu m}$ threshold tests, (f) for the D parameter methods, and (g) for the MCI algorithm. Pixels classified as dust by each technique are shown in orange.

Table 4.1 Comparisons between MODIS dust detection techniques and co-located CALIPSO scene classification during 2008 daytime over ocean. Rows are MODIS dust detection techniques, including three different BTD thresholds, while columns are CALIPSO cloud/dust classifications. The percentages in the interior cells represent the percentage of dust pixels by MODIS dust detection techniques out of the total number of the each CALIPSO classes. Note that CALIPSO dust categories are separated into thin and thick layer by a CALIPSO optical thickness (τ) threshold of 1.

	CALIPSO category				
	Clear	Cloud	Dust		Others
			$\tau < 1$	$\tau \geq 1$	
$BTD_{11\text{-}12\mu m}$ < 0K	4.5%	3.8%	1.2%	8.2%	0.9%
$BTD_{11\text{-}12\mu m}$ < 0.5K	31.5%	40.6%	23.1%	38.6%	11.1%
$BTD_{11\text{-}12\mu m}$ < 1K	67.3%	68.0%	66.3%	72.0%	41.8%
D Parameter	20.5%	36.0%	14.8%	58.9%	14.9%
MCI	0.09%	0.01%	1.6%	9.9%	0.03%
Total	427,252	6,091,514	70,985	4,003	4,821,017

CALIPSO observations. Table 4.1 compares the three $\mathrm{BTD}_{11\text{-}12\mu m}$ thresholds, D-parameter, and MCI with CALIPSO's scene classification, as described in section 4.2.2.

The percentages show the fraction of pixels in each scene category that would be classified as dust by the algorithm. Therefore, the clear and cloudy percentages should be viewed as false positives, while the others percentage is harder to interpret because the scene type is mixed. Note that while ~75,000 co-located pixels are classified as dust by CALIPSO, these make up less than 1% of our ~11 million pixel data set. To further focus on the detection of optically thin dust, we use the CALIPSO dust optical depth threshold of 1 is used to separate thin ($\tau < 1$) and relatively thick ($\tau \geq 1$) dust.

Overall, all these dust detection methods are better at finding thick ($\tau \geq 1$) dust than thin ($\tau < 1$), however these techniques do not consistently separate dusty areas from areas that are clear, cloudy or others. In general, an algorithm that correctly classifies a large percentage of the dust scenes, will incorrectly classify a larger fraction of clear and cloudy scenes as dust. For example, the 1-K BTD threshold test is most successful at finding thick ($\tau \geq 1$) dust (72.0% of scenes) and thin ($\tau < 1$) dust (66.3% of scenes), however it incorrectly classifies as larger number of clear (67.3%) and cloudy (68.0%) scenes as dust than thin dust scenes. In the $\mathrm{BTD}_{11\text{-}12\mu m}$ threshold tests, small threshold changes have large impacts on detection fraction. The D-parameter technique classifies a large percentage of clear and cloudy scenes as dusty. For the MCI algorithm, the percentage of dusty area is higher than that of clear or cloudy region, but it is still small (1.6% for thin dust and 9.9% for thick dust). These imager techniques may have difficulties in separating thin dust layers from both clear and cloudy pixels. Dust scenes may be difficult to distinguish from dust scenes because of similarities between the spectral reflectance and radiance of optically thin dust layers and clear scenes. Dust may be difficult to distinguish from cloud due to the global use of simple fixed thresholds. While not necessarily effective for the sort of optically thin dust scenes at which CALIPSO excels in detection, these techniques may be effective for detection of highly concentrated or optically thick dust.

4.4 MODIS Radiative Signatures of the Thin Dust Layers

As shown in the previous subsection, detecting the optically thin dust that can be observed by CALIPSO can be difficult for imager-based algorithms. In this subsection, we investigate several dust parameters with the goal of developing a MODIS algorithm to thin dust layers. Specifically, six MODIS parameters are investigated, including brightness temperature differences, and standard deviation and ratios of reflectance, for inclusion in a training data set for a the new algorithm.

As mentioned before, window channel BTDs provide some information about dust scenes (e.g. Ackerman, 1997). In this study, we consider the BTDs between 11 μm and 12 μm and between 8.5 μm and 11 μm. Since aerosol layers have a more homogeneous structure than clouds (Martins et al., 2002), the standard deviation of reflectance at 0.55 μm (STD[$R_{0.55\mu m}$]) will be used to help to separate dust aerosols from clouds. Another parameter used in this study is the normalized difference vegetation index (NDVI). Originally, the NDVI was used for the identification of vegetated areas (Rouse et al., 1973). However, it can also be used in mineral dust detection due to the different reflectances of dust in the red and near-infrared spectral regions (Evan et al., 2006b). The NDVI is defined as the modified ratio of reflectances at 0.64 μm and 0.86 μm,

$$\mathrm{NDVI} = \frac{R_{0.86\mu m} - R_{0.64\mu m}}{R_{0.86\mu m} + R_{0.64\mu m}}. \tag{4.2}$$

Qu et al. (2006) proposed a normalized difference dust index (NDDI) for distinguishing mineral dust from the clouds due to the spectral characteristic of sand at 2.13 μm and 0.47 μm. The NDDI is analyzed in this subsection, which is defined as the modified ratio of reflectances at these wavelengths,

$$\mathrm{NDDI} = \frac{R_{2.13\mu m} - R_{0.47\mu m}}{R_{2.13\mu m} + R_{0.47\mu m}}. \tag{4.3}$$

The last parameter is the simple ratio of 0.47 μm (blue) and 0.645 μm (red) reflectances ($R_{0.47\mu m}/R_{0.64\mu m}$). As mentioned in the previous section, mineral dust absorptivity increases with decreasing visible wavelength, while clouds scatter more uniformly over the visible wavelengths. So, this ratio will help to separate dust from cloud.

We test the usefulness of these MODIS parameters for dust discrimination using one year (2008) of collocated daytime MODIS and CALIPSO data. In this study, only ocean surface away from ice cover and sun-glint regions are considered. Fig. 4.2 shows the distribution of MODIS NDVI (Eqn. 4.2) and standard deviation of reflectance at 0.55 μm (MODIS band 4) of 3 by 3 pixel blocks (STD3[$R_{0.55\mu m}$]) for each of the CALIPSO clear, cloud and dust classifications. The MODIS NDVI of CALIPSO cloudy pixels is concentrated around zero value and the standard deviation of reflectance of cloud is

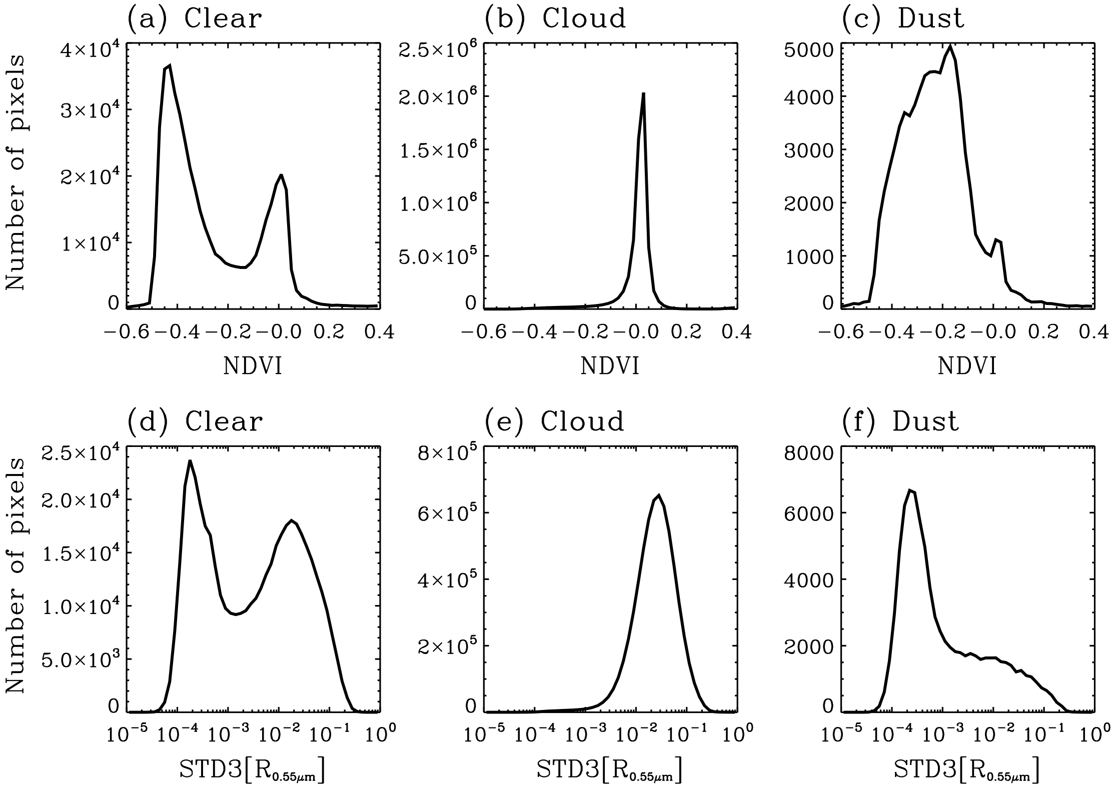

Fig. 4.2 Distribution of MODIS NDVI (a~c) and 3 by 3 pixel standard deviation of MODIS $R_{0.55\mu m}$ (d~f) for each of the CALIPSO clear, cloud, and dust categories (left panel: clear, middle panel: cloud, and right panel: dust pixels) during 2008.

around 10^{-2}, while the NDVI distribution is broader and the reflectivity variability lower for dust. This figure verifies the result of Martins et al. (2002) that mineral dust reflectivity is more uniform than clouds. Therefore, these parameters will be useful in discriminating dust from cloud. However, the clear pixels have two peaks in both the NDVI and STD3[$R_{0.55\mu m}$]. In Fig. 4.2a, one peak of NDVI is near zero value, and another one is around -0.4. This feature is also found in the standard deviation of MODIS band 4 as shown in Fig. 4.2d. This may be due to the difference of data resolutions between MODIS and CALIPSO. In this analysis, we collocated the CALIPSO 5-km cloud and aerosol layer products with 1-km MODIS resolution. Therefore, CALIPSO classification may classify a fraction of clouds having smaller horizontal extension than 5 km as clear.

We have also seen a few examples of the CALIPSO 5 km cloud layer product failing to classify scenes containing small marine boundary layer cumulus as cloudy. For example, Fig. 4.3 shows the MODIS cloudy pixels corresponding CALIPSO clear sky scenes. The CALIPSO retrieval classifies the region in the red circle in Fig. 4.3b as clear, although the MODIS image implies that there is marine boundary layer cumulus cloud. Because it appears that, at the MODIS scale, there is some cloud contamination in CALIPSO's clear category and it is necessary to try to separate the two peaks before we can use the classifications as a training data set.

In this study, we have applied an additional screening based on the MODIS $R_{0.64\mu m}$ (R1 in some figures) to eliminate cloud contamination in CALIPSO clear classification, because this visible wavelength is highly sensitive to cloud optical thickness. We assume that CALIPSO clear scenes with MODIS $R_{0.64\mu m}<0.05$ are truly clear, and the CALIPSO clear pixels with MODIS $R_{0.64\mu m}\geq 0.05$ have some cloud contamination.

Based on this modified CALIPSO scene classification, the six parameters mentioned above are analyzed as follows. First, the distributions of standard deviation of $R_{0.55\mu m}$ for six latitude bands (Lat. band 1: 90°~60°; Lat. band 2: 60°~30°; Lat. band 3: 30°~0°; Lat. band 4: 0°~-30°; Lat. band 5: -30°~-60°; and Lat. band 6: -60°~-90°,

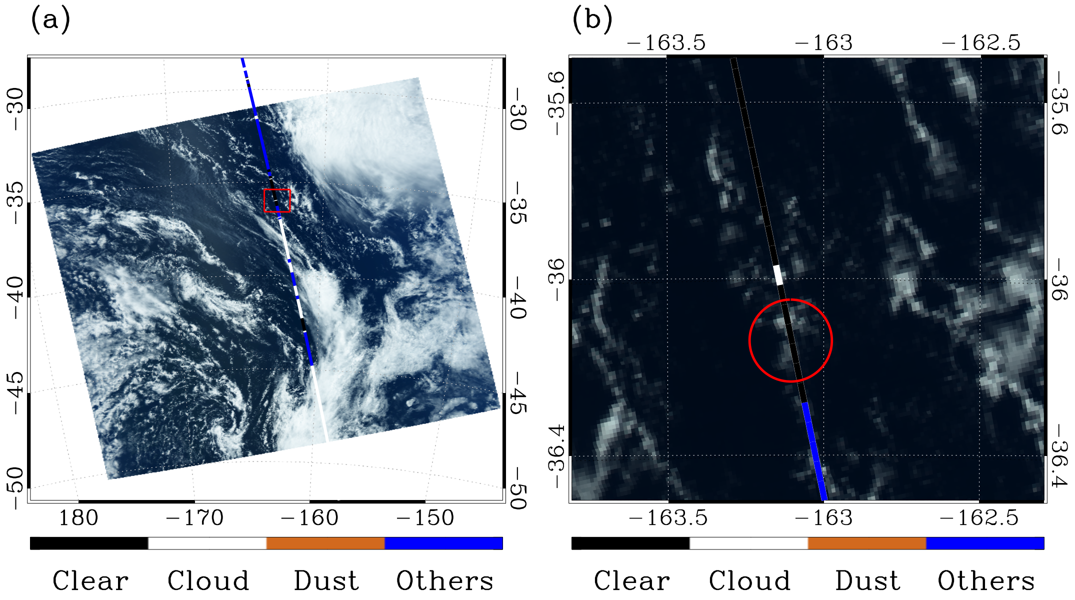

Fig. 4.3 (a) MODIS RGB image from January 1, 2008 (0055 UTC) along with CALIPSO flight track and (b) the RGB image of the red box area indicated in (a). The colorbar shows the CALIPSO scene classification along the CALIPSO track. Note that the CALIPSO retrieval classifies the region in the red circle in (b) as clear, although the MODIS image implies the presence of cloud.

respectively), and four regimes of CALIPSO optical thickness retrievals are shown in Fig. 4.4. The first row shows CALIPSO clear scenes with MODIS $R_{0.64\mu m}<0.05$, which we consider to be clear. The second row shows CALIPSO clear scenes with MODIS $R_{0.64\mu m}\geq0.05$ which we consider to be cloud contaminated. It will require additional screening to separate the two STD3[$R_{0.55\mu m}$] peaks in CALIPSO clear classification. The standard deviations of clear ($R_{0.64\mu m}<0.05$) and dust pixels are much lower than those of clouds and show little latitudinal dependence. As expected, the spatial variability of

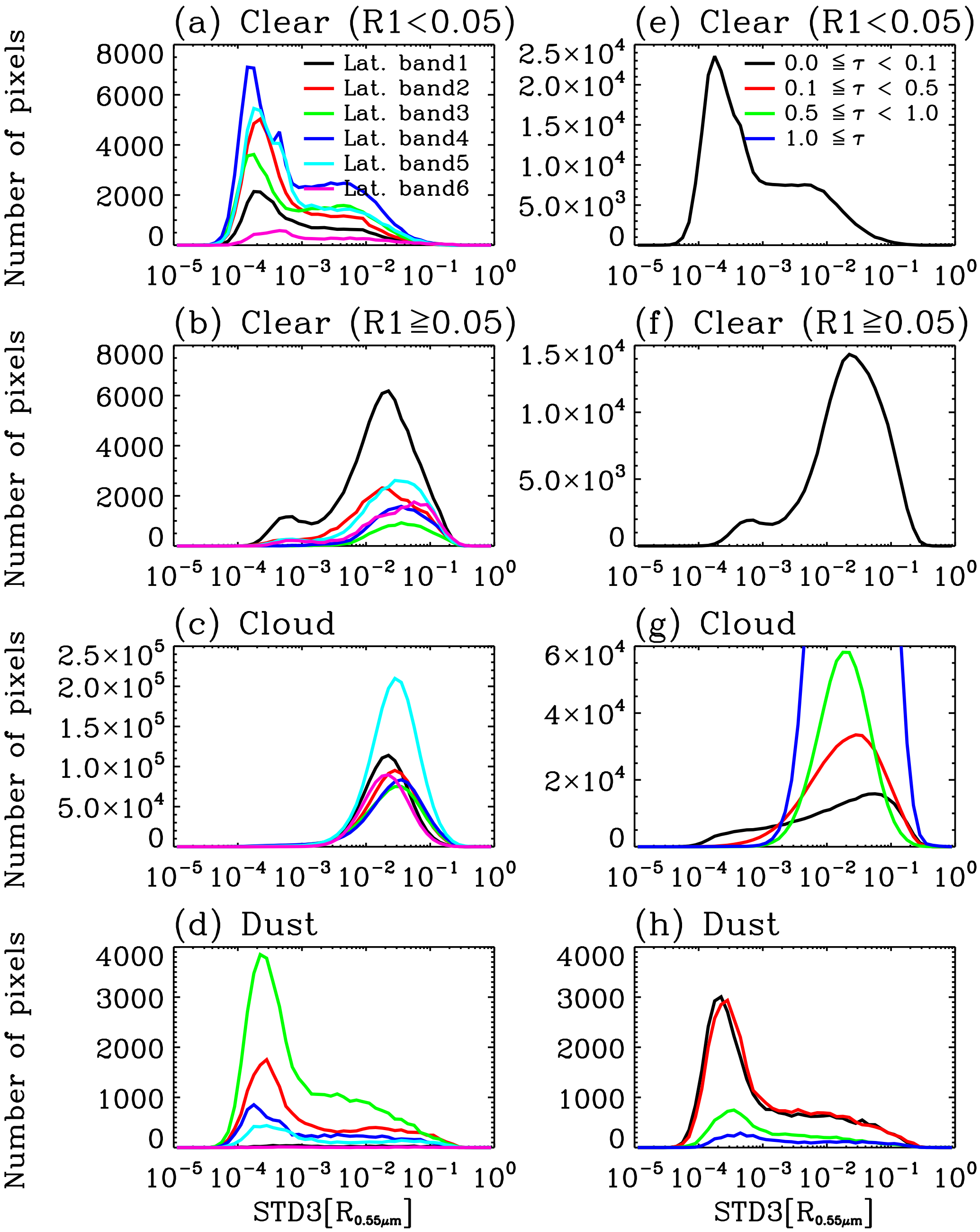

Fig. 4.4 Distribution of 3 by 3 pixel standard deviation of MODIS $R_{0.55\mu m}$ for the modified CALIPSO categories (first row: clear ($R_{0.64\mu m}$<0.05), second row: clear ($R_{0.64\mu m}$≥0.05), third row: cloud, and bottom row: dust) during 2008 with respect to different latitude bands (left column), and CALIPSO optical thickness (right column).

cloud-contaminated clear category looks similar to that clouds expect for small peak around 10^{-3}. To build our training data set, it will be important to have a distinct classification for our clear category, therefore the small peak in the cloud-contaminated clear class is less important. We also see little dependence on optical thickness for either clouds or dust pixels. Overall, STD3[$R_{0.55\mu m}$] should be useful to discriminate dust from cloud.

Figure 4.5 shows the distribution of MODIS NDVI for the modified CALIPSO scene classification. The CALIPSO cloud category shows a very narrow peak around 0 because of flat spectral sensitivity of cloud at 0.64 μm and 0.86 μm, while the clear ($R_{0.64\mu m} < 0.05$) and the dust categories have wider ranges of NDVI values near -0.4 (clear) and -0.2 (dust), respectively. As we expected, the NDVI of clear ($R_{0.64\mu m} \geq 0.05$) category looks similar to that of clouds with little peak around -0.3. The NDVI of the clear ($R_{0.64\mu m} < 0.05$) and cloud classes show less latitudinal dependence than that of the dust. For the dust, the MODIS NDVI of the latitude band from 0 to 30° (green in Fig. 4.5d) shows higher frequency than other latitude bands and has a somewhat higher NDVI values, which corresponds to an optically thick layer. This is because most large desert areas, including the Saharan desert, are located within this latitude band. The NDVI of dust increases with optical thickness. So, NDVI will be useful to separate optically thin dust layers from clouds. Very optically thin ($0<\tau<0.1$) dust layers look similar to clear pixels.

We see similar characteristics with the MODIS reflectance ratio ($R_{0.47\mu m}/R_{0.64\mu m}$) in Fig. 4.6. The $R_{0.47\mu m}/R_{0.64\mu m}$ of the cloud category is concentrated around 1. Again,

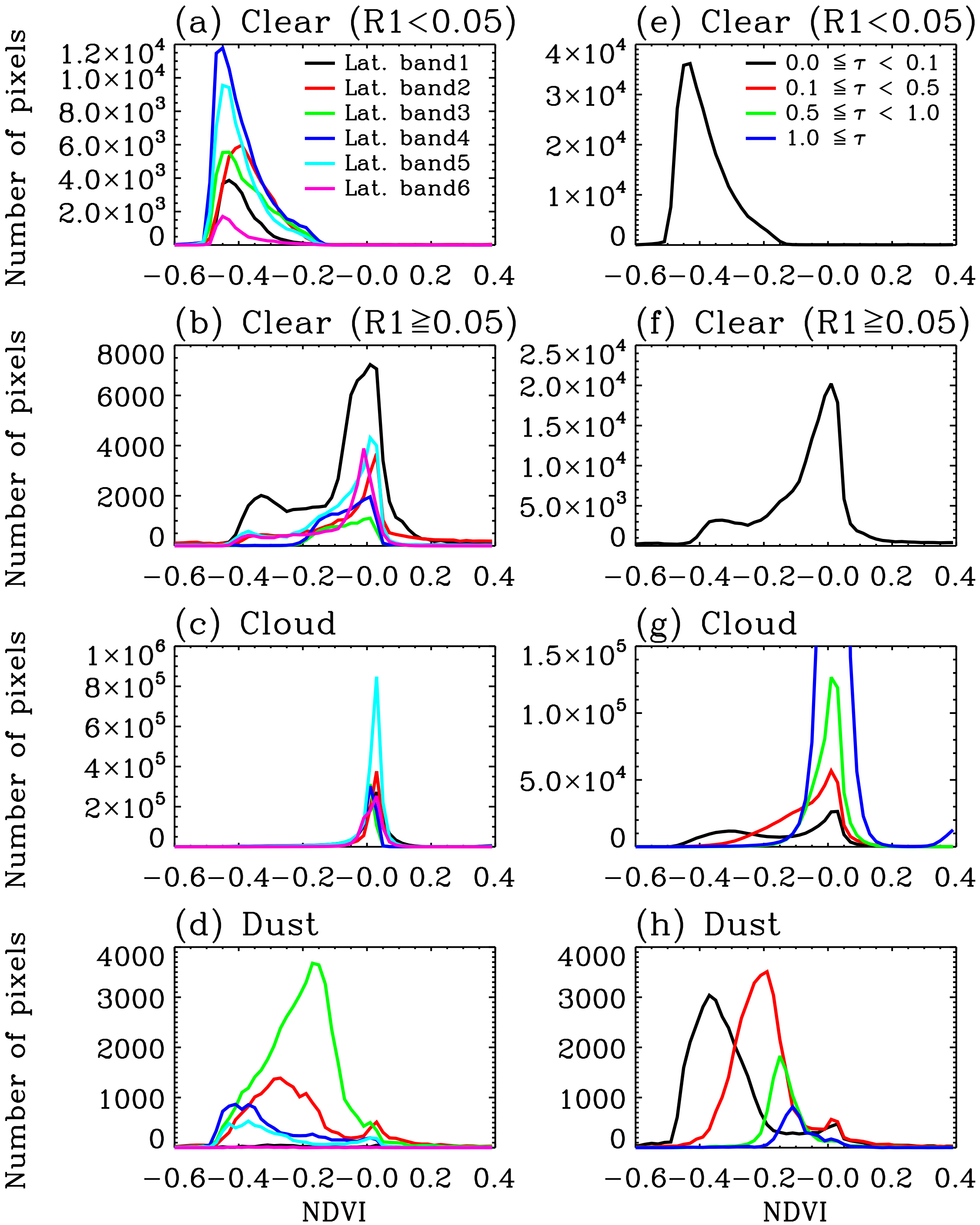

Fig. 4.5 Same as Fig. 4.4 except for normalized difference vegetation index (NDVI) (see Eqn. 4.2).

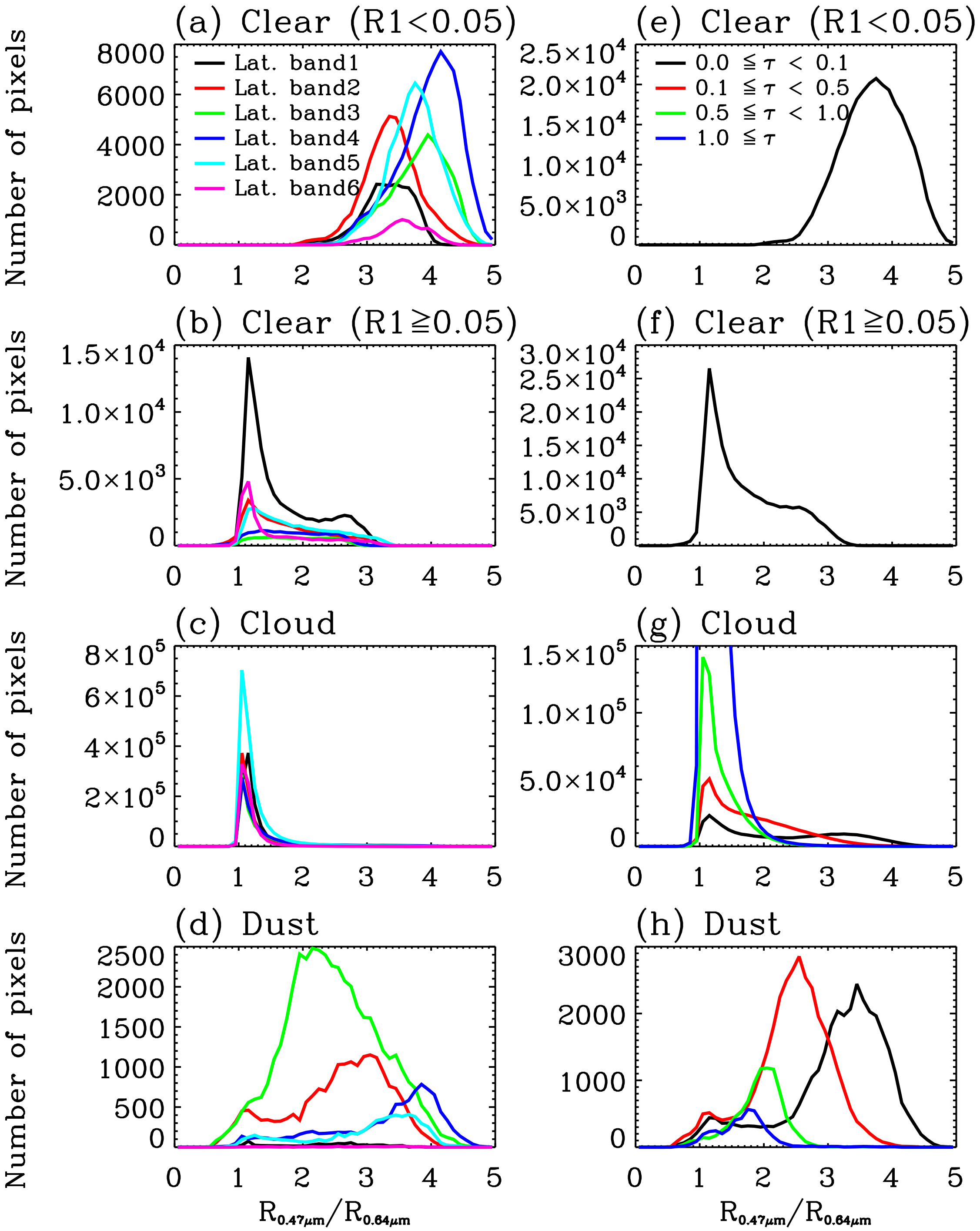

Fig. 4.6 Same as Fig. 4.4 except for the ratio of MODIS $R_{0.47\mu m}$ and $R_{0.64\mu m}$.

this is due to the similar reflectances of cloud at these wavelengths. For clear ($R_{0.64\mu m}$<0.05) category, the ratio is high (around 4) with little latitudinal dependence. The tropics (green and blue color in first row) in the clear ($R_{0.64\mu m}$<0.05) category have higher $R_{0.47\mu m}/R_{0.64\mu m}$ ratios than the high latitudes (black and purple). The reflectance ratio of dust decreases from similar to clear to more similar to cloud with increasing optical thickness.

Fig. 4.7 shows that NDDI shares similar characteristics with the other reflectance ratios. The NDDI for the clear ($R_{0.64\mu m}$<0.05) class is very narrow near -1.0, while cloud and dust categories have broader values through -0.9 to 0 (cloud) and -1.0 to -0.5 (dust) with optical thickness dependence. The NDDI values for cloud and dust increase with optical thickness. The dust NDDI for the tropics (green color in first row of Fig. 4.7d) tends to be much higher than other regions. This is because the optically thick dust layers are more frequently observed in this region. Overall, the reflectance ratios (NDVI, NDDI, and $R_{0.47\mu m}/R_{0.64\mu m}$) will be helpful in our new algorithm to separate dust layers both from cloud and clear scene.

Figs. 4.8 and 4.9 show the MODIS BTD distributions between 8.5-11 μm (Fig. 4.8) and 11-12 μm (Fig. 4.9). The $BTD_{8.5\text{-}11\mu m}$ of dust looks similar to that of clear pixels ($R_{0.64\mu m}$ <0.05). The $BTD_{8.5\text{-}11\mu m}$ distribution of cloudy scenes is broader and overlaps that of the clear ($R_{0.64\mu m}$<0.05) and dust categories. The $BTD_{8.5\text{-}11\mu m}$ of cloud increases with optical thickness, as shown in Ackerman (1997). However, the $BTD_{11\text{-}12\mu m}$ of cloud in Fig. 4.9 shows much less dependence on optical thickness than $BTD_{8.5\text{-}11\mu m}$. Alone, the BTDs are not sufficient to separate dust from clear or cloudy scenes, but they may

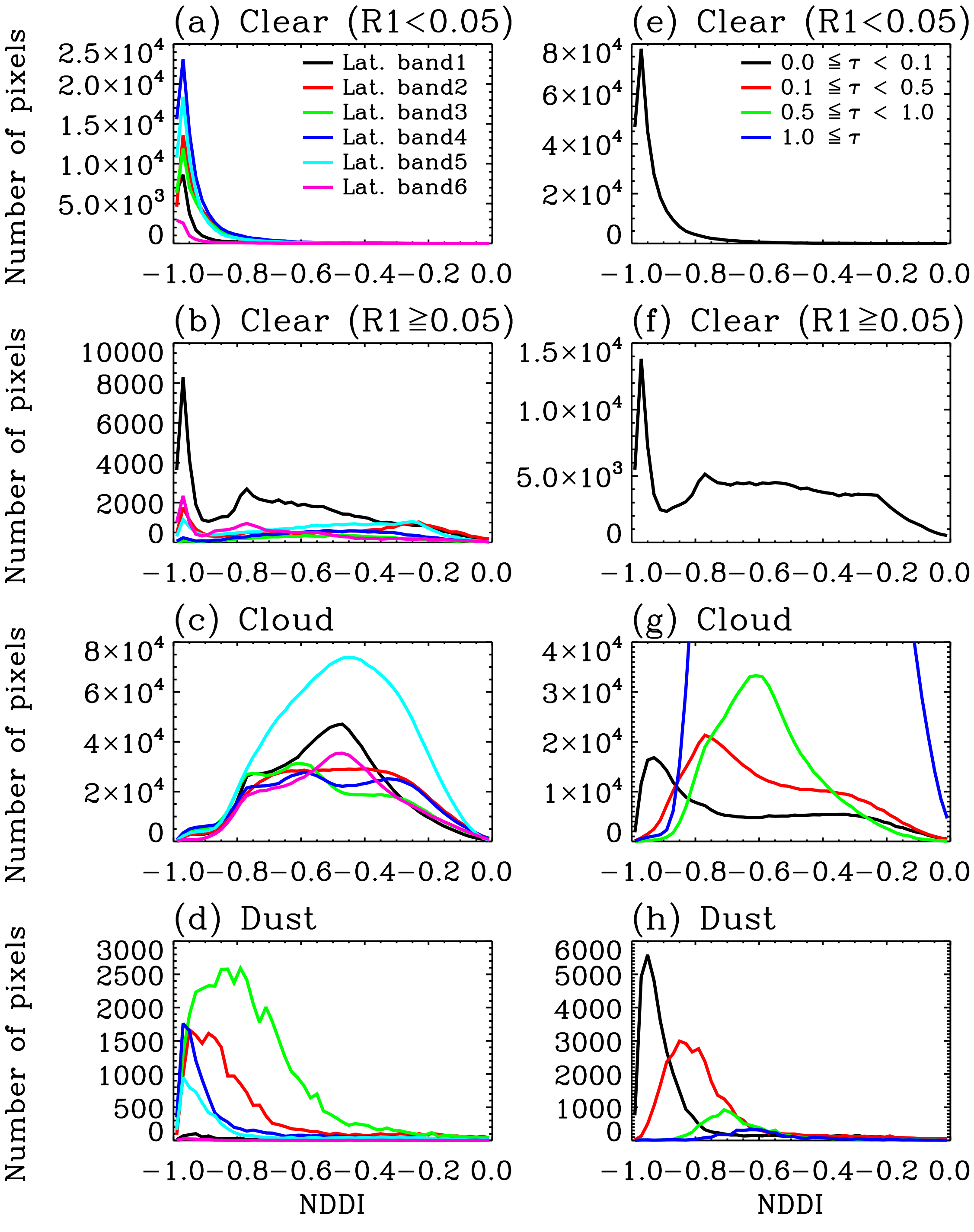

Fig. 4.7 Same as Fig. 4.4 except for normalized difference dust index (NDDI).

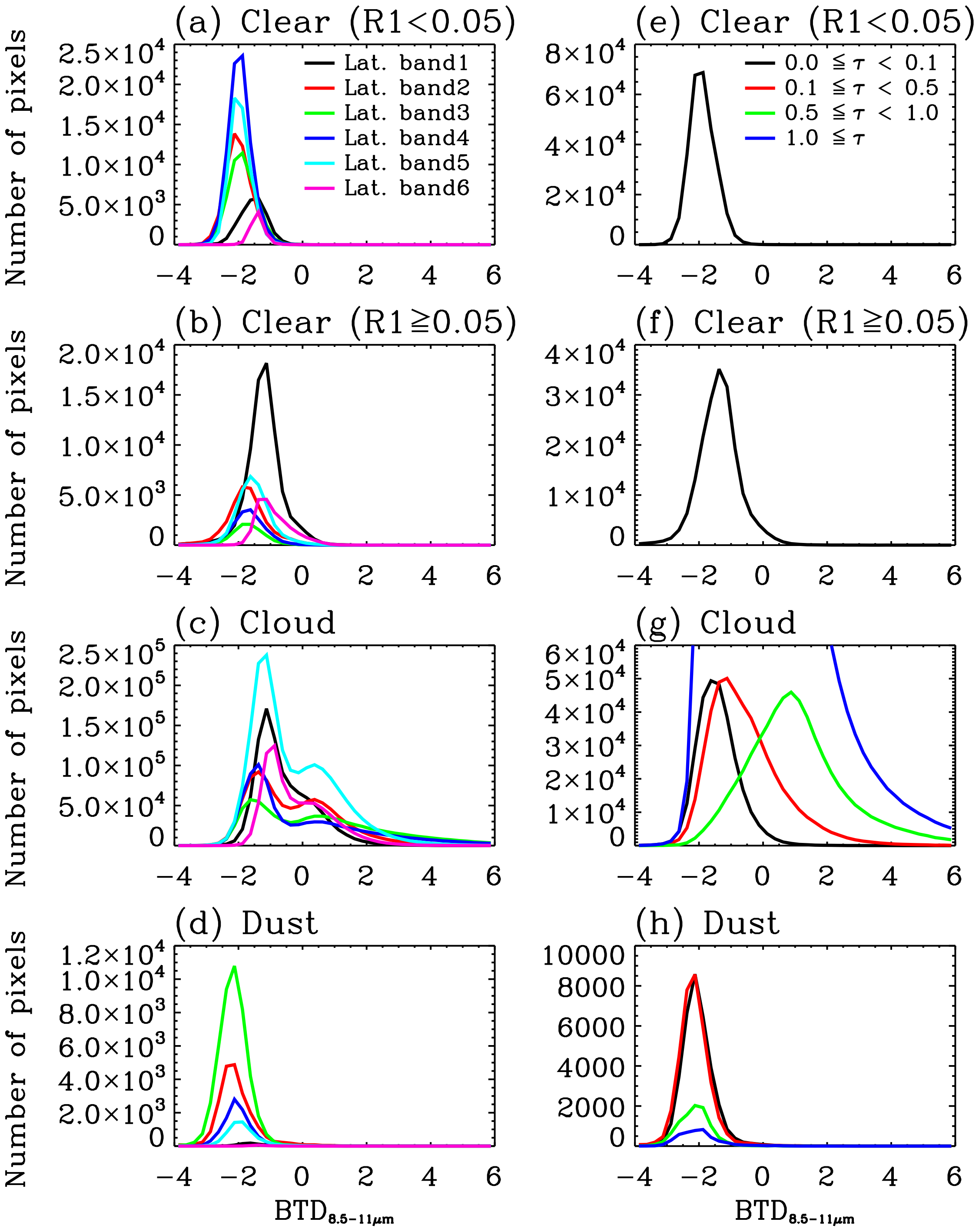

Fig. 4.8 Same as Fig. 4.4 except for $\mathrm{BTD}_{8.5\text{-}11\mu\mathrm{m}}$.

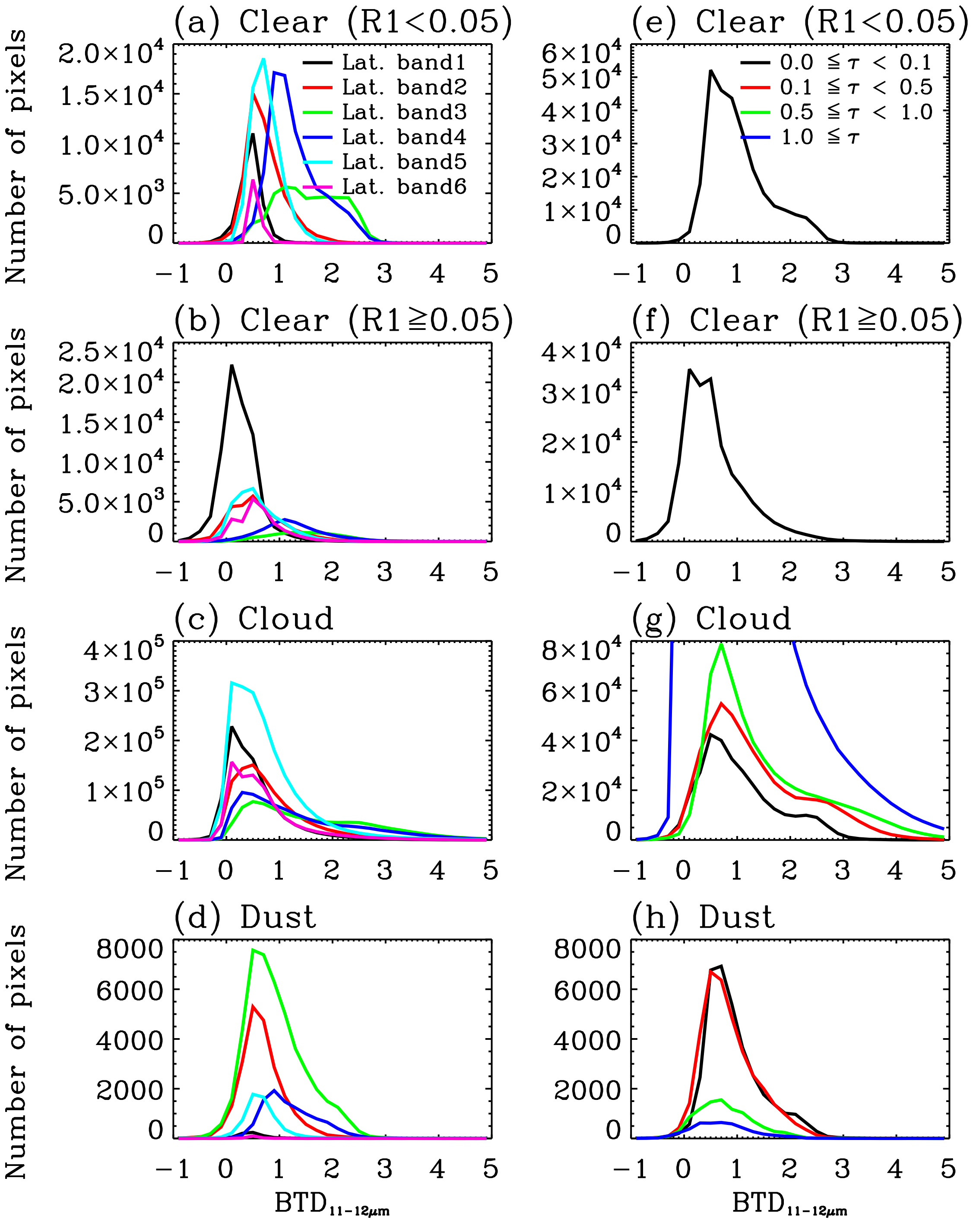

Fig. 4.9 Same as Fig. 4.4 except for $\mathrm{BTD}_{11\text{-}12\mu\mathrm{m}}$.

contribute to our algorithm in combination with other parameters.

4.5 A New Multi-spectral MODIS Algorithm using Discriminant Analysis

We have developed a new multi-spectral MODIS algorithm for the detection of optically thin mineral dust layer over the ocean. The algorithm is based on discriminant analysis (DA) and uses MODIS visible ($R_{0.47\mu m}$, $R_{0.55\mu m}$, and $R_{0.64\mu m}$), near-infrared ($R_{0.86\mu m}$, and $R_{2.13\mu m}$) and thermal infrared window ($BT_{8.5\mu m}$, $BT_{11\mu m}$, and $BT_{12\mu m}$) channels. This algorithm uses a combination of the six parameters introduced in the previous section to separate dust from cloud and clear scenes. Discriminant analysis is used to determine algorithm thresholds for each of the spectral parameters.

4.5.1 Discriminant analysis

Discriminant analysis is a statistical method of assigning an object to one of a number of possible classes (types or groups) on the basis of a set of features (MODIS measurements, in this case). The discriminant analysis finds the dividing function between the measurements by finding the maximum conditional probability based on the Bayes' rule. In this study, we have used two discriminant analyses methods: Linear (LDA) and Quadratic (QDA) discriminant analysis. Linear and quadratic discriminant analyses divide the sample space with linear and quadratic functions, respectively. For example, LDA uses straight a line to divide the two areas of a sample space with two variables and uses flat surfaces for three variables in the case of two classes.

If it is assumed that each CALIPSO class has multivariate normal distribution and all classes have different covariance matrixes, the quadratic discriminant analysis formula can be used, which is defined as,

$$d_i = \ln\left(\left|\mathbf{C}_i\right|\right) + \left(\mathbf{x} - \mu_i\right)^T \mathbf{C}_i^{-1}\left(\mathbf{x} - \mu_i\right) - 2\ln\left(\mathbf{P}(i)\right), \tag{4.4}$$

where $\mathbf{C}_i$ is covariance matrix of class *i*, **x** is measurement, μ_i is the average of class *i*, and **P** is prior probability of class *i*. We can classify the types by assigning object **x** to class *i* that has minimum d_i. If we add the additional assumption that all classes have the same covaiance matrix, the linear discriminat analysis formula can be obtained as follows; (see Appendix for the derivation of these formulas)

$$f_i = \mu_i \mathbf{C}^{-1}\mathbf{x}^T - \frac{1}{2}\mu_i \mathbf{C}^{-1}\mu_i^T + \ln\left(\mathbf{P}(i)\right). \tag{4.5}$$

Object **x** will be assigned to class *i* that has maximum of f_i. James (1985) provides more information about discriminant methods.

In our application, six parameters for three classes (clear, cloud, and dust) of MODIS data collocated with CALIPSO from 2008 are used as a training data set. We only use the clear pixels having MODIS 0.64-µm reflectance less than 0.05 for the clear category in the training data set. We establish the lookup tables of covariance matrixes, means and prior probabilities of each class for six latitude bands (-90 to -60, -60 to -30, -30 to 0, 0 to 30, 30 to 60, and 60 to 90^o) and four seasons. Since this algorithm uses reflectances over ocean, we screen out the sun-glint area in the analysis. If a latitude band and season pair does not contain a sufficient number of dusty pixels, the algorithm classifies the granule as ‘undetermined’.

4.6 Application of the New Dust Detection Algorithm

4.6.1 Case study

Fig. 4.10 demonstrates the application of the discriminant analysis dust detection algorithms to the April 2, 2008 granule shown in Fig. 4.1. The Saharan desert dust along the CALIPSO track has relatively low aerosol optical thickness (AOT) of around 0.5 according to MODIS (Fig. 4.10b). The results (Fig. 4.10c, and d) of both discriminant analysis methods and both appear to detect areas with thin dust. Comparing the two, the QDA method classifies more large dusty area, but the pattern is similar to LDA method result. However, these methods misclassify the thick dust region near the coastline of Africa (right side of each panel) as cloud. This is probably due to similar spectral characteristics between clouds and thicker dust in several of our parameters. The lack of a large number of thick dust scenes in our CALIPSO-based training data set is also issue. Fig. 4.11 shows an example of Asian dust case on April 15, 2008 (0430 UTC). A dust layer is seen over the ocean along the CALIPSO track, although it is difficult to see in MODIS RGB image (Fig. 4.11a). The MODIS retrievals show low values of aerosol optical thickness (Fig. 4.11b). Similar to the Saharan dust case, both methods seem to detect thin dust layers.

4.6.2 Evaluation with CALIPSO products

We also evaluate the new dust detection algorithm with co-located MODIS and CALIPSO data from 2009. These data are independent of our 2008 training data set. In

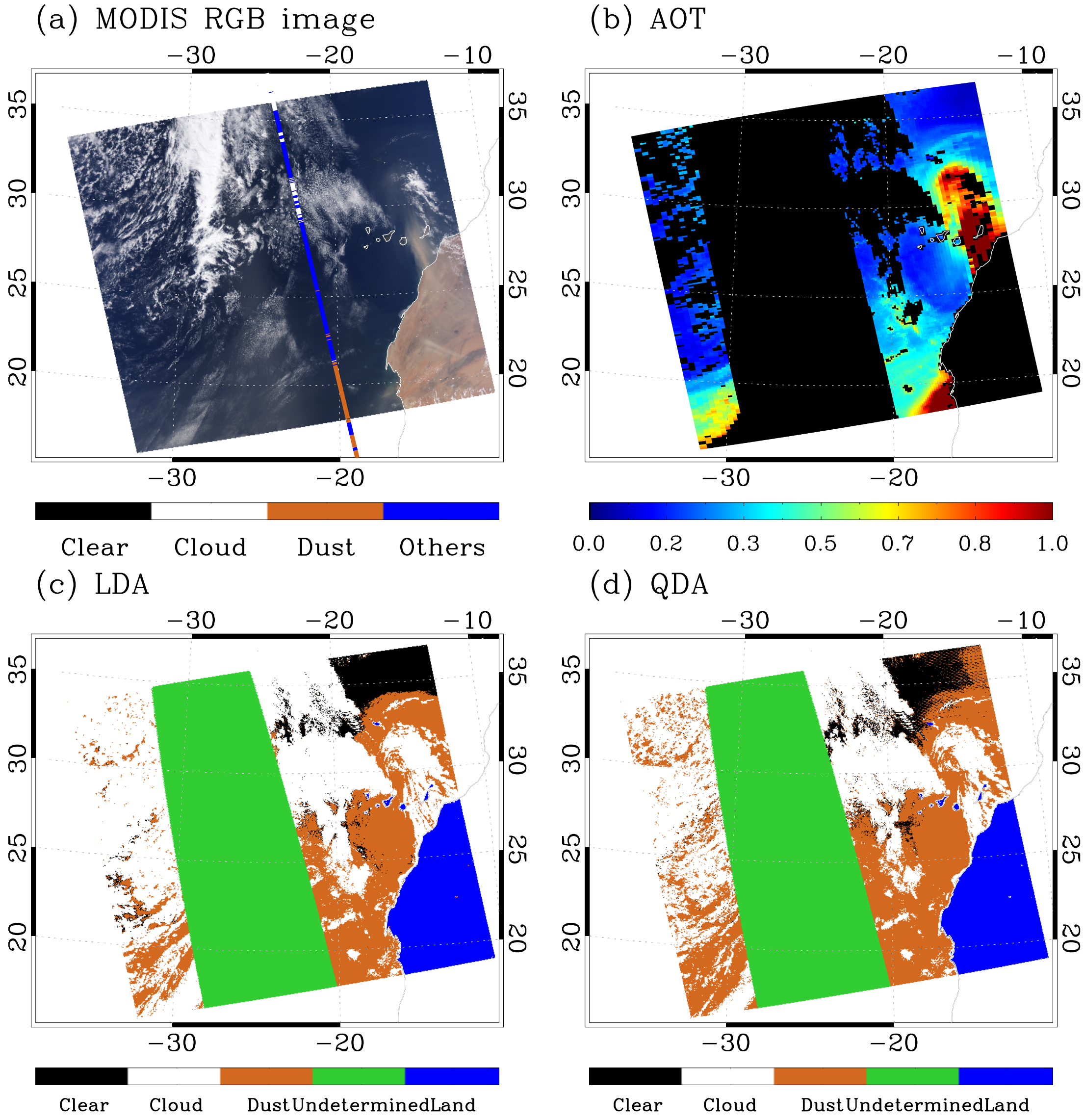

Fig. 4.10 (a) MODIS RGB image on April 2, 2008 (1450 UTC) with the CALIPSO track, (b) aerosol optical thickness, and (c) dust detection results for the LDA, and (d) for the QDA methods. Black, white, and orange colors in (a), (c), and (d) represent clear, cloud, and dust pixels, respectively. Blue in (a) refers to the CALIPSO 'other' classification. Green in (c and d) represents undetermined pixels, typically due to sunglint. Blue in (c and d) marks land surfaces.

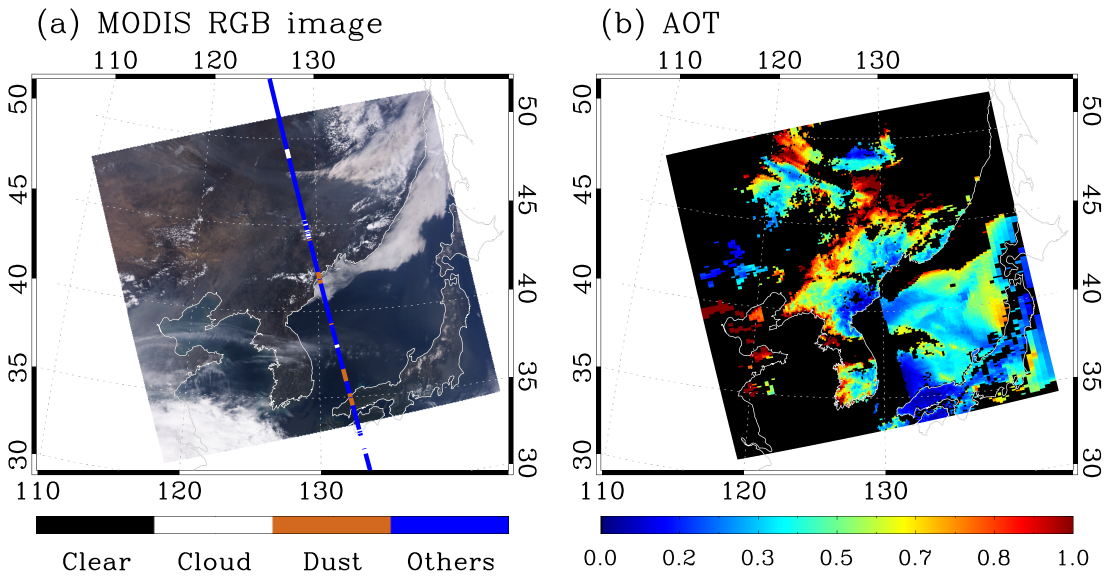

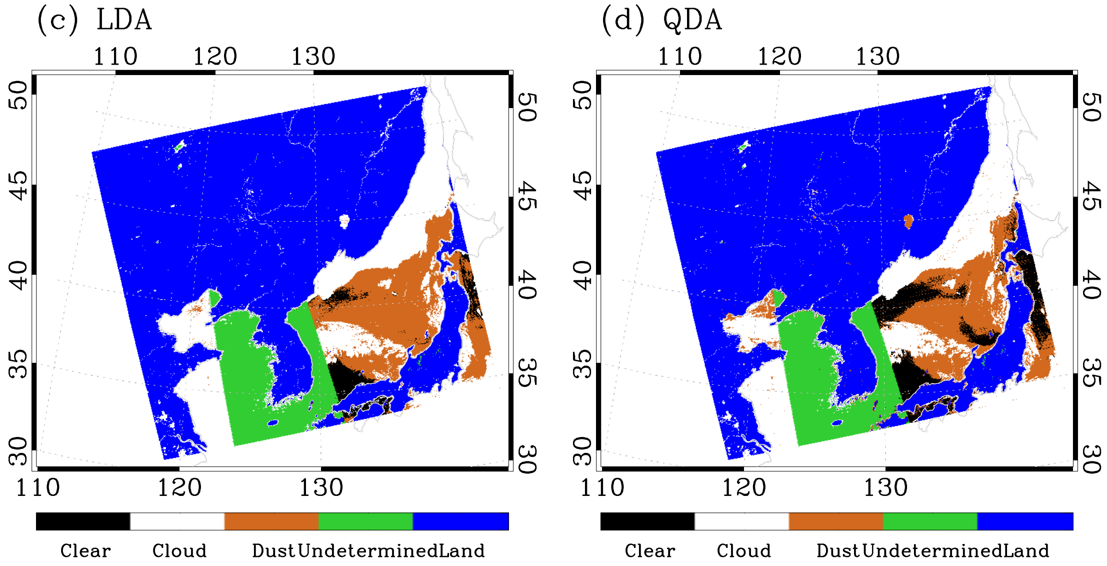

Fig. 4.11 Same as Fig. 4.10 except for on April 15, 2008 (0430 UTC).

the evaluation, all CALIPSO categories (Clear ($R_{0.64\mu m}$<0.05), Cloud, Dust, Clear ($R_{0.64\mu m}$≥0.05), Others) are employed. The number of pixels for each CALIPSO and new algorithm (clear, cloud, and dust) category for the LDA method are shown in Table 4.2, while Table 4.3 has the QDA results. The percentages represent the percentage of each

LDA or QDA class numbers out of the total number of the CALIPSO class. Note that in each discriminant classification, each clear, cloudy and dusty pixel is categorized according to the conditional probability (P) of 0.8 to indicate the degree of confidence in the selection. The lower probability (P<0.8) indicates lower confidence in the DA classification.

Table 4.2 The statistics of the new MODIS LDA algorithm over ocean during 2009. Note that each LDA classification is broken into two degrees of confidence according to the conditional probability (P<0.8 implies lower confidence than P≥ 0.8). Values in bold indicate agreement between the MODIS LDA and CALIPSO categories.

			CALIPSO category					
			Clear (R1<0.05)	Cloud	Dust	Clear (R1≥0.05)	Others	Sum
LDA Classification	Clear	P<0.8	21,800 (8.7%)	31,920 (0.5%)	5,853 (9.6%)	4,851 (3.2%)	504,065 (10.6%)	568,489
		P≥0.8	210,276 (83.9%)	69,922 (1.1%)	12,928 (21.2%)	11,829 (7.7%)	1,090,659 (22.9%)	1,395,614
	Cloud	P<0.8	4,555 (1.8%)	27,792 (0.5%)	2,310 (3.8%)	2,478 (1.6%)	243,918 (5.1%)	281,053
		P≥0.8	5,601 (2.2%)	5,933,029 (97.4%)	9,575 (15.7%)	125,501 (81.8%)	2,442,861 (51.4%)	8,516,567
	Dust	P<0.8	5,908 (2.4%)	16,052 (0.3%)	6,634 (10.9%)	4,550 (3.0%)	254,872 (5.4%)	288,016
		P≥0.8	2,427 (1.0%)	11,625 (0.2%)	23,800 (39.0%)	4,220 (2.8%)	218,345 (4.6%)	260,417
Total			250,567	6,090,340	61,100	153,429	4,754,720	11,310,156

Table 4.3 Same as Table 2, but for the QDA method.

		CALIPSO category					
		Clear (R1<0.05)	Cloud	Dust	Clear (R1≥0.05)	Others	Sum
QDA Classification Clear	P<0.8	10,304 (4.1%)	21,653 (0.4%)	5,671 (9.3%)	3,880 (2.5%)	387,239 (8.1%)	428,747
	P≥0.8	228,406 (91.2%)	95,752 (1.6%)	16,347 (26.8%)	14,937 (9.7%)	1,563,337 (32.9%)	1,918,779
QDA Classification Cloud	P<0.8	2,016 (0.8%)	25,462 (0.4%)	1,727 (2.8%)	5,333 (3.5%)	221,115 (4.7%)	255,653
	P≥0.8	2,192 (0.9%)	5,913,430 (97.1%)	6,594 (10.8%)	117,165 (76.4%)	2,063,122 (43.4%)	8,102,503
QDA Classification Dust	P<0.8	4,226 (1.7%)	17,145 (0.3%)	6,209 (10.2%)	5,124 (3.3%)	284,414 (6.0%)	317,118
	P≥0.8	3,423 (1.4%)	16,898 (0.3%)	24,552 (40.2%)	6,990 (4.6%)	235,493 (5.0%)	287,356
Total		250,567	6,090,340	61,100	153,429	4,754,720	11,310,156

Almost half of the CALIPSO dust pixels (P<0.8 and P≥0.8) are detected as dust by using the LDA method (Table 4.2). Those scenes misclassified by LDA as dust are largely assigned with low confidences. For example, the 2.4% of total CALIPSO clear ($R_{0.64\mu m}<0.05$) class are classified as low confidence LDA dust class. It is over twice number of high confidence LDA dust class. The percentage of false detection in the CALIPSO clear ($R_{0.64\mu m}<0.05$) and cloud categories is very low. The percentages of dusty pixels by discriminant analysis technique over CALIPSO clear and cloud pixels are 3.4% and 0.5% by LDA and 5.0% and 1.3% by QDA, which is an improvement compared to the other methods in section 4.2. As expected, most cloud-contaminated clear ($R_{0.64\mu m} \geq 0.05$) CALIPSO category are classified as cloud by discriminant analysis. Over all, these discriminant analysis methods more effectively separate dust from cloud and clear pixels than the methods discussed in section 4.3. Although a significant fraction of CALIPSO dust scenes are not detected, the number of clear and cloudy scenes misclassified as dust by LDA is much lower compared with the other methods.

CALIPSO retrievals of dust and cloud optical thickness provide another way to evaluate the performance of the discriminant analysis-based algorithms. The CALIPSO optical thickness histograms for CALIPSO cloud and dust categories with two confidence classes from LDA result are shown in Fig. 4.12 (for cloud) and Fig. 4.13 (for dust). For scenes described by CALIPSO as cloud (Fig. 4.12), most with optical thickness greater than 0.5 are classified as cloud with high confidence. If the cloud optical thickness is less than 0.5, LDA may classify as clear or dust. Fig. 4.13 shows that most scenes described by CALIPSO as dust with optical thickness between 0.1 and 2.0 are classified as dust with high confidence by LDA. The LDA technique is not effective at separating clear, cloud, and dust types when the CALIPSO cloud or dust optical thickness is very low (less than 0.1). This is likely due to the lack of sensitivity in the MODIS reflectances in these cases. The QDA technique shows similar result as the LDA (not shown).

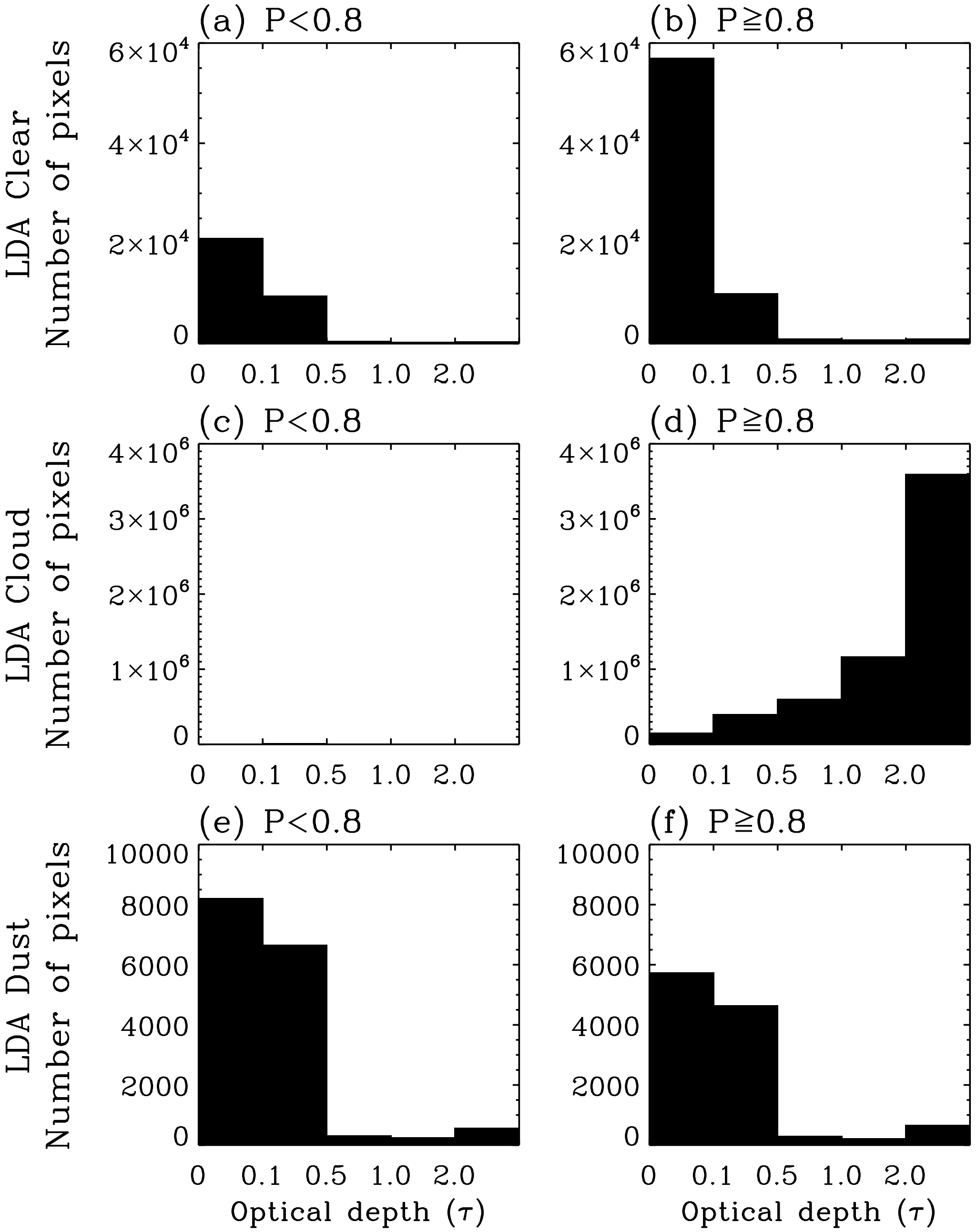

Fig. 4.12 CALIPSO cloud optical thickness histograms for LDA classifications [Clear (a and b), Cloud (c and d), and Dust (e and f)] for the CALIPSO cloud category. Left panels show lower confidence classifications, while right panels indicate higher confidence ones.

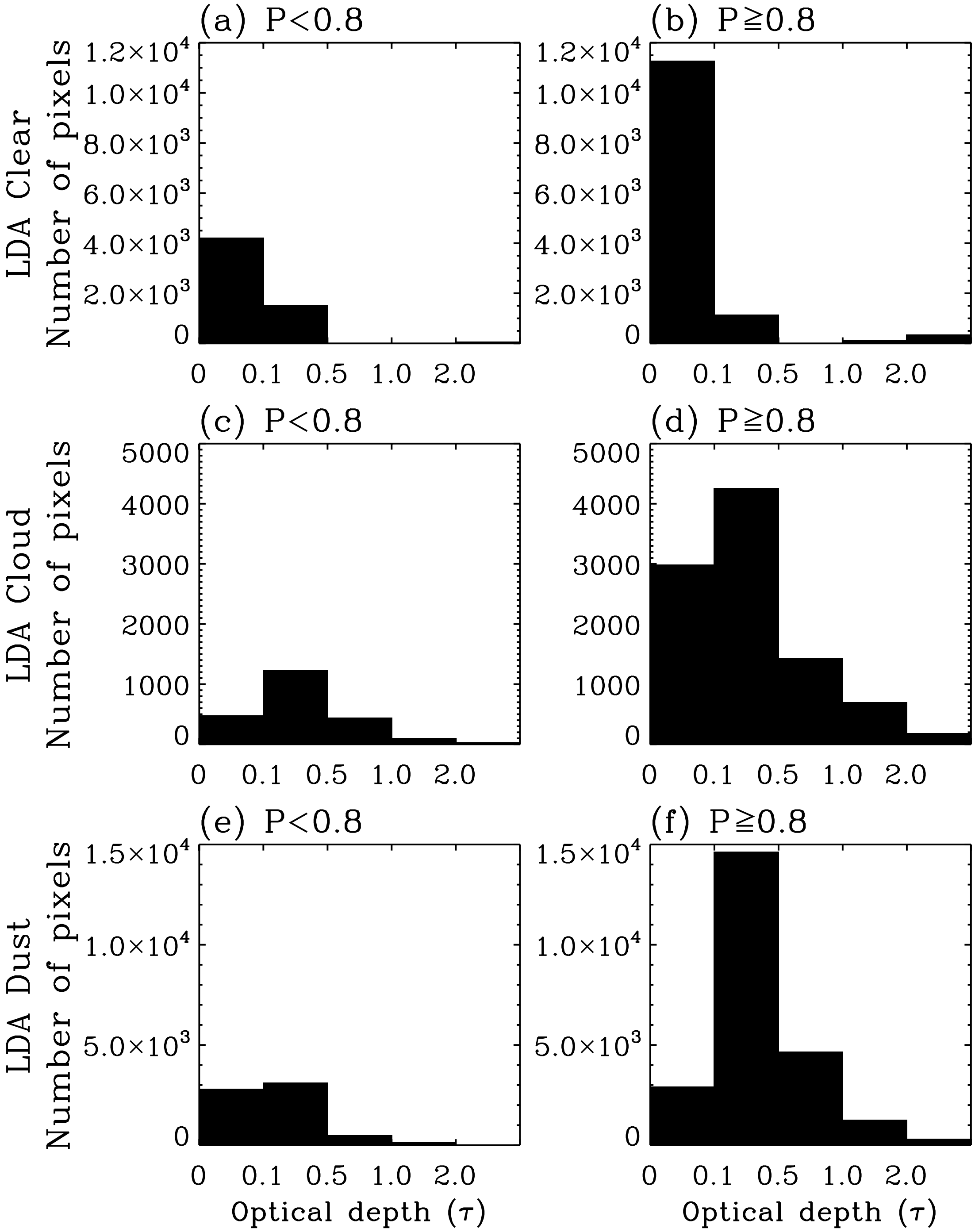

Fig. 4.13 Same as Fig. 4.12 except for the CALIPSO dust category.

4.7 Summary and Conclusions

In this section, we evaluate three dust detection methods with CALIPSO products and investigate the MODIS radiative signature of the mineral dust detected by CALIPSO satellite. Based on this analysis, we implement a new dust detection algorithm for MODIS by using discriminant analysis and evaluate this new algorithm.

The three existing dust detection algorithms including BTD procedure, D parameter method, and multi-channel image algorithm are evaluated for the daytime over ocean surface with CALIPSO aerosol product. The analysis shows that these techniques may be effective for detection of highly concentrated dust, while these algorithms may have difficulties in detecting optically thin dust layers. The six parameters including reflectance ratios, BTDs, and a standard deviation of reflectance are analyzed for radiative signature of the dust, cloud, and clear scenes detected by CALIPSO satellite. Reflectance ratios (NDVI, NDDI, and $R_{0.47\mu m}/R_{0.64\mu m}$) and standard deviation of reflectance (STD3[R4]) are confirmed to be useful to discriminate dust from clear or cloud, while BTDs (BTD8.5-11µm, and BTD11-12µm) didn't show the significant differences between dust and clear/clouds. From this analysis, we implement a new dust detection algorithm for MODIS by using discriminant analysis to combine the visible and IR measurements observations, including information about spatial variability. The CALIPSO cloud and aerosol classification with an aid of MODIS reflectance is used as training data set in the development of a new algorithm. The training data set uses data from collocated MODIS and CALIOP data from 2008. Results are also evaluated using data from 2009. The new algorithm looks effective for dust optical thickness between

0.1 and 2.0. In order to discriminate between cloud and optically thick dust, combining other method such as BTD method and the D-parameter technique is necessary.

5. SUMMARY

In this dissertation, we investigated the microphysical properties of aerosols and clouds with newly available global observations of lidar depolarization ratio and backscatter relationships, which allow us to retrieve particle thermodynamic phase and shape and/or orientation of aerosols and clouds.

In section 2, spaceborne polarization lidar, CALIPSO lidar, are introduced and its unique capabilities are demonstrated by presenting the relationships between lidar backscatter and the corresponding depolarization ratio for different cloud classifications and aerosol subtypes. Specifically, the operational MODIS cloud optical thickness and cloud-top pressure products are used to classify cloud types on the basis of the ISCCP cloud classification scheme. While the CALIPSO observations provide information for up to 10 cloud layers, in the present study only the uppermost clouds are considered. The layer-averaged attenuated backscatter (γ') and layer-averaged depolarization ratio (δ) from the CALIPSO measurements show both water- and ice-phase features for global cirrus, cirrostratus, and deep convective cloud classes. Furthermore, we screen both the MODIS and CALIPSO data to eliminate cases in which CALIPSO detected two- or multi-layered clouds. It is shown that low γ' values corresponding to uppermost thin clouds are largely eliminated in the CALIPSO δ-γ' relationship for single-layered clouds. For mid-latitude and polar regions corresponding, respectively, to latitude belts 30º-60º and 60º-90º in both the hemispheres, a mixture of water and ice is also observed in the case of the altostratus class. MODIS cloud phase flags are also used to screen ice clouds.

The resultant water clouds flagged by the MODIS algorithm show only water phase feature in the δ-γ' relation observed by CALIOP; however, in the case of the ice clouds flagged by the MODIS algorithm, the co-existence of ice- and water-phase clouds is still observed in the CALIPSO δ-γ' relationship.

In the δ-γ' relation for the aerosol types, the attenuated backscatter of dust type is similar to that other aerosol types. However, the depolarization ratio of dust is much higher than others due to its nonspherical characteristics. Thus, dust aerosol type can be well separated from other aerosol types, and can be used in evaluation of MODIS dust detection algorithms.

In section 3, we evaluate the MODIS IR cloud phase with the CALIPSO cloud products. The three possible misclassifications of MODIS cloud phase mentioned in radiative transfer modeling study by Nasiri and Kahn (2008) are tested by comparing between MODIS IR phase and CALIOP observations for single-layer clouds (54% of the cloudy CALIOP scenes) and for the top-layer of the CALIOP scenes. Both CALIOP and MODIS retrieve larger fractions of water clouds in the single-layer cases than in the top-layer cases, demonstrating that focusing on only single-layer clouds may introduce a water cloud bias. Of the single-layer clouds, 60% are transparent and 40% are opaque (defined by the lack of a CALIOP ground return). MODIS tends to classify single-layer clouds with mid-layer temperatures below -40°C as ice, around -30°C nearly equally as ice, mixed, and unknown, between -28°C and -15° as mixed, and above 0°C as water. 95% of the single-layer CALIOP clouds not detected by MODIS are transparent. Approximately 1/3 of transparent single-layer clouds with temperatures below -30°C are not detected by MODIS, close to another 1/3 are classified as ice, with the rest as either water, mixed, or unknown. CALIOP classes nearly all of these transparent cold clouds as ice.

In section 4, we evaluate three dust detection methods with CALIPSO product. The dust detection algorithms including BTD procedure, D parameter method, and multi-channel image algorithm may have difficulties in detecting optically thin dust layers. These techniques may be effective for detection of highly concentrated dust. We also investigate the MODIS radiative signature of the mineral dust detected by CALIPSO satellite. Based on this analysis, we implement a new dust detection algorithm for MODIS by using discriminant analysis with combining the visible and IR measurements as well as the information about spatial variability. The new algorithm is effective for dust optical thickness between 0.1 and 2.

REFERENCES

Ackerman, S. A., 1989: Using the radiative temperature difference at 3.7 and 11 μm to track dust outbreaks. *Remote Sens. Environ.*, **27**, 129−133.

Ackerman, S. A., 1997: Remote sensing aerosols using satellite infrared observations. *J. Geophys. Res.*, **102**, 17 069−17 080.

Ackerman, S. A., R. E. Holz, R. Frey, E. W. Eloranta, B. C. Maddux, and M. McGill, 2008: Cloud detection with MODIS. Part II: Validation. *J. Atmos. Oceanic Technol.*, **25**, 1073–1086.

Albrecht, B. A., 1989: Aerosols, cloud microphysics, and fractional cloudiness. *Science,* **245**, 1227–1230.

Ångström, A., 1962: Atmospheric turbidity, global illumination and planetary albedo of the earth. *Tellus,* **14**, 435–450.

Baddock, M., J. Bullard, and R. Bryant, 2009: Dust source identification using MODIS: A comparison of techniques applied to the Lake Eyre Basin, Australia. *Remote Sens. Environ.*, **113**, 7, 1511−1528.

Barnes, W. L., T. S. Pagano, and V. V. Salomonson, 1998: Pre-launch characteristics of the Moderate Resolution Imaging Spectroradiometer (MODIS) on EOS-AM1. *IEEE Trans. Geosci. Remote Sens.*, **36**, 1088–1100.

Baum, B. A., P. F. Soulen, K. I. Strabala, M. D. King, S. A. Ackerman, P. Menzel and P. Yang, 2000: Remote sensing of cloud properties using MODIS airborne simulator imagery during SUCCESS 2. Cloud thermodynamic phase. *J. Geophys.*

Res., **105**, 11 781−11 792.

Brennan, J. I., Y. J. Kaufman, I. Koren, and R. R. Li, 2005: Aerosol-cloud interaction: Misclassification of MODIS clouds in heavy aerosol. *IEEE Trans. Geosci. Remote Sens.*, **43**, 911–915, doi:10.1109/TGRS.2005.844662.

Bullard, J. E., M. C. Baddock, G. H. McTainsh, and J. F. Leys, 2008: Sub-basin scale dust source geomorphology detected using MODIS. *Geophys. Res. Lett.*, **35**(15), L15404, doi:10.1029/2008GL033928.

Chepfer, H., G. Brogniez, P. Goloub, F. M. Breon, and P. H. Flamant, 1999: Observations of horizontally oriented ice crystals in cirrus clouds with POLDER-1/ADEOS-1. *J. Quant. Spectro. Radiat. Transfer,* **63**, 521−543.

Cho, H.-M., P. Yang, G. W. Kattawar, S. L. Nasiri, Y. Hu, P. Minnis, C. Trepte, D. Winker, 2008: Depolarization ratio and attenuated backscatter for nine cloud types: analyses based on collocated CALIPSO lidar and MODIS measurements. *Opt. Express*, **16**, 3931−3948.

Cho, H.-M., S. L. Nasiri, P. Yang, 2009: Application of CALIOP measurements to the evaluation of cloud phase derived from MODIS infrared channels. *J. Appl. Meteor. Climatol.*, **48**, 2169−2180.

Chylek, P., S. Robinson, M. K. Dubey, M. D. King, Q. Fu, and W. B. Clodius, 2006: Comparison of near-infrared and thermal infrared cloud phase detections. *J. Geophys. Res.*, **111**, D20203, doi:10.1029/2006JD007140.

Claquin, T., C. Roelandt, K. E. Kohfeld, S. P. Harrison, I. Tegen, I. C. Prentice, Y. Balkanski, G. Bergametti, M. Hansson, N. Mahowald, H. Rodhe, and M. Schulz, 2003: Radiative forcing of climate by ice-age atmospheric dust. *Clim. Dynam.*, **20**, 193−202.

Darmenov, A., and I. N. Sokolik, 2005: Identifying the regional thermal–IR radiative signature of mineral dust with MODIS. *Geophys. Res. Lett.*, **32**, L16803, doi:10.1029/2005GL023092.

Duce, R. A., P. S. Liss, J. T. Merrill, E. L. Atlas, P. Buat-Menard, B. B. Hicks, J. M. Miller, J. M. Prospero, R. Arimoto, T. M. Church, W. Ellis, J. N. Galloway, L. Hansen, T. D. Jickells, A. H. Knap, K. H. Reinhardt, B. Schneider, A. Soudine, J. J. Tokos, S. Tsunogai, R. Wollast, and M. Zhou, 1991: The atmospheric input of trace species to the world ocean. *Global Biogeochem. Cyc.*, **5**, 193–259.

Dunion, J. P., and C. S. Velden, 2004: The impact of the Saharan air layer on Atlantic tropical cyclone activity. *Bull. Amer. Meteor. Soc.*, **84**, 353–365.

Ehrlich, A., M. Wendisch, E. Bierwirth, A. Herber, and A. Schwarzenböck, 2008: Ice crystal shape effects on solar radiative properties of Arctic mixed-phase clouds – Dependence on microphysical properties. *Atmos. Res.*, **88**, 266–276.

Evan, A. T., J. Dunion, J. A. Foley, A. K. Heidinger, and C. S. Velden, 2006a: New evidence for a relationship between Atlantic tropical cyclone activity and African dust outbreaks. *Geophys. Res. Lett.*, **33**, L19813, doi:10.1029/2006GL026408.

Evan, A. T., A. K. Heidinger, and M. J. Pavolonis, 2006b: Development of a new over-water advanced very high resolution radiometer dust detection algorithm. *Int. J. Remote Sens.*, **27**, 3903–3924, doi:10.1080/01431160600646359.

Evan, A. T., A. K. Heidinger, and P. Knippertz, 2006c: Analysis of winter dust activity off the coast of West Africa using a new 24-year over-water advanced very high resolution radiometer satellite dust climatology. *J. Geophys. Res.*, **111**, D12210, doi:10.1029/2005JD006336.

Frey, R. A., S. A. Ackerman, Y. Liu, K. I. Strabala, H. Zhang, J. R. Key, and X. Wang, 2008: Cloud Detection with MODIS. Part I: Improvements in the MODIS Cloud Mask for Collection 5. *J. Atmos. Oceanic Technol.*, **25**, 1057–1072.

Fu, Q., 1996: An accurate parameterization of the solar radiative properties of cirrus clouds for climate models. *J. Clim.*, **9**, 2058–2082.

Gassó, S., and A. F. Stein, 2007: Does dust from Patagonia reach the sub-Antarctic Atlantic Ocean. *Geophys. Res. Lett.*, **34**, doi:10.1029/2006GL027693.

Hansell, R. A., S. C. Ou, K. N. Liou, J. K. Roskovensky, S. C. Tsay, C. Hsu, and Q. Ji, 2007: Simultaneous detection/separation of mineral dust and cirrus clouds using MODIS thermal infrared window data. *Geophys. Res. Lett.*, **34**, L11808, doi:10.1029/2007GL029388.

Hao, X., and J. J. Qu, 2007: Saharan dust storm detection using MODIS thermal infrared bands. *J. Appl. Remote Sens.*, **1**, 013510.

Harrington, J. Y., T. Reisin, W. R. Cotton, and S. M. Kreidenweis, 1999: Cloud resolving simulations of Arctic stratus – Part II: Transition-season clouds. *Atmos. Res.*, **51**, 45–75.

Herman, J., P. Bhartia, O. Torres, C. Hsu, C. Seftor, and E. Celarier, 1997: Global distribution of UV-absorbing aerosols from Nimbus 7/TOMS data. *J. Gephys. Res. Atmos.*, **102**(D14), 16 911–16 922.

Higdon, N. S., E. V. Browell, P. Ponsardin, B. E. Grossmann, C. F. Butler, T. H. Chyba, M. N. Mayo, R. J. Allen, A. W. Heuser, W. B. Grant, S. Ismail, S. D. Mayor, and A. F. Carter, 1994: Airborne differential absorption lidar system for measurements of atmospheric water vapor and aerosols. *Appl. Opt.*, **33**, 6422−6438.

Ho, C.-H., M.-D. Chou, M. Suarez, and K.-M. Lau, 1998: Effect of ice cloud on GCM climate simulations. *Geophys. Res. Lett.*, **25**, 71−74.

Holz, R. E., S. A. Ackerman, F. W. Nagle, R. Frey, S. Dutcher, R. E. Kuehn, M. A. Vaughan, and B. Baum, 2008: Global Moderate Resolution Imaging Spectroradiometer (MODIS) cloud detection and height evaluation using CALIOP. *J. Geophys. Res.*, **113**, doi:10.1029/2008JD009837.

Houghton, J. T., Ding, Y., Griggs, D. J., Noguer, M., van der Linden, P. J., Xiaosu, D., Maskell, K. and Johnson, C. A. (Eds.), 2001: *Climate Change 2001: The Scientific Basis*. Cambridge University Press, Cambridge, UK. (Contribution of Working Group 1 to the Third Assessment Report of the Intergovernmental Panel on Climate Change.)

House, J. I., V. Brovkin, R. Betts, R. Constanza, M. A. Silva Dias, E. Holland, C. le Quere, N. Kim Phat, U. Riebesell, and M. Scholes, 2006: Climate and air quality, in *Ecosystems and Human Well-Being: Volume 1 Current State and Trends*, Findings of the Condition and Trends Working Group of the Millennium Ecosystem Assessment, Island Press, Washington, Covelo, London, 357–390.

Hu, Y., D. Winker, P. Yang, B. Baum, L. Poole, and L. Vann, 2001: Identification of cloud phase from PICASSO-CENA lidar depolarization: A multiple scattering sensitivity study. *J.Quant. Spectrosc. Radiat. Transfer*, **70**, 569–579.

Hu, Y., M. Vaughan, Z. Liu, B. Lin, P. Yang, D. Flittner, B. Hunt, R. Kuehn, J. Huang, D. Wu, S. Rodier, K. Powell, C. Trepte, and D. Winker, 2007: The depolarization – attenuated backscatter relation: CALIPSO lidar measurements vs. theory. *Opt. Express*, **15**, 5327−5332.

Hu, Y., D. Winker, M. Vaughan, B. Lin, A. Omar, C. Trepte, D. Flittner, P. Yang, S. L. Nasiri, B. Baum, R. Holz, W. Sun, Z. Liu, Z. Wang, S. Young, K. Stamnes, J. Huang, R. Kuehn, 2009: CALIPSO/CALIOP Cloud Phase Discrimination Algorithm. *J. Atmos. Oceanic Technol.*, **26**, 2293–2309, doi: 10.1175/2009JTECHA1280.1.

Husar, R. B., D. M. Tratt, B. A. Schichtel, S. R. Falke, F. Li, D. Jaffe, S. Gasso, T. Gill, N. S. Laulainen, F. Lu, M. C. Reheis, Y. Chun, D. Westphal, B. N. Holben, C. Gueymard, I. McKendry, N. Kuring, G. C. Feldman, C. McClain, R. J. Frouin, J. Merrill, D. DuBois, F. Vignola, T. Murayama, S. Nickovic, W. E. Wilson, K. Sassen, N. Sugimoto, and W. C. Malm, 2001: Asian Dust events of April 1998, *J. Geophys. Res.*, **106**, 18 317–18 330.

IPCC, 2007: *Climate Change 2007: The Physical Science Basis*; Working Group I Contribution to the Fourth Assessment Report of the IPCC; Cambridge University Press: New York, NY, USA, pp. 996.

Jaffe, D., T. Anderson, D. Covert, R. Kotchenruther, B. Trost, J. Danielson, W.

Simpson, T. Berntsen, S. Karlsdottir, D. Blake, J. Harris, G. Carmichael, and I. Uno, 1999: Transport of Asian air pollution to North America. *Geophys. Res. Lett.*, **26**, 711–714.

James, M., 1985: *Classification Algorithms*, John Wiley and Sons, pp. 209.

Kaufman, Y. J., B. N. Holben, D. Tanre, I. Slutsker, A. Smirnov, and T. F. Eck, 2000: Will aerosol measurements from Terra and Aqua polar orbiting satellites represent the daily aerosol abundance and properties? *Geophys. Res. Lett.*, **27**, 3861–3864.

King, M. D., S. Platnick, P. Yang, G. T. Arnold, M. A. Gray, J. C. Riédi, S. A. Ackerman, and K. N. Liou, 2004: Remote sensing of liquid water and ice cloud optical thickness and effective radius in the Arctic: Application of airborne multispectral MAS data. *J. Atmos. Oceanic Technol.*, **21**, 857–875.

Knap, W. H., P. Stammes, and R. B. A. Koelemeijer, 2002: Cloud thermodynamic-phase determination from near-infrared spectra of reflected sunlight. *J. Atmos. Sci.*, **59**, 83–96.

Legrand, M., Nertrand, J. J., Desbois, M., Menenger, L., and Fouquart, Y., 1989: The potential of infrared satellite data for the retrieval of Saharan dust optical depth over Africa. *J. Climate Appl. Meteor.*, **28**, 309−318.

Legrand, M., A. Plana-Fattori, and C. N’doumé, 2001: Satellite detection of dust using the IR imagery of Meteosat: 1. Infrared difference dust index. *J. Geophys. Res.*, **106**, 18 251–18 274.

Levin, Z., E. Ganor, and V. Gladstein, 1996: The effects of desert particles coated with sulfate on rain formation in the Eastern Mediterranean. *J. Appl. Meteorol.*, **35**, 1511–1523.

Li, Z., X. Zhao, R. Kahn, M. Mishchenko, L. Remer, K.-H. Lee, M. Wang, I. Laszlo, T. Nakajima, and H. Maring, 2009: Uncertainties in satellite remote sensing of aerosols and impact on monitoring its long-term trend: a review and perspective. *Ann. Geophys.*, **27**, 2755−2770.

Liou, K. N., 2002: *An Introduction to Atmospheric Radiation*, 2nd ed., Elsevier, New York, pp. 583.

Liou, K. N. and H. Lahore, 1974: Laser sensing of cloud composition: a backscattered depolarization technique. *J. Appl. Meteorol.*, **13**, 257–263.

Liu, Z., A. H. Omar, Y. Hu, M. A.Vaughan, and D. M. Winker, 2005: CALIOP algorithm theoretical basis document—Part 3: Scene classification algorithms. NASA Langley Research Center Doc. PC-SCI-202 Part 3, pp. 56. [Available online at http://wwwcalipso.larc.nasa.gov/resources/pdfs/PC-SCI-202_Part3_v1.0.pdf.]

Liu, Z., M. A. Vaughan, D. M. Winker, C. Kittaka, R. E. Kuehn, B. J. Getzewich, C. R. Trepte, and C. A. Hostetler, 2009: The CALIPSO Lidar Cloud and Aerosol Discrimination: Version 2 Algorithm and Initial Assessment of Performance. *J. Atmos. Oceanic Technol.*, **26**, 1198−1213, doi:10.1175/2009JTECHA1229.1.

Martins, J. V., D. Tanré, L. Remer, Y. Kaufman, S. Mattoo, and R. Levy, 2002: MODIS Cloud screening for remote sensing of aerosols over oceans using spatial variability, *Geophys. Res. Lett.*, **29**(12), 8009, doi:10.1029/2001GL013252.

McClatchey, R. A., R. W. Fenn, J. E. A. Selby, F. E. Volz, and J. S. Garing, 1972: *Optical properties of the atmosphere. (third ed.)*, AFCRL-72-0497, Air Force Cambridge Research Laboratories, pp. 108.

McCormick, R. A., and J. H. Ludwig, 1967: Climate modifications by atmospheric aerosols. *Science,* **156**, 1358–1359.

McGill, M. J., W. R. Skinner, and T. D. Irgang, 1997:Analysis technique for the recovery of winds and backscatter coefficients from a multiple-channel incoherent Doppler lidar. *Appl. Opt.*, **36**, 1253–1268.

Menzel, W. P., R. A. Frey, B. A. Baum, and H. Zhang, 2006: Cloud top properties and cloud phase. *NASA Algorithm Theor. Basis Doc.* ATBDMOD-04, pp. 56.

Menzel, W. P., R. A. Frey, H. Zhang, D. P. Wylie, C. C. Moeller, R. E. Holz, B. Maddux, B. A. Baum, K. I. Strabala, and L. E. Gumley, 2008: MODIS global cloud-top pressure and amount estimation: Algorithm description and results. *J. Appl. Meteor. Climatol.*, **47**, 1175–1198.

Miller, S. D., 2003: A consolidated technique for enhancing desert dust storms with MODIS. *Geophys. Res. Lett.*, **30**(20), 2071, doi:10.1029/2003GL018279.

Mishchenko, M. I., and K. Sassen, 1998: Depolarization of lidar returns by small ice crystals: An application to contrails. *Geophys. Res. Lett.*, **25**(3), 309−312.

Murayama T., N. Sugimoto, I. Uno, K. Kinoshita, K. Aoki, N. Hagiwara, Z. Liu, I. Matsui, T. Sakai, T. Shibata, K. Arao, B.-J. Sohn, J.-G. Won, S.-C. Yoon, T. Li, J. Zhou, H. Hu, M. Abo, K. Iokibe, R. Koga, and Y. Iwasaka, 2001: Ground-based network observation of Asian dust events of April 1998 in east Asia. *J.*

Geophys. Res., **106**, 18 345–18 360.

Nakajima, T., and M. D. King, 1990: Determination of the optical thickness and effective particle radius of clouds from reflected solar radiation measurements. Part I: Theory. *J. Atmos. Sci.*, **47**(15), 1878−1893.

Nasiri, S. L., and B. H. Kahn, 2008: Limitations of bispectral infrared cloud phase determination and potential for improvement. *J. Appl. Meteor. Climatol.*, **47**, 2895–2910.

Okada O., J. Heintzenberg, K. Kai, and Y. Qin, 2001: Shape of atmospheric mineral particles collected in three Chinese arid-regions. *Geophys. Res. Lett*., **28**, 3123–3126.

Omar, A., D. Winker, C. Kittaka, M. Vaughan, Z. Liu, Y. Hu, C. Trepte, R. Rogers, R. Ferrare, R. Kuehn, C. Hostetler, 2009: The CALIPSO automated aerosol classification and lidar ratio selection algorithm. *J. Atmos. Oceanic Technol.*, **26**, 1994−2014, doi:10.1175/2009-JTECHA1231.1.

Overpeck, J., D. Rind, A. Lacis, and R. Healy, 1996: Possible role of dust-induced regional warming in abrupt climate change during the last glacial period. *Nature*, **384**, 447−449, doi:10.1038/384447a0.

Patterson, E. M., D. A. Gillette, and B. H. Stockton, 1977: Complex index of refraction between 300 and 700 nm for Saharan aerosols. *J. Geophys. Res.*, **82**, 3153−3160.

Pavolonis, M. J., A. K. Heidinger, and T. Uttal, 2005: Daytime global cloud typing from AVHRR and VIIRS: Algorithm description, validation, and comparisons. *J. Appl. Meteor.*, **44**, 804–826.

Pilewskie, P., and S. Twomey, 1987: Cloud phase discrimination by reflectance measurements near 1.6 and 2.2 mm. *J. Atmos. Sci.*, **44**, 3419–3420.

Pincus, R. and M. B. Baker, 1994: Effect of precipitation on the albedo susceptibility of clouds in the marine boundary layer. *Nature*, **372**, 250−252, doi:10.1038/372250a0.

Platnick, S., M. D. King, S. A. Ackerman, W. P. Menzel, B. A. Baum, J. C. Riédi, and R. A. Frey, 2003: The MODIS cloud products: Algorithms and examples from Terra. *IEEE Trans. Geosci. Remote Sens.*, **41**, 459–473.

Platt, C. M. R., 1978: Lidar backscatter from horizontal ice crystal plates. *J. Appl. Meteor.*, **17**(4), 482−488.

Platt, C. M. R., S. C. Scott, and A. C. Dilley, 1987: Remote sounding of high clouds. Part VI: optical properties of midlatitude and tropical cirrus. *J. Atmos. Sci.*, **44**, 729−747.

Prospero, J. M., P. Ginoux, O. Torres, S. E. Nicholson, and T. E. Gill, 2002: Environmental characterization of global sources of atmospheric soil dust identified with the Nimbus 7 Total Ozone Mapping Spectrometer (TOMS) absorbing aerosol product. *Rev. Geophys.*, **40**, 1002, doi:10.1029/2000RG000095.

Qu, J. J., X. Hao, M. Kafatos, and L. Wang, 2006: Asian dust storm monitoring combining terra and aqua MODIS SRB Measurements. *IEEE Geosci. Remote Sens. Lett.*, **3**(4), 484−486.

Reichardt, S., and J. Reichardt, 2003: Effect of multiple scattering on depolarization measurements with spaceborne lidars. *Appl. Opt.,* **42**, 3620−3633.

Riédi, J., M. Doutriaux-Boucher, P. Goloub, and P. Couvert, 2000: Global distribution of cloud top phase from POLDER/ADEOS I. *Geophys. Res. Lett.*, **27**, 1707–1710.

Rosenfeld, D., Y. Rudich, and R. Lahav, 2001: Desert dust suppressing precipitation: A possible desertification feedback loop. *Proc. Natl. Acad. Sci. U.S.A.*, **98**, 5975–5980, doi:10.1073/pnas.101122798.

Roskovensky, J. K., and K. N. Liou, 2005: Differentiating airborne dust from cirrus clouds using MODIS data. *Geophys. Res. Lett.*, **32**, L12809, doi:10.1029/2005GL022798.

Rossow, W. B., and R. A. Schiffer, 1999: Advances in understanding clouds from ISCCP. *Bull. Amer. Meteorol. Soc.*, **80**, 2261−2287.

Rouse, J. W., R. H. Haas, J. A. Schell, and D. W. Deering, 1973: Monitoring vegetation systems in the Great Plains with ERTS. *Third ERTS Symposium,* NASA SP-351 I, 309-317.

Sassen, K., 1976: Polarization diversity lidar returns from virga and precipitation: anomalies and the bright band analogy. *J. Appl. Meteor.*, **15**, 292−300.

Sassen, K., 1991: The polarization lidar technique for cloud research: A review and current assessments. *Bull. Amer. Meteorol. Soc.*, **72**, 1848−1866.

Sassen, K., 1994: Advances in polarization diversity lidar for cloud remote sensing. *Proceedings of the IEEE*, **82**, 1907−1914.

Sassen, K., 2000: Lidar backscatter depolarization technique for cloud and aerosol research. In M. L. Mishchenko et al. (Eds.), *Light Scattering by Nonspherical Particles*. New York: Academic Press. 393–416.

Schotland, R. M., K. Sassen, and R. J. Stone, 1971: Observations by lidar of linear depolarization ratios by hydrometeors. *J. Appl. Meteor.*, **10**, 1011−1017.

Seinfeld, J. H., G. R. Carmichael, R. Arimoto, W. C. Conant, F. J. Brechtel, T. S. Bates, T. A. Cahill, A. D. Clarke, S. J. Doherty, P. J. Flatau, B. J. Huebert, J. Kim, K. M. Markowicz, P. K. Quinn, L. M. Russell, P. B. Russell, A. Shimizu, Y. Shinozuka, C. H. Song, Y. Tang, I. Uno, A. M. Vogelmann, R. J. Weber, J.-H. Woo, X. Y. Zhang, 2004: ACE-ASIA—Regional climatic and atmospheric chemical effects of Asian dust and pollution. *Bull. Amer. Meteorol. Soc.*, **85**(3), 367–380, doi:10.1175/BAMS-85-3-367.

Senior, C. A., and J. F. B. Mitchell, 1993: Carbon dioxide and climate: The impact of cloud parameterization. *J. Climate,* **6**, 393–418.

Shenk, W. E., and R. J. Curran, 1974: The detection of dust storms over land and water with satellite visible and infrared measurements. *Mon. Weather Rev.* **102**, 830–837.

Sokolik, I. N., and O. B. Toon, 1996: Direct radiative forcing by anthropogenic airborne mineral aerosols. *Nature*, **381**, 681–683.

Sokolik, I. N., and O. B. Toon, 1999: Incorporation of mineralogical composition into models of the radiative properties of mineral aerosol from UV to IR wavelengths. *J. Geophys. Res.*, **104**, 9423−9444.

Stackhouse, P. W. and G. L. Stephens, 1991: A theoretical and observational study of the radiative properties of cirrus: results from FIRE 1986. *J. Atmos. Sci.*, **48**, 2044−2059.

Stephens, G. L., S.-C. Tsay, P. W. Stackhouse, and P. J. Flatau, 1990: The relevance of the microphysical and radiative properties of cirrus clouds to climate and climate feedback. *J. Atmos. Sci.*, **47**, 1742−1753.

Stephens, G. L., D. G. Vane, R. J. Boain, G. G. Mace, K. Sassen, Z. Wang, A. J. Illingworth, E. J. O'Connor, W. B. Rossow, S. L. Durden, S. D. Miller, R. T. Austin, A. Benedetti, C. Mitrescu, and the CloudSat Science Team, 2002: The CloudSat mission and the A-Train: A new dimension of space-based observations of clouds and precipitation. *Bull. Amer. Meteor. Soc.*, **83**, 1771–1790.

Sun, Z. and K. P. Shine, 1994: Studies of the Radiative Properties of Ice and Mixed-Phase Clouds. *Quart. J. Roy. Meteor. Soc.*, **120**, 111–137.

Tanré, D., and M. Legrand, 1991: On the satellite retrieval of Saharan dust optical thickness over land: Two different approaches. *J. Geophys. Res.*, **96**, 5221−5227.

Tegen I., A. A. Lacis, and I. Fung, 1996: The influence of mineral aerosol from disturbed soils on the global radiation budget. *Nature*, **380**, 419−422.

Torres, O., P. Bhartia, J. Herman, Z. Ahmad, and J. Gleason, 1998: Derivation of aerosol properties from satellite measurements of backscattered ultraviolet radiation: Theoretical basis. *J. Geophys. Res. Atmos.*, **103**(D14), 17 099–17 110.

Torres, O, A. Tanskanen, B. Veihelmann, C. Ahn, R. Braak, P. K. Bhartia, P. Veefkind, and P. Levelt, 2007: Aerosols and surface UV products from Ozone Monitoring Instrument observations: An overview. *J. Geophys. Res. Atmos.*, **112**(D24), doi: 10.1029/2007JD008809.

Twomey, S., 1974: Pollution and the planetary albedo. *Atmos. Environ.,* **8**, 1251–1256.

Vaughan, M., K. Powell, R. Kuehn, S. Young, D. Winker, C. Hostetler, W. Hunt, Z. Liu, M. McGill, and B. Getzewich, 2009: Fully Automated Detection of Cloud and Aerosol Layers in the CALIPSO Lidar Measurements. *J. Atmos. Oceanic Technol.*, **26**, 2034−2050, doi: 10.1175/2009JTECHA1228.1.

Wald, A. E., Y. J. Kaufman, D. Tanré, and B.-C. Gao, 1998: Daytime and nighttime detection of mineral dust over desert using infrared spectral contrast. *J. Geophys. Res.*, **103**(D24), 32307−32313.

Weisz, E., J. Li, W. P. Menzel, A. K. Heidinger, and B. H. Kahn, 2007: Comparison of AIRS, MODIS, CloudSat and CALIPSO cloud top height retrievals. *Geophys. Res. Lett.*, **34**, L17811.

Wielicki, B. A., R. D. Cess, M. D. King, D. A. Randall and E. F. Harrison, 1995: Mission to planet Earth: role of clouds and radiation in climate. *Bull Amer. Meteorol. Soc.*, **76**, 2125–2153.

Winker, D. M., M. A. Vaughan, A. H. Omar, Y. Hu, K. A. Powell, Z. Liu, W. H. Hunt, and S. A. Young, 2009: Overview of the CALIPSO Mission and CALIOP Data Processing Algorithms. *J. Atmos. Oceanic Technol.*, **26**, 2310−2323, doi:10.1175/2009JTECHA1281.1.

Yang, P., H. Wei, H.-L. Huang, B. A. Baum, Y. X. Hu, G. W. Kattawar, M. I.

Mishchenko, and Q. Fu, 2005: Scattering and absorption property database for nonspherical ice particles in the near- through far-infrared spectral region. *Appl. Opt.*, **44**, 5512–5523, doi:10.1364/AO.44.005512.

Yoshida, Y., and S. Asano, 2005: Effects of the vertical profiles of cloud droplets and ice particles on the visible and near-infrared radiative properties of mixed-phase stratocumulus clouds. *J. Meteor. Soc. Japan*, **83**, 471–480.

You, Y., G. W. Kattawar, P. Yang, Y. Hu, and B. A. Baum, 2006: Sensitivity of depolarized lidar signals to cloud and aerosol particle properties. *J. Quant. Spectrosc. Radiat. Transfer*, **100**, 470–482.

Zender, C.S., R.L. Miller, and I. Tegen, 2004: Quantifying mineral dust mass budgets: Terminology, constraints, and current estimates. *Eos Trans. Amer. Geophys. Union*, **85**(48), 509–512.

Zhao, T. X.-P., S. Ackerman and W. Guo, 2010: Dust and smoke detection for multi-channel imagers. *Remote Sens.*, **2**(10), 2347−2368, doi:10.3390/rs2102347.

Zhu, A., V. Ramanathan, F. Li, and D. Kim, 2007: Dust plumes over the Pacific, Indian, and Atlantic oceans: Climatology and radiative impact. *J. Geophys. Res.*, **112**, D16208, doi:10.1029/2007JD008427.

APPENDIX

DERIVATION OF DISCRIMINANT ANALYSIS FORMULA

Discriminant analysis is a technique for classifying a set of measurements into predefined classes. The main purpose of discriminant analysis is to determine the class of an observation based on a set of the input variables (i.e. parameters). Following the derivation of discriminant analysis formula is based on James (1985).

Basically, discriminant analysis uses the Bayes' rule to minimize the total classification error by assigning the object to class i which has the highest conditional probability, where

$$\mathbf{P}(i \mid \mathbf{x}) > \mathbf{P}(j \mid \mathbf{x}), \textit{for } \forall\ j \neq i. \tag{A1}$$

Since we can obtain $\mathbf{P}(\mathbf{x} \mid i)$ instead of $\mathbf{P}(i \mid \mathbf{x})$ from the measurements, we use Bayes' theorem to calculate $\mathbf{P}(i \mid \mathbf{x})$ as follows;

$$\mathbf{P}(i \mid \mathbf{x}) = \frac{\mathbf{P}(\mathbf{x} \mid i)\mathbf{P}(i)}{\sum_{\forall j} \mathbf{P}(\mathbf{x} \mid j)\mathbf{P}(j)}. \tag{A2}$$

If we assume that the measurement vector x have a multivariate normal distribution, $\mathbf{P}(\mathbf{x} \mid i)$ can be expressed as follows;

$$\mathbf{P}(\mathbf{x} \mid i) = \left(\frac{1}{(2\pi)^{n/2}\left|\mathbf{C}_i\right|^{1/2}}\right)\exp\left(-\frac{1}{2}\left(\mathbf{x}-\mu_i\right)^T \mathbf{C}_i^{-1}\left(\mathbf{x}-\mu_i\right)\right), \tag{A3}$$

where μ_i is the vector **x** mean of class i and $\mathbf{C}_i$ is the covariance matrix of class i.

Thus, the Bayes' rule becomes:

Assign the object **x** to class i if

$$\begin{aligned}&\frac{\mathbf{P}(i)}{(2\pi)^{n/2}\left|\mathbf{C}_i\right|^{1/2}}\exp\left(-\frac{1}{2}\left(\mathbf{x}-\mu_i\right)^T\mathbf{C}_i^{-1}\left(\mathbf{x}-\mu_i\right)\right) > \\ &\qquad \frac{\mathbf{P}(j)}{(2\pi)^{n/2}\left|\mathbf{C}_j\right|^{1/2}}\exp\left(-\frac{1}{2}\left(\mathbf{x}-\mu_j\right)^T\mathbf{C}_j^{-1}\left(\mathbf{x}-\mu_j\right)\right), \mathit{for}\ \forall\ j \neq i\end{aligned} \quad \text{(A4)}$$

Taking the natural log (ln) and cancelling all of the terms that are common to both sides gives:

$$\begin{aligned}&-\frac{1}{2}\ln\left(\left|\mathbf{C}_i\right|\right)+\ln\left(\mathbf{P}(i)\right)-\frac{1}{2}\left(\mathbf{x}-\mu_i\right)^T\mathbf{C}_i^{-1}\left(\mathbf{x}-\mu_i\right) > \\ &\qquad -\frac{1}{2}\ln\left(\left|\mathbf{C}_j\right|\right)+\ln\left(\mathbf{P}(j)\right)-\frac{1}{2}\left(\mathbf{x}-\mu_j\right)^T\mathbf{C}_j^{-1}\left(\mathbf{x}-\mu_j\right), \mathit{for}\ \forall\ j \neq i\end{aligned} \quad \text{(A5)}$$

By multiplying both sides with -2 and rearranging terms, we have:

$$\begin{aligned}&\ln\left(\left|\mathbf{C}_i\right|\right)+\left(\mathbf{x}-\mu_i\right)^T\mathbf{C}_i^{-1}\left(\mathbf{x}-\mu_i\right)-2\ln\left(\mathbf{P}(i)\right) < \\ &\qquad \ln\left(\left|\mathbf{C}_j\right|\right)+\left(\mathbf{x}-\mu_j\right)^T\mathbf{C}_j^{-1}\left(\mathbf{x}-\mu_j\right)-2\ln\left(\mathbf{P}(j)\right), \mathit{for}\ \forall\ j \neq i\end{aligned} \quad \text{(A6)}$$

If we let

$$d_i(\mathbf{x}) = \ln\left(\left|\mathbf{C}_i\right|\right)+\left(\mathbf{x}-\mu_i\right)^T\mathbf{C}_i^{-1}\left(\mathbf{x}-\mu_i\right)-2\ln\left(\mathbf{P}(i)\right), \quad \text{(A7)}$$

which is quadratic discriminant function, the rule becomes;

Assign object with measurement $\mathbf{x}$ to class i if

$$d_i(\mathbf{x}) < d_j(\mathbf{x}), \forall\ i \neq j, \quad \text{(A8)}$$

which means that the classification rule assigns the object **x** to the group *i* with the minimum $d_i(\mathbf{x})$.

If the correlations between the variables are the same within each class, then this can be used to simplify the formula further by letting $\mathbf{C} = \mathbf{C}_i = \mathbf{C}_j$. The inequality (A6) becomes;

$$\begin{aligned}&\ln(|\mathbf{C}|) + (\mathbf{x} - \mu_i)^T \mathbf{C}^{-1}(\mathbf{x} - \mu_i) - 2\ln(\mathbf{P}(i)) < \\ &\quad \ln(|\mathbf{C}|) + (\mathbf{x} - \mu_j)^T \mathbf{C}^{-1}(\mathbf{x} - \mu_j) - 2\ln(\mathbf{P}(j)), \textit{for } \forall\ j \neq i\end{aligned} \quad \text{(A9)}$$

By expending the term $(\mathbf{x} - \mu_i)^T \mathbf{C}^{-1}(\mathbf{x} - \mu_i)$ into $\mathbf{x}\mathbf{C}^{-1}\mathbf{x}^T - 2\mu_i\mathbf{C}^{-1}\mathbf{x}^T + \mu_i\mathbf{C}^{-1}\mu_i^T$ and cancelling out common terms, then we have:

$$\begin{aligned}&-2\mu_i\mathbf{C}^{-1}\mathbf{x}^T + \mu_i\mathbf{C}^{-1}\mu_i^T - 2\ln(\mathbf{P}(i)) < \\ &\quad -2\mu_j\mathbf{C}^{-1}\mathbf{x}^T + \mu_j\mathbf{C}^{-1}\mu_j^T - 2\ln(\mathbf{P}(j)), \textit{for } \forall\ j \neq i \cdot\end{aligned} \quad \text{(A10)}$$

For convenience, it is usual to multiply both sides of the inequality by $-\frac{1}{2}$.

Finally, we get;

$$\begin{aligned}&\mu_i\mathbf{C}^{-1}\mathbf{x}^T - \frac{1}{2}\mu_i\mathbf{C}^{-1}\mu_i^T + \ln(\mathbf{P}(i)) > \\ &\quad \mu_j\mathbf{C}^{-1}\mathbf{x}^T - \frac{1}{2}\mu_j\mathbf{C}^{-1}\mu_j^T + \ln(\mathbf{P}(j)), \textit{for } \forall\ j \neq i\end{aligned} \quad \text{(A11)}$$

Let us define a new function

$$f_i(\mathbf{x}) = \mu_i\mathbf{C}^{-1}\mathbf{x}^T - \frac{1}{2}\mu_i\mathbf{C}^{-1}\mu_i^T + \ln(\mathbf{P}(i)), \quad \text{(A12)}$$

which is linear discriminant function, then the classification rule becomes;

Assign object with measurement $\mathbf{x}$ to class i if

$$f_i(\mathbf{x}) > f_j(\mathbf{x}), \forall\ i \neq j, \quad \text{(A13)}$$

which means that the linear discriminant classification rule assigns the object **x** to the group *i* with the maximum $f_i(\mathbf{x})$.

VITA

Name: Hyoun Myoung Cho

Address: Department of Atmospheric Sciences
Texas A&M University
3150 TAMU
College Station, TX, 77843-3150

Email Address: blueatmos@tamu.edu

Education: B.S., Atmospheric Sciences, Seoul National University, South Korea, 1999
M.S., School of Earth Environmental Sciences, Seoul National University, South Korea, 2002
Ph.D., Atmospheric Sciences, Texas A&M University, 2011